Title

Plasmonics powered hybrid platform for label free bio-sensing

Author

YAN, ZHONGBO

Publication Date

2017

UNIVERSITY OF CALIFORNIA

Los Angeles

Plasmonics powered hybrid platform for label free bio-sensing

A dissertation submitted in partial satisfaction of the
requirements for the degree Doctor of Philosophy
in Materials Science and Engineering

by

Zhongbo Yan

2017

ABSTRACT OF THE DISSERTATION

Plasmonics powered hybrid platform for label free bio-sensing

by

Zhongbo Yan
Doctor of Philosophy in Materials Science and Engineering
University of California, Los Angeles, 2017
Professor Ya-Hong Xie, Chair

Surface plasmons (SPs) are coherent delocalized electron oscillations that exist at the metal-dielectric interface. The charge motion in the surface plasmon creates intense electromagnetic fields at certain locations of the interface, which are referred to as "hot spots". The intense electromagnetic field associated with the excitation of surface plasmons has found applications in various bio-sensing techniques.

A unique plasmonic hybrid platform, graphene-Au pyramid structure, was invented by our group. The hybrid platform provides an ultra intense surface plasmon field and has a bio-compatible surface, making it a powerful tool for bio-sensing. The work to refine the nanostructure for generation of stronger surface plasmon field has been intensively explored by my group mates. Aside from generation of stronger surface plasmon fields, this research was done to improve several surface plasmon based techniques through the hybrid platform and to explore their applications in the label free bio-sensing field. The ultimate goal of my thesis work is to develop an integrated system for biological detection and analysis with high sensitivity and specificity.

In the bio-sensing field, especially in regards to remote detection in an analyte, the biological entities (e.g. biomolecules and cells) of interest are always dispersed in the solution. This would be a concern if we were using plasmon resonance powered techniques by themselves. The first part of this research focuses on Plasmonic tweezers, a manipulation technique to attract and capture biological entities onto the plasmonics surface. Plasmonic tweezers is noninvasive manipulation technique, in which a near-field gradient force is generated by the surface plasmon field around hot spots. It can be used to precisely control the position of biological entities. However, the near-field property of plasmonic tweezer limits its functional range in capturing biological samples. To remedy this problem, electrostatic bias is used in conjunction with plasmonic tweezers. Electrostatic bias produces a long range force whose effects spread across the entire space between a pair of electrodes. It compensates for the plasmonic tweezers' short range limitation by "condensing" molecules throughout the analyte to a layer immediately adjacent to the plasmonic surface. By using plasmonic tweezers and an electrostatic force together, the biological entities can be confined to sub-wavelength dimensions near the hot spots. For the plasmonics based bio-detection methods, the hot spots are always where the signal generates from. Therefore, this self-aligned trapping method is used to

effectively increase the sensitivity and selectivity of bio-sensing techniques.

After the biological entities are attracted to the plasmonics surface, the next step is to develop specific detection techniques. The second part of this thesis is to demonstrate the capability of the surface-enhanced Raman spectroscopy (SERS) techniques based on a nanopyramid array hybrid platform. SERS is a surface-sensitive technique employing strong plasmon resonance fields to enhance the Raman signal by several orders of magnitude. This enables even the detection of single molecules. Also, compared with other nanostructures, the hybrid platform has distinct advantages. The nanopyramid array is an open structure, in which hot spots are located between neighboring pyramids. As such, large biomolecules and biological entities can easily move into these regions and their Raman signals can be enhanced. By introducing single layer graphene, the hybrid platform provides a bio-friendly surface, preventing biological entities from being affected by toxic metals such as silver. The signal of the graphene layer can also serve as a built-in gauge of local electromagnetic field intensity used to indicate the distribution of the hot spots. These properties make the hybrid platform a powerful tool for biological detection and analysis. In this thesis work, the hybrid platform is employed to generate SERS signals of biological samples, in particular, the characterization of exosomes and T-cells. However, the biological entities would naturally bring variations to the SERS signals due variations in the type and quantity of their chemical compositions. In our research, principle component analysis (PCA) is also employed to interpret the SERS data and provide a

statistical investigation of the biological samples.

To achieve dynamic monitoring of biological processes, higher sensitivity and temporal resolution are preferred. In the last part of this thesis, another label free bio-sensing technique, surface-enhanced coherent anti-Stokes Raman spectroscopy (SECARS), was developed based on the hybrid platform. A multiplicative enhancement of the Raman signal over CARS and SERS is achieved using a novel SECARS setup. Compared to previous setups, it shows a broadband feature with high spectral resolution, which is preferred in biological detection. The novel setup based on the hybrid platform could be a powerful tool for not only the characterization of biological entities but also the dynamic monitoring of various biological processes.

The dissertation of Zhongbo Yan is approved.

Mark S. Goorsky

Delroy A. Baugh

Ya-Hong Xie, Committee Chair

University of California, Los Angeles

2017

To my parents, who supported me throughout my PhD study

Table of Contents

Acknowledgments

First, I want to express my gratitude to Prof. Ya-Hong Xie, who patiently guided my research throughout all my PhD study at UCLA. Prof. Xie's abundant knowledge and altitude to scientific research benefit me a lot. Through Prof. Xie's mentorship, I not only learned how to conducted research independently, but also developed my skill set. I want to extend my gratitude to my lab mates in Prof. Xie's Group: Dr. Ming Xia, thank you for the insightful discussion about the SERS and teaching me about nanostructure fabrication; Dr. Wei Zhang and Jimmy Ng, thank you for the nanofabrication and the materials growth at the Nanolab at UCLA; Owen Liang, thank you for training me to grow graphene and using Raman microscope; Zirui Liu, thank you for the help with the Raman measurement; Xinke Yu, thank you for the help in the experimental data analysis; Pei Zhang, Peiyi Ye and Yao Yang, thank you for the kind help in my research and the open discussions.

In addition, I want to thank the collaborators during my PhD research. I want to thank Dr. Anatoly Efimov at Los Alamos National Laboratory for teaching me the knowledge of nonlinear optics and the guidance on the construction of the SECARS instrument. Moreover, I want to thank Prof. Gal Bitan and Dr. Suman Dutta for providing inspiring thinking from the biology perspective and the high quality biological samples.

At the end, I want to thank my parents for their support to my choice to study abroad and pursue my dreams.

VITA

2012	B.S. in Physics Peking University Beijing, China
2017	Ph.D. Candidate in Materials Science and Engineering University of California, Los Angeles Los Angeles, CA, USA

Publications:

1. Yan Z, Liu Z, Xia M, et al. Broadband surface-enhanced coherent anti-Stokes Raman spectroscopy with high spectral resolution. *Journal of Raman Spectroscopy*, 2017.
2. Yan Z , Xia M, et al. Self-Aligned Trapping and Detecting Molecules Using a Plasmonic Tweezer with an Integrated Electrostatic Cell. *Advanced Optical Materials*, 2017, 5(5).
3. Yan Z, Xia M, et al. Selective Manipulation of Molecules by Electrostatic Force and Detection of Single Molecules in Aqueous Solution. *The Journal of Physical Chemistry C*, 2016, 120(23), 12765-12772.

Chapter 1 Introduction

1.1 Motivation of the thesis

Surface plasmon resonance (SPR) is a charge-density oscillation existing at the interface of two media with dielectric constants of opposite signs, for instance, a metal and a dielectric. Since the first application of the surface plasmon resonance phenomenon for bio-sensing in 1983[1,2], many efforts have been devoted to develop various SPR-based methods to enhance the specificity and sensitivity for bio-sensing[3,4,5,6,7,8,9,10,11,12,13]. Although there are continuous reports of new progress and applications in literature, building up an integrated bio-sensing system by combining various SPR-based techniques is still under development. Our group invented a unique plasmonic hybrid platform[14,15]. The hybrid platform can generate an intense surface plasmon field, and meanwhile has a chemically stable and biologically compatible surface, making it a powerful tool for bio-sensing. The main objective of the thesis work is to develop an integrated system based on the hybrid platform for bio-detection and analysis, and explore its applications in the label free bio-sensing field. The integrated system includes manipulation techniques, label free bio-detection methods and statistical method for data analysis.

This chapter introduces the background of surface plasmon resonance (SPR) in Section 1.2, molecular manipulation techniques in Section 1.3, Raman spectroscopy and its applications in biological studies in Section 1.4, and the plasmonics hybrid platform in

Section 1.5. Chapter 1.6 presents the outline of the dissertation.

1.2 Surface Plasmon Resonance

Surface plasmon resonance is the resonant oscillation of conduction electrons at the interface between materials of negative and positive dielectric constants stimulated by incident light. SPR was first demonstrated by Otto in 1968[16]. Discussions of surface plasmons and their origins and principles can be found in many books and review articles, for example, Hass et al. (1977), Raether (1988), Homola (2006) , and Kalele et al. (2007).

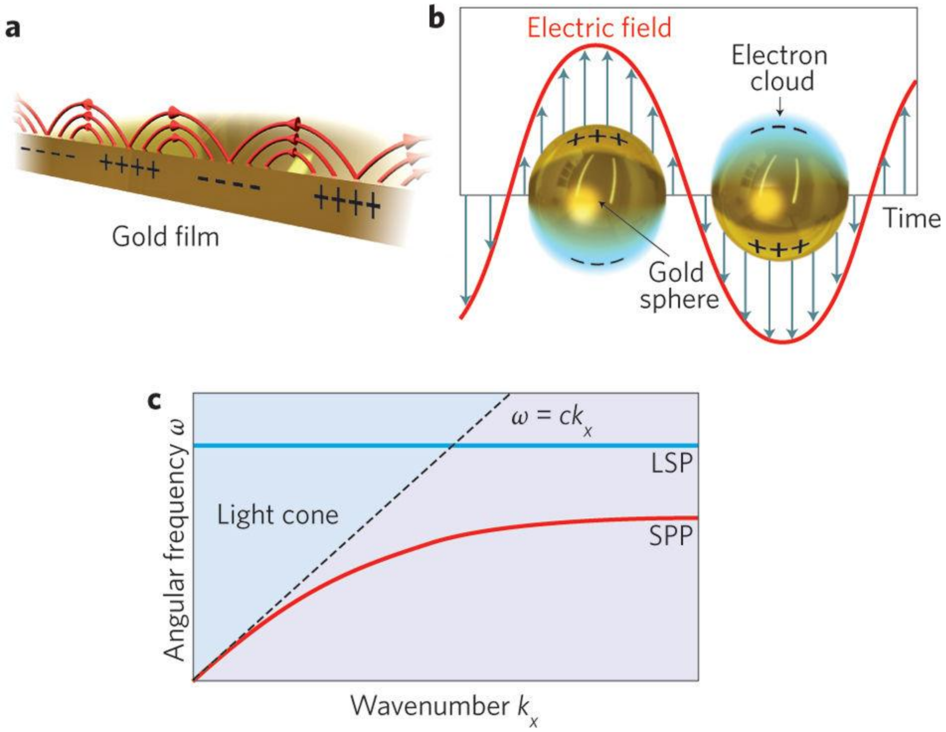

Figure 1.1. Illustration of SPPs and LSPs, together with their associated dispersion diagrams. (a) (b) Collective oscillation of electrons with the incident electromagnetic field at a flat gold–air interface (SPP; a) and in a gold nanoparticle (LSP; b). (c) Typical dispersion curves of SPPs (red) and LSPs (blue).

Two distinct types of surface plasmons are known to exist, depending on the geometry of the metals. Figure 1.1 presents schematic diagram of SPR on the interface of a thin metal film and a dielectric as well as on isolated nanoparticles. SPR associated with a metallic thin film of thickness in the 10-200 nm range can travel along the interface, which is termed propagating SPR or surface plasmon polariton[17] (SPP, Figure 1.1a). The SPR associated with nanoparticles of noble metals within a size range of 10-200 nm is localized to each nanoparticle, which is called localized SPR[18] (LSPR, Figure 1.1b).

SPP is a non-radiative electromagnetic wave that propagates in a direction parallel to the metal-dielectric interface. Because SPPs are pure evanescent modes decaying exponentially away from the interface, they cannot be directly coupled to propagating light and thus a technique is required to compensate for the momentum mismatch[3,18]. This is usually done by illuminating a thin metal film under total internal reflection through a glass prism of higher refractive index than the dielectric. Efficient coupling to a SPP mode enables light at the metal surface to be concentrated into an intense and confined surface wave whose intensity is dramatically larger than the incident light intensity. Since the wave is on the boundary of the conductor and the external medium (air, water or vacuum for example), these oscillations are very sensitive to any change of this boundary, such as the adsorption of molecules to the conducting surface. Furthermore, the plasmon wavelength can be tuned by proper control of the metal film's shape and thickness, which can be used as plasmonics waveguide.

LSPRs are collective electron charge oscillations on individual metallic nanoparticles. They exhibit enhanced near-field electromagnetic fields at the resonance wavelength. This field is highly localized at the nanoparticles and decays rapidly away from the nanoparticle/dieletric interface into the dielectric background. The LSPR has very high spatial resolution (subwavelength) due to the localization, limited only by the size of nanoparticles. SPPs have a continuous dispersion relation and therefore exist over a wide range of frequencies, but LSP resonances exist only over a finite frequency range owing to the additional constraints imposed by their finite dimensions (Figure 1.1c). The spectral position of the surface plasmon resonance is governed by the particle's size and shape, as well as by the dielectric functions of both the metal and the surrounding media. LSPs can be directly coupled with propagating light, whereas SPPs cannot.

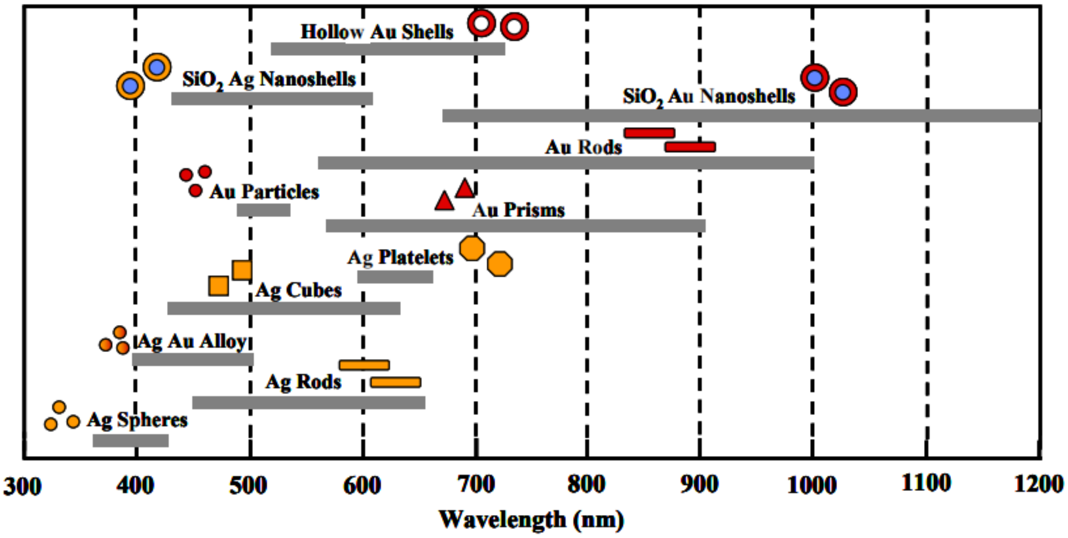

Figure 1.2. Tuning of SPR of metal nanoparticles by varying their size and shape.

A variety of metals, including silver, gold, copper, aluminum, sodium, indium, titanium, and chromium, can exhibit SPR phenomenon[19]. Compared to nanostructures made of other materials, those of gold and silver have been studied much more extensively because of their unique optical properties. As shown in Figure 1.2, silver and gold nanostructures exhibit tunable optical properties over wide spectral ranges. For gold and silver nanoparticles, usually the SPR band lies in the visible range of electromagnetic spectrum. But silver is too susceptible to oxidation and could be poisonous to biological samples, so gold is preferred for bio-sensing. The SPR bandwidth and the peak maximum are dependent on various factors such as size and shape as well as the relative permittivity of the medium in which they are dispersed. The SPR band can be tuned from the visible to the near-infrared ranges simply by varying the shape of the nanoparticles[20]. For instance, when the shape changes from spherical to aciculate (i.e., rod-like), a single broad plasmon absorption band splits into two plasmon bands.

In recent years, the potential of plasmonics has been realized in making highly sensitive photonic devices. A wide range of applications arising from controlling the light at the nanoscale have been established, such as high-resolution optical imaging below the diffraction limit, enhanced optical transmission through sub-wavelength apertures, bio-detection at single molecule level, nanoscale wave guiding, and surface-enhanced Raman scattering. Surface plasmon resonance are finding an increasing number of applications in traditional domains of surface characterization and sensors as well as in newly emerging nano-photonic and optoelectronic technologies. Undoubtedly, these developments will benefit the development of bio-sensing field.

1.3 Molecular Manipulation Techniques

Single-molecule manipulation techniques have evolved rapidly over the past 15 years[21,22]. Several techniques have been developed, such as optical tweezers[23,24], magnetic tweezers[25], atomic force microscopy[26] (AFM), glass microneedle[27], and the biomembrane force probe[28]. Among these techniques, optical tweezers permit noninvasive, full three-dimensional control over the position of the trapped object, affording it wider applicability, particularly in the biosensing field.

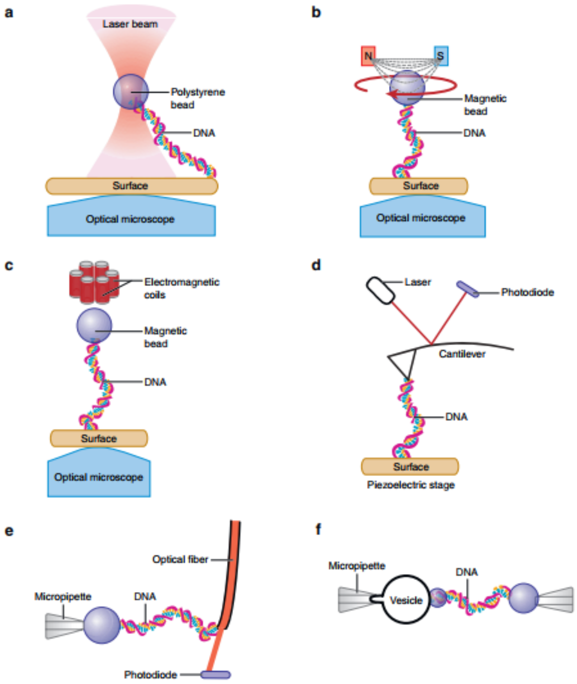

Figure 1.3. Schematic representation of micromanipulation techniques (not to scale).

As a noninvasive technique, the use of optical force on micrometer-sized particles was first reported in 1970 by Ashkin and Dziedzic[29]. Although optical tweezers based on far-field have proven highly successful for manipulating objects with precision on the order of the wavelength of light, they face difficulties at the nanoscale because of the diffraction-limited focused spot size and the rapidly decreased force intensity. To overcome the problems, the use of the “plasmonic tweezers”, the near fields around a nanostructured surface, has been explored. In the early years of research into near-field optics, several theoretical proposals were provided regarding the use of evanescent fields for optical trapping[30,31]. Experimental research on surface plasmon based trapping was triggered by pioneering studies into the enhanced force field at a homogeneous gold/water interface. In 2006, Garcés-Chávez and co-workers reported the self-assembly of a large number of micrometer-sized dielectric beads within the region of a gold surface where an SPP was excited[32]. The same year, Volpe *et al.* used photonic force microscopy to probe the surface plasmon force field, and measured a 40-fold enhancement to the force magnitude[33].

Beyond the interest for performing unprecedented basic experiments, plasmonic tweezers may play a key role in the development of future integrated analytical platforms, known as ‘lab-on-a-chip’. Surface plasmon trapping could become an important tool for capturing biomolecules and immobilizing cells for a period of time that allows them to be inspected optically. The combination of plasmonic tweezer and surface-enhanced spectroscopy could largely improve the sensitivity and specificity of the bio-sensing techniques.

1.4 Raman Spectroscopy and Its application in Biological Studies

Raman spectroscopy, a molecular spectroscopy which is observed as inelastically scattered light, allows for the interrogation and identification of vibrational (phonon) states of molecules. As a result, Raman spectroscopy provides an invaluable analytical tool for molecular finger printing as well as monitoring changes in molecular bond structure (e.g. state changes and stresses & strains). In comparison to other vibrational spectroscopy method, Raman has several major advantages in bio-sensing field. These advantages stem from the fact that the Raman effect manifests itself in the light scattered off of a sample as opposed to the light absorbed by a sample. As a result, Raman spectroscopy requires little to no sample preparation and is insensitive to aqueous absorption bands. Raman spectroscopy is commonly used to provide a structural "fingerprint" by which molecules can be identified. The label-free nature of Raman spectroscopy makes it a powerful option for studies of biological samples over several decades.

In Raman scattering process, a molecule absorbs an incident photon with energy E_L and is excited from ground state to a virtual state by the incident photon. Because the virtual state is not stable, the molecule will jump back to its vibrational state and emit a Raman scattered photon with different energy E_S. The energy difference between the incident photon and the Raman scattered photon is called Raman shift ($\Delta E_R=E_L-E_S$), which provides vibrational information of molecules. ΔE_R is positive for a Stokes and negative for an anti-Stokes process. Figure 1.4 shows the schematic of Raman scattering process (Stokes-process). Raman spectrum is wavelength- (or energy-) dependence of Raman scattered intensity at a given incident wavelength.

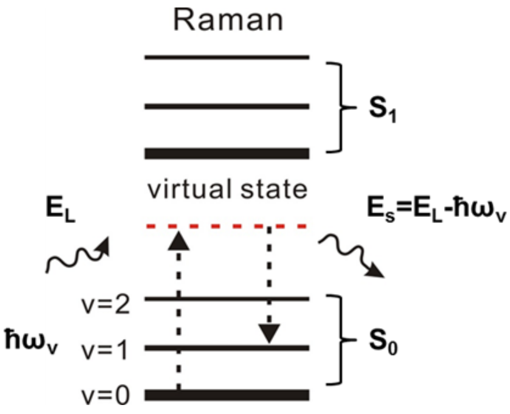

Figure 1.4 Schematic of Raman scattering process (Stokes-process).

So far, Raman spectroscopy has been widely employed in an impressive number of studies of in *vitro* and in *vivo* biological systems (DNA, peptide and proteins, microbes and virus, cells, etc.). Raman spectroscopy has a wide variety of applications in biology and medicine. It has helped confirm the existence of low-frequency phonons in proteins and DNA, promoting studies of low-frequency collective motion in proteins and DNA and their biological functions. Raman reporter molecules with olefin or alkyne moieties are being developed for tissue imaging with SERS-labeled antibodies. Raman spectroscopy has also been used as a noninvasive technique for real-time, in situ biochemical characterization of wounds. Multivariate analysis of Raman spectra has enabled development of a quantitative measure for wound healing progress. Spatially offset Raman spectroscopy (SORS), which is less sensitive to surface layers than conventional Raman, can be used to discover counterfeit drugs without opening their packaging, and to non-invasively study biological tissue. Raman spectroscopy also has a wide usage for studying biominerals. Lastly, Raman gas analyzers have many practical applications, including real-time monitoring of anesthetic and respiratory gas mixtures during surgery.

The most noticeable drawback of Raman spectroscopy is the extremely low yield and the resulting low detection sensitivity. Various derivative techniques of Raman spectroscopy have been employed to enhance Raman signal. Among these derivatives, surface-enhanced Raman spectroscopy[34,35] (SERS) and to a lesser extent coherent anti-Stokes Raman spectroscopy[36,37](CARS) are the most successful ones. SERS is a technique capable of boosting by orders of magnitude the Raman signals from molecules located within tens of nanometers of metallic nanostructures[38]. The enhancement arises mainly from the intensified optical fields stemming from surface plasmon resonance. CARS is an alternative way of achieving Raman signal enhancement. It employs multiple photons to interact with molecular vibrations in a coherent fashion leading to greatly enhanced signals. With the development of the derivative techniques, Raman spectroscopy has become one of the most promising label free analytical techniques for bio-sensing.

1.5 Plasmonics Hybrid Platform

To generate intense SPR field as well as SERS signals for bio-sensing, our lab invented a unique hybrid platform, which consists of a graphene-Au pyramid structure (Figure 1.5)[39,40,41]. An ideal surface plasmonic nanostructure for biosensing is expected to be reproducible, very sensitive, chemically stable, biological compatible, and should be easily fabricated at the scale of manufacturing. The hybrid platform is demonstrated to have a single molecule sensitivity. The periodic Au nano-pyramid structure with tunable size and sharpness can be fabricated via a bottom-up self-assembly process, which is suitable for mass production and provides a reproducible and uniform SPR field. A graphene layer on top of the metal surface provides a bio-compatible surface, independent of the type of metal used, for supporting plasmon resonance. Also, the graphene layer is chemically inert so that it is easily refreshed after each test and also resistant to the degradation of the metallic nano-structures. Besides that, the graphene layer serves as a hotspot marker indicating the intensity of individual hotspot of surface plasmon resonance. Therefore, the SPR field intensity from different set of substrates and different locations of the same substrate can be compared by normalized to the optical signals of graphene. Owing to these properties, this hybrid platform could be a powerful option for label free bio-sensing.

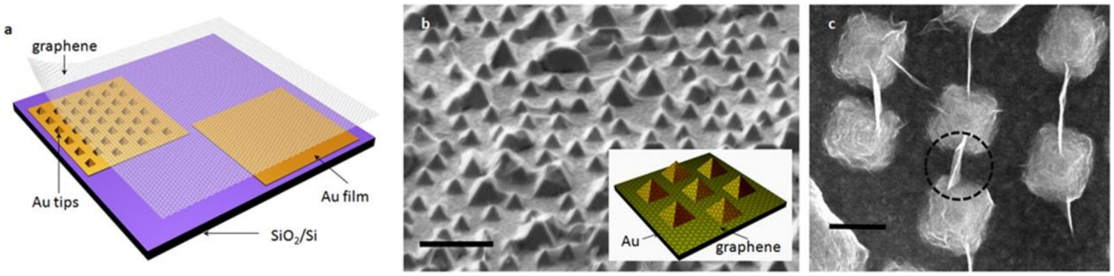

Figure 1.5. Hybrid platform: graphene-Au nanopyramid (tip) structure. (a) Schematics of typical samples. (b) SEM image of graphene on Au tips; scale bar 1 μm. Inset: Schematic image of graphene on Au tips. (c) SEM image of hexagonally arranged arrays of Au tips with sharply folded graphene; scale bar 200 nm. The dotted black circle indicates a hanging graphene fold between neighboring tips.

1.6 Outline of Thesis

Chapter 2 describes the experimental and theoretical studies of molecular manipulation techniques for biosensing applications *via* plasmonic hybrid platform. A self-aligned molecular manipulation method by combining the plasmonic tweezer and the electrostatic force is demonstrated. Factors affecting molecular motion are investigated. The molecular motion is monitored by SERS. Through the combined method, the capture of single molecules and a dramatic increase of the SERS signal intensity are observed. The combined method offers a new approach for enhancing bio-detection sensitivity and a noninvasive way for precisely control and alignment of biomolecules in solution.

Chapter 3 presents biological studies on exosomes and T-cells using the SERS hybrid platform. The interest in exosome-based disease diagnostics and prognosis has risen substantially in recent years prompting urgent need for characterizations of exosomes. A rigorous study to identify the finger-print Raman signature of exosomes from specific sources is performed based on the hybrid platform by correlating Raman and SEM measurement. The capability of the hybrid platform to distinguish among exosomes isolated from different sources by combining the SERS with principal component analysis (PCA) is also demonstrated.

Chapter 4 describes the application of hybrid platform for coupling SERS (plasmon resonance) and CARS (coherence and nonlinear process) processes. SERS and CARS are widely used methods for improving the intensity of Raman scattering process. By using the unique graphene-Au pyramids hybrid platform, a multiplicative enhancement is achieved to generate surface-enhanced CARS (SECARS) signals. A broadband SECARS setup with high sensitivity and high spectral resolution is presented in this chapter. This powerful technique could be instrumental in furthering the understanding of various chemical and biological processes.

Chapter 5 concludes the thesis by providing the major results with a section that proposes future work that can build on the results presented herein.

References

1 Liedberg, Bo, Claes Nylander, and Ingemar Lunström. "Surface plasmon resonance for gas detection and biosensing." Sensors and actuators 4 (1983): 299-304.

2 Liedberg, Bo, Claes Nylander, and Ingemar Lundström. "Biosensing with surface plasmon resonance—how it all started." Biosensors and Bioelectronics 10.8 (1995): i-ix.

3 Homola, Jiří, Sinclair S. Yee, and Günter Gauglitz. "Surface plasmon resonance sensors." Sensors and Actuators B: Chemical 54.1 (1999): 3-15.

4 Willets, Katherine A., and Richard P. Van Duyne. "Localized surface plasmon resonance spectroscopy and sensing." Annu. Rev. Phys. Chem. 58 (2007): 267-297.

5 Pattnaik, Priyabrata. "Surface plasmon resonance." Applied biochemistry and biotechnology 126.2 (2005): 79-92.

6 Jönsson, U., et al. "Real-time biospecific interaction analysis using surface plasmon resonance and a sensor chip technology." Biotechniques 11.5 (1991): 620-627.

7 Homola, Jiří. "Present and future of surface plasmon resonance biosensors." Analytical and bioanalytical chemistry 377.3 (2003): 528-539.

8 Homola, Jiří. "Surface plasmon resonance sensors for detection of chemical and biological species." Chemical reviews 108.2 (2008): 462-493.

9 Haes, Amanda J., and Richard P. Van Duyne. "A nanoscale optical biosensor: sensitivity and selectivity of an approach based on the localized surface plasmon resonance

spectroscopy of triangular silver nanoparticles." Journal of the American Chemical Society 124.35 (2002): 10596-10604.

10 Mayer, Kathryn M., and Jason H. Hafner. "Localized surface plasmon resonance sensors." Chemical reviews 111.6 (2011): 3828-3857.

11 Rich, Rebecca L., and David G. Myszka. "Advances in surface plasmon resonance biosensor analysis." Current opinion in biotechnology 11.1 (2000): 54-61.

12 Nelson, Bryce P., et al. "Surface plasmon resonance imaging measurements of DNA and RNA hybridization adsorption onto DNA microarrays." Analytical chemistry 73.1 (2001): 1-7.

13 Zeng, Shuwen, et al. "Nanomaterials enhanced surface plasmon resonance for biological and chemical sensing applications." Chemical Society Reviews43.10 (2014): 3426-3452.

14 Wang, Pu, et al. "Ultra-Sensitive Graphene-Plasmonic Hybrid Platform for Label-Free Detection." Advanced Materials 25.35 (2013): 4918-4924.

15 Wang, Pu, et al. "Label-free SERS selective detection of dopamine and serotonin using graphene-Au nanopyramid heterostructure." Anal. Chem87.20 (2015): 10255-10261.

16 Otto, Andreas. "Excitation of nonradiative surface plasma waves in silver by the method of frustrated total reflection." Zeitschrift für Physik 216.4 (1968): 398-410.

17 Zayats, Anatoly V., Igor I. Smolyaninov, and Alexei A. Maradudin. "Nano-optics of

surface plasmon polaritons." Physics reports 408.3 (2005): 131-314.

18 Maier, Stefan A. "Localized surface plasmons." Plasmonics: fundamentals and applications (2007): 65-88.

19 Kalele, Suchita A., et al. "Plasmon-assisted photonics at the nanoscale." Journal of Nanophotonics 1.1 (2007): 012501-012501.

20 Sun, Yugang, and Younan Xia. "Gold and silver nanoparticles: a class of chromophores with colors tunable in the range from 400 to 750 nm." Analyst128.6 (2003): 686-691.

21 Neuman, Keir C., and Attila Nagy. "Single-molecule force spectroscopy: optical tweezers, magnetic tweezers and atomic force microscopy." Nature methods 5.6 (2008): 491-505.

22 Bockelmann, Ulrich. "Single-molecule manipulation of nucleic acids." Current opinion in structural biology 14.3 (2004): 368-373.

23 Xie, C.; Mace, J.; Dinno, M. A.; Li, Y. Q.; Tang, W.; Newton, R. J.; Gemperline, P. J. Identification of Single Bacterial Cells in Aqueous Solution Using Confocal Laser Tweezers Raman Spectroscopy. Anal. Chem. 2005, 77, 4390-4397.

24 Svedberg, F.; Li, Z.; Xu, H.; Käll, M. Creating Hot Nanoparticle Pairs for Surface-enhanced Raman Spectroscopy through Optical Manipulation. Nano Lett. 2006, 6, 2639-2641.

25 Gosse, Charlie, and Vincent Croquette. "Magnetic tweezers: micromanipulation and

force measurement at the molecular level." Biophysical journal 82.6 (2002): 3314-3329.

26 Anderson, M. S. Locally Enhanced Raman Spectroscopy with an Atomic Force Microscope. Appl. Phys. Lett. 2000, 76, 3130-3132.

27 Kishino, Akiyoshi, and Toshio Yanagida. "Force measurements by micromanipulation of a single actin filament by glass needles." Nature334.6177 (1988): 74-76.

28 Gourier, Christine, et al. "A nanospring named erythrocyte. the biomembrane force probe." Cellular and Molecular Bioengineering 1.4 (2008): 263.

29 Ashkin, Arthur. "Acceleration and trapping of particles by radiation pressure." Physical review letters 24.4 (1970): 156.

30 Kawata, Satoshi, and Tadao Sugiura. "Movement of micrometer-sized particles in the evanescent field of a laser beam." Optics letters 17.11 (1992): 772-774.

31 Girard, Christian, Alain Dereux, and Olivier JF Martin. "Theoretical analysis of light-inductive forces in scanning probe microscopy." Physical Review B49.19 (1994): 13872.

32 Garcés-Chávez, V., et al. "Extended organization of colloidal microparticles by surface plasmon polariton excitation." Physical Review B 73.8 (2006): 085417.

33 Volpe, Giovanni, et al. "Surface plasmon radiation forces." Physical review letters 96.23 (2006): 238101.

34. Stiles, P. L., Dieringer, J. A., Shah, N. C., & Van Duyne, R. P. (2008).

Surface-enhanced Raman spectroscopy. Annu. Rev. Anal. Chem., 1, 601-626.

35. Xia, M., Qiao, K., Cheng, Z., & Xie, Y. H. (2016). Multiple layered metallic nanostructures for strong surface-enhanced Raman spectroscopy enhancement. Applied Physics Express, 9(6), 065001.

36. Yan, Z., Xia, M., Zhang, P., & Xie, Y. H. (2017). Self-Aligned Trapping and Detecting Molecules Using a Plasmonic Tweezer with an Integrated Electrostatic Cell. Advanced Optical Materials.

37. Yan, Z., Xia, M., Wang, P., Zhang, P., Liang, O., & Xie, Y. H. (2016). Selective Manipulation of Molecules by Electrostatic Force and Detection of Single Molecules in Aqueous Solution. The Journal of Physical Chemistry C, 120(23), 12765-12772.

38. Haynes, C. L., McFarland, A. D., & Duyne, R. P. V. (2005). Surface-enhanced Raman spectroscopy. Analytical Chemistry, 77(17), 338-A.

39. Wang, P., Zhang, W., Liang, O., Pantoja, M., Katzer, J., Schroeder, T., & Xie, Y. H. (2012). Giant optical response from graphene–plasmonic system. ACS nano, 6(7), 6244-6249.

40. Wang, P., Liang, O., Zhang, W., Schroeder, T., & Xie, Y. H. (2013). Ultra-Sensitive Graphene-Plasmonic Hybrid Platform for Label-Free Detection. Advanced Materials, 25(35), 4918-4924.

41. Xia, M., Zhang, P., Qiao, K., Bai, Y., & Xie, Y. H. (2015). Coupling SPP with LSPR

for Enhanced Field Confinement: A Simulation Study. The Journal of Physical Chemistry C, 120(1), 527-533.

Chapter 2 Molecular Manipulation Techniques Based on Hybrid Platform

2.1 Introduction

Detection, transportation, assembly, and distinguishment of biomolecules in aqueous solutions are widely studied with the development of many biomedical devices. These biomedical devices have shown a broad range of applications in fields[1,2,3,4,5] such as bio-sensing, cell sorting and selections, advanced drug-delivery, *etc.* For plasmonics-based biosensing in dilute solutions, the manipulation of biomolecules is critical to improve the performance of such devices, since the plasmonics are always surface sensitive. Conventional methods of molecular manipulation include chemical functionalization of molecules[6] or substrates,[7] and the use of atomic force[8] or optical force.[9,10] A number of novel methods of nano-particle manipulation have appeared recently in the literature including 2D assembly by evaporation-based convection,[11] capillary interaction,[12] 3D self assembly on liquid/liquid interfaces[13] and during droplet evaporation.[14] All these methods have advantages and disadvantages. For some of them, the potential for practical use is yet to be demonstrated.

As a noninvasive technique, the use of optical force on micron sized particles was first reported in 1970 by Arthur Ashkin[15]. Although optical tweezers[16,17,18,19,20,21] based on far-field have proven highly successful for manipulating objects with precision on the order of the wavelength of light, they face difficulties at the nanoscale such as trapping single molecules at individual plasmon resonance hotspots because of the diffraction-limited focused spot size. The trapping potential varies with the cube of the object's diameter, so smaller objects require much higher laser power. In addition, positional control with a precision commensurate with object size is difficult, as the potential well in which the object is trapped has a width of roughly half the wavelength. As a result, it is hard to use optical tweezers for a precision alignment. To overcome these problems, the use of the "plasmonic tweezers", the near-fields around a nanostructured surface, has been explored.[22,23,24,25,26,27]. Nanostructured surfaces enable intense fields confined to sub-wavelength dimensions and the field enhancement is achieved over a broad range of wavelengths.

The plasmonic tweezer is a near-field effect with the intensity of the plasmonic field decays exponentially away from the hotspots of plasmon resonance[28]. This property limits the range of plasmonic tweezers in trapping molecules. Electrostatic bias on the other hand, is a long range force with its effect spreads across the entire space in between the pair of electrodes. Combining with plasmonic tweezers, it could be leveraged to compensate for the short range limitation by "condensing" molecules from all across the analyte to a layer immediately adjacent to the plasmonic surface thereby greatly increase the probability of the molecules being trapped by the plasmonic field. In addition plasmonic hotspots are often associated with topological protrusions on the surface leading to concentrated electric field lines analogous to the function of lightening rods. As such, combining plasmonic tweezers with electrostatic bias allows for all molecules distributed across the analyte to first be condensed to the near surface region (electrostatic force) and subsequently be trapped by the plasmonic hotspots. Furthermore, electrostatic force can also be used to a certain extent to selectively attract (or repel) one type of molecule in an aqueous solution to (or from) an electrode based on the differences in their charge, polarizability, mass and acidity. To explore this possibility, we performed attraction/repulsion cycles of a mixture of more than one type of molecule by varying the magnitude and the polarity of the electrostatic bias.

A major challenge for the manipulation is the *in situ* monitoring of biomolecules during manipulation and assembly in aqueous solution. The sub-micrometer length scale of biomolecules and the liquid environment limit the effective observation either by the naked eyes or by conventional optical microscopes. Fluorescence-based methods have been proven to be highly useful, including single molecule detection inside living cells[29,30,31]. However, labeling molecules with fluorophores can be expensive and time consuming, and for certain applications it may not even be feasible[32,33,34,35]. SERS is one of the most commonly used label-free methods today[36,37.38,39]. The intense gradient field induced by the plasmonic structure can not only produce gradient force for capturing molecules, but also the surface enhancement for the Raman signal intensity. Therefore the combination appears to be the ideal for enhancing SERS sensitivity especially in the case of dilute analyte.

In this study, the integrated hybrid platform consisting of graphene and a plasmonic substrate is employed for the capture and detection of individual molecules. By combining electrostatic bias with plasmonic tweezers, the molecules moved to SERS hotspots in a self-aligned way with the force field extended throughout the liquid analyte. We show the theory to understand the physics governing the molecular motion in solutions under the plasmonic tweezer effect and electrostatic force. The calculation results of the surface plasmon field and related force field are presented in this chapter. Furthermore, we provide experimental results which demonstrate the selective attraction of the electrostatic force and the combination effect of the plasmonic tweezers and electrostatic force.

2.2 Experimental Methods

The experimental setup consists of three components: a polydimethylsiloxane (PDMS) cell that allows electrostatic bias across a liquid, a SERS active substrate, and Raman spectroscope.

The PDMS cell is shown in Figure 2.1a. The cell is constructed of two glass slides coated with 200 nm of indium tin oxide (ITO) and a circular PDMS wall for containing the analyte. The separation between the plates is 5 mm. The diameter of the cell is 1 cm. A DC voltage source is connected to the ITO contacts. Because it is transparent in the visible range, the ITO layer allows us to illuminate the cell from the top with a ×50 long working distance microscope objective (numerical aperture ~0.5).

The SERS active substrate is a Au pyramid-graphene hybrid platform,[40] which has an ultra high Raman enhancement. Figure 2.1b is the scanning electron microscope (SEM) image of this substrate. The Au nanopyramid-graphene hybrid platform has been shown to render a remarkable Raman enhancement factor of up to 10^{12}. The periodic Au nanopyramid structure with tunable size and sharpness can be fabricated via a wafer-scale bottom-up templating technology.The base dimension of the pyramids is 250 nm and the center-to-center distance between adjacent pyramids is 500 nm (Figure 2.1c). The graphene has three functions in the experiment. Firstly, it provides an additional SERS enhancement factor of about 10. Secondly the graphene serves as a bio-compatible surface independent of the type of metal used for supporting plasmon resonance. More importantly the graphene is employed as a hotspot marker which indicates the intensity and stability of the hot spots.

The Raman spectra were taken using a Renishaw inVia Raman spectroscope under ambient conditions. The laser excitation wavelength was 633 nm from a He-Ne laser. The power of the lasers was kept at 5 mW to avoid sample heating. The diameter of laser spot was ~1 μm.

As shown in Figure 2.1a, aqueous analyte was introduced into the PDMS cell with a voltage bias between the ITO glass and the hybrid SERS platform. The electrostatic force is produced by an applied voltage between the plates giving rise to an electric field perpendicular to the plates. The plasmonic tweezer in this experiment is excited at the hot spot region by turning the laser on. The laser used for turning on plasmonic tweezer is the same laser used for the Raman spectroscopy. Theoretically the plasmonic tweezer will always be on when the Raman signal is collected. However, the existence of a time constant of the response to the plasmonic tweezer effect allows us to decouple these two processes. This time constant is on the order of tens of seconds mainly due to the finite viscosity of the analyte. The fact can be clearly seen in the following experimental results. In contrast, the time duration for collecting Raman spectra is 1 second. So it is reasonable to assume that the influence of Raman measurement on the molecular motion is negligible. Raman spectroscopy was employed to monitor the change of molecular concentration with time at individual SERS hotspots after switching on the bias voltage.

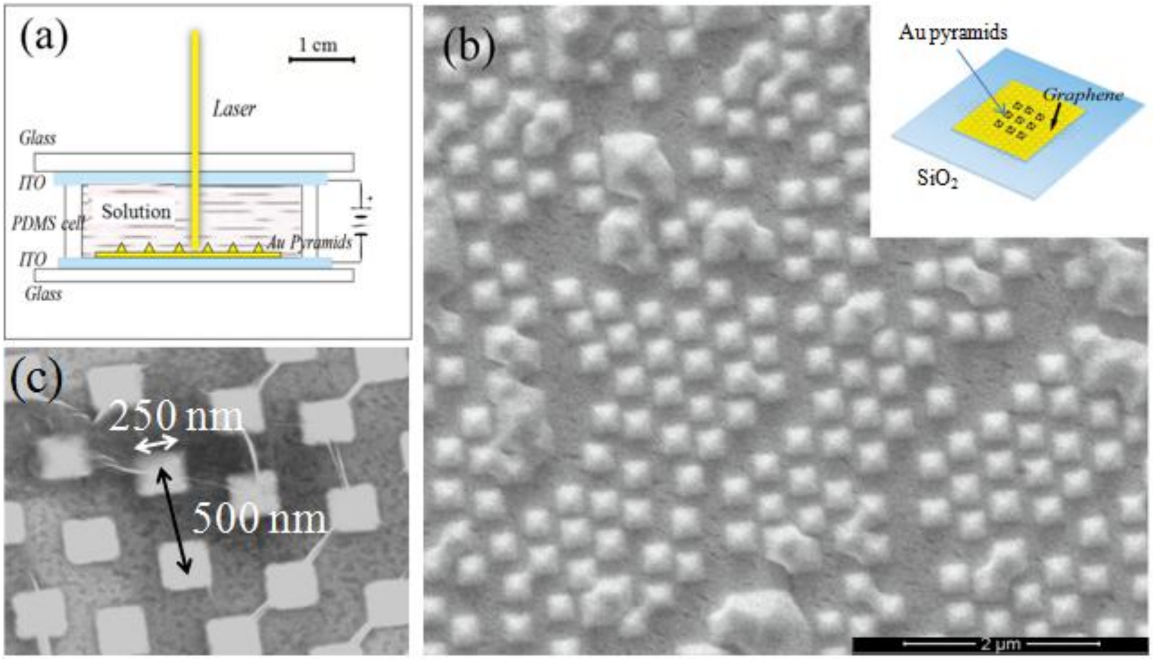

Figure 2.1. Experimental setups (a) Schematic diagram of the PDMS cell structure. (b) and (c) SEM image of the Au pyramid-graphene hybrid platform. Insert: schematic diagram of the Au-pyramid-graphene hybrid platform.

2.3 Theoretical Analysis and Simulation Method

2.3.1 Plasmonic Tweezer

The surface plasmon field distribution and the force field distribution is simulated by using Finite-difference time-domain (FDTD) solution software, which qualitatively illustrated In the simulation model, the substrate is Au submerged in water. The side length of the pyramids is 200 nm and the center-to-center distance between adjacent pyramids is 400 nm. Periodic boundary condition is invoked. The wavelength of the light source is 633 nm, which is the same as the wavelength of the laser source employed in the experiments. Two forces are involved in the plasmonic tweezer effect: gradient force and scattering force (Equation 1). The force field distribution is calculated based on the following equations.[41]

$$\begin{aligned} \vec{f}(\vec{r}) &= \vec{f}_{grad}(\vec{r}) + \vec{f}_{scat}(\vec{r}) \\ \vec{f}_{grad}(\vec{r}) &= \frac{\alpha\varepsilon_m}{2}\nabla\left|E_m(\vec{r})\right|^2 \\ \vec{f}_{scat}(\vec{r}) &= \alpha\varepsilon_m \frac{\partial\left(E_m(\vec{r},t)\times B_m(\vec{r},t)\right)}{\partial t} \end{aligned} \tag{2.1}$$

Where the optical force ($\vec{f}$) includes two parts: gradient force ($\vec{f}_{grad}$) and scattering force ($\vec{f}_{scat}$). α represents the induced dipole moment of the molecules. ε_m represents the relative dielectric constant. E_m is the local electric field intensity. B_m represents the local magnetic field intensity. The molecular model is based on the R6G molecule. The polarizability of R6G is $980\,\text{Å}^3$ (CGS system of units) [42] and the relative dielectric constant is estimated through Clausius Mossotti relation.

2.3.2 Electrostatic Force

Three forces are involved during the molecular motion under voltage bias: (1) electrostatic force, (2) Brownian motion force and (3) drag force. For the electrostatic force:

$$\vec{F}_{electrostatic} = q\vec{E} + \left(\varepsilon\alpha\vec{E}\cdot\nabla\right)\vec{E} \qquad (2.2)$$

where q is the charge of molecules, $\vec{E}$ is electrical field intensity, ε is the dielectric constant, α is the polarizability of molecules. The first term represents the electric force on a point charge and the second term represents the electric force on dipoles.

For the Brownian motion force and drag force:[43]

$$\vec{F}_{brownian} = \vec{\zeta}\sqrt{\frac{12\pi k_B \mu T r_P}{\Delta t}} \qquad (2.3)$$

$$\vec{F}_{drag} = \frac{1}{\tau_P} m_P\left(\vec{u}-\vec{v}\right) = 6\pi\mu r_p\left(\vec{u}-\vec{v}\right),\ \tau_P = \frac{2\rho_p r_p^2}{9\mu} \qquad (2.4)$$

where $\vec{\zeta}$ is a Gaussian random number with zero mean and unit variance, μ is viscosity, T is temperature, r_p is the radius of particles, m_p is the mass of particles, ρ_p is the density of particles, and $\vec{u}$ and $\vec{v}$ are the velocity of the medium and particles respectively (in most cases $\vec{u}$ =0).

These equations indicate that the molecular motion highly depends on the properties of molecules (such as the charge, mass and radius) and the external factors (voltage, temperature, viscosity, etc). By varying the external factors, the attraction or repulsion velocity could be changed. In the meantime, different responses of molecules to the external field enable selective attraction and repulsion.

The motion of molecules under electrostatic bias was simulated with COMSOL Multiphysics to clearly show the distribution change of the analyte. Figure S5 shows the simulation model. In order to make it more close to the real experiment environment, the built in material is set as water, the substrate material is set as Au, and the particle model (including mass and radius) is based on R6G molecules. As observed in the experiment, the laser spot diameter is about 1 μm. As shown in Figure S5b, it could roughly cover seven Au pyramids. Therefore in our simulation, we monitored the variation of particle quantity within the region of seven pyramids. Considering the computational capability, we set the total side length of the simulation region as 3 μm, which is twice the length of the monitored region. In the following sections, we present the calculation results of the molecular distribution change of the molecules with time and compared the simulation results with the experiment results.

2.4 Results and Discussion

2.4.1 Molecular Motion under Plasmonic Tweezer

First we focused on the influence of the effect of individual plasmonic tweezers. The simulation results are shown in Figure 2.2. From the distribution of surface plasmon field (Figure 2.2a), we could see that the hot-spot regions are on the two sides of the nanopyramids and very close (~20 nm) to the nanostructure surface. The color bar represents the electric field intensity in logarithmic scales. The force density distribution (Figure 2b) shows that a very intense attraction force (>10^{11} N m^{-3}) exists around the hot-spot regions, pushing molecules towards the hot spots. These intense trapping potential wells are also highly localized to within a 20 nm region around the nanostructured surface. This provides the capability of precise positional control of particles that are much smaller than the incident light wavelength.

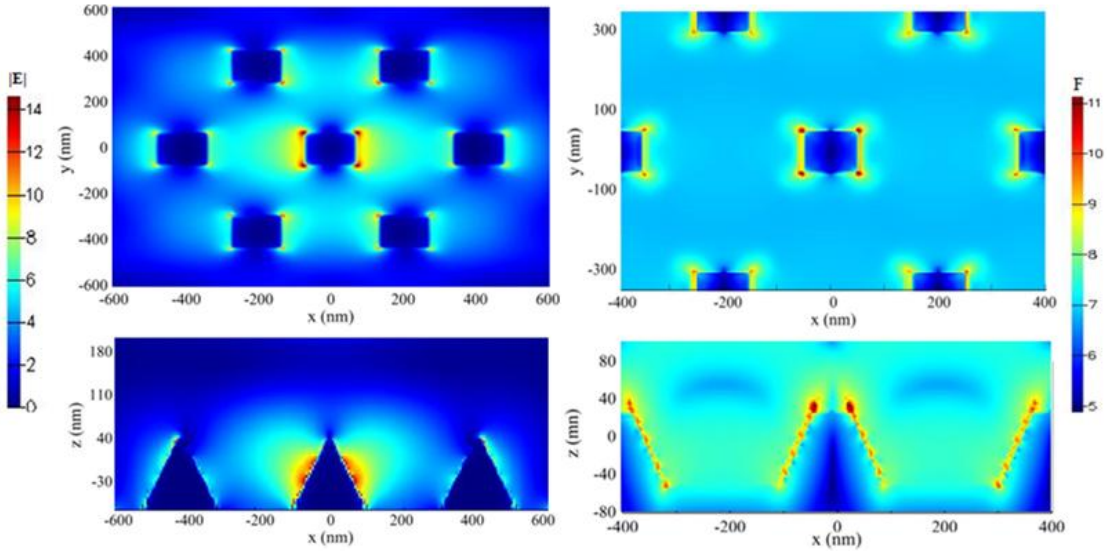

Figure 2.2. Simulation model and results of plasmonic tweezer effect by using FDTD solution. (a)

Top: electric field distribution at xy-plane (top view); Bottom: electric field distribution at xz-plane (side view); The color bar represents the electric field intensity in logarithmic scales. (b) Top: force field distribution at xy-plane; Bottom: force field distribution at xz-plane. The color bar represents the force density in logarithmic scales.

We used Rhodamine 6G (R6G) molecules as the target molecules. R6G is a fluorescent Rhodamine family dye with positively charged in aqueous solution[44]. The electrostatic cell was filled with aqueous Rhodamine 6G solutions of 10^{-6} *M*. In the initial state (t=0 min), the laser was off so that the plasmonic tweezer was off. The Raman spectrum of R6G at initial state was shown in Figure 2.3a (black curve). Then the plasmonic tweezer was turned on. The Raman spectrum was collected every 20 s. The change of the Raman intensity (peak intensity at 1361 cm^{-1}, normalized to the graphene G peak) with time is shown in Figure 2.3b. During the whole measurement, the Raman intensity of graphene G peak kept unchanged, indicating that the electromagnetic field stayed constant. In the meantime, the Raman intensity of R6G kept increasing, indicating the increase of the quantity of molecules. After 5 min, the intensity approached to saturation. The increase of the molecules was a result of molecular Brownian motion and subsequent capture of plasmonic tweezer. The saturation phenomenon was due to the limited space of the hot spots which contributed to most of the SERS signal intensity. Then, at 6 min, the plasmonic tweezer was turned off and there was a consequent decrease of Raman signal intensity. When the plasmonic tweezer was off, the molecules moved away from the nanostructured surface under the influence of concentration gradient force. From Figure 2.3a we could find that the rate of increase of the signal intensity was slower than the rate of decrease. The reason is that when the plasmonic tweezer was turned on the molecules moved against the concentration gradient but when the plasmonic tweezer was turned off the molecules moved along the concentration gradient. As a result, the molecules moved faster when the plasmonic tweezer was turned off. Under the plasmonic tweezer effect, the molecules were trapped by the hot spots and there was an enhancement (>10 times) to the overall SERS intensity. The time constant for the plasmonic tweezer to take effect is on the order of tens of seconds, much larger than the acquisition time of Raman measurement. To demonstrate its usefulness, we further repeated the plasmonic tweezer experiments with dopamine (189.64 g/mol) and lysozyme (14,307 Da), which is presented in Figure 2.4.

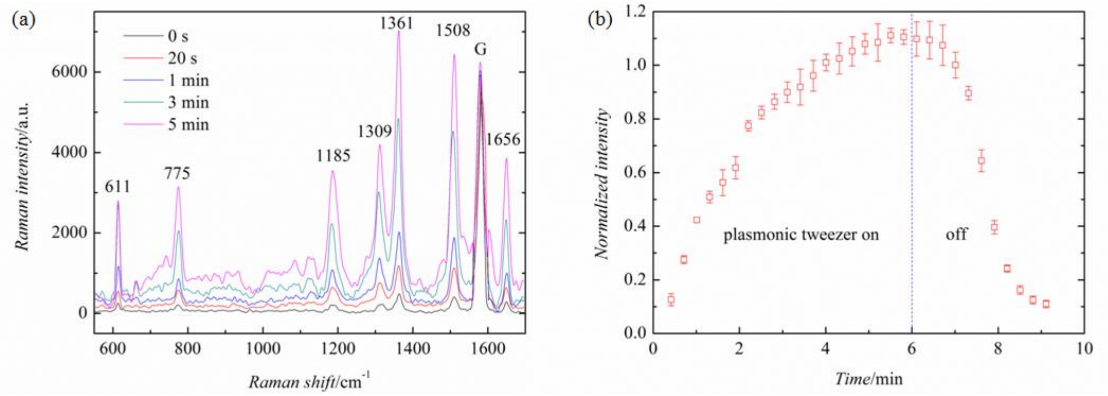

Figure 2.3. Change of Raman spectra of R6G under plasmonic tweezer effect. (a) The Raman spectra of R6G at 0 s, 20 s, 1 min, 3 min and 5 min. The intensity of the graphene G peak kept constant during the measurement; (b) The change of Raman signal intensity (1361 cm^{-1} peak) with time. The Raman

signal intensity is normalized to the intensity of the graphene G peak. The plasmonic tweezer was on from 0 min to 6 min and the plasmonic tweezer was off from 6 min to 9 min.

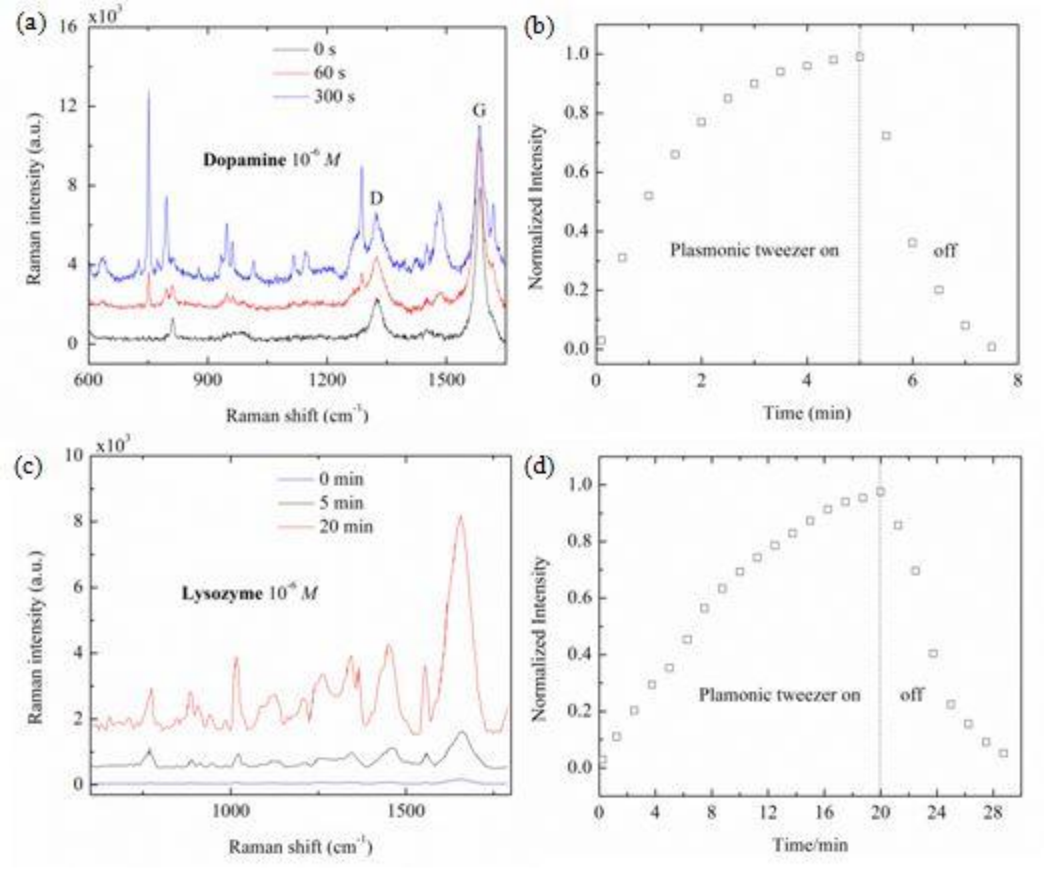

Figure 2.4. Change of Raman spectra of dopamine (189.64 g/mol) and lysozyme (14,307 Da) under plasmonic tweezer effect. (a) The Raman spectra of dopamine at 0 s, 60 s, 300 s; (b) The change of Raman signal intensity (742 cm^{-1} peak) with time. The plasmonic tweezer was on from 0 min to 5 min and the plasmonic tweezer was off from 5 min to 8 min. (c) The Raman spectra of lysozyme at 0 min, 5 min, 20 min; (d) The change of Raman signal intensity (1020 cm^{-1} peak) with time. The plasmonic tweezer was on from 0 min to 20 min and the plasmonic tweezer was off from 20 min to 30 min.

2.4.2 Molecular Motion under Electrostatic Force

In this section focus on the molecular motion under electrostatic force. The basic idea is to attract /repel the molecules to/ from the SERS substrate by applying a voltage bias. The analyte was the solution of R6G, which is positively charged in analyte. The concentration of the solution was 10^{-7} *M*. The SERS signal of the analyte was monitored *in situ* while cycling the bias voltage across the cell. From 0 to 20 min, we applied a voltage bias of +1 V from the top electrode to the bottom electrode, and the voltage bias direction was changed every 20 minutes. To maximize the performance of electrostatic force the cycle time was determined to be 20 minutes. There are several ways to shorten the time duration like reducing the cell size (such as the cases in lab-on-a-chip[45]), increasing voltage bias, changing operating temperature, *etc*.

Figure 2.5a shows the SERS intensity of four different Raman modes as a function of time. The laser was focused on the hybrid platform and the Raman spectra were measured every 20 s. The SERS activity is fairly homogeneous for the different modes of the sample and the repulsion motion is faster than the attraction motion. During the cycles, the G peak of graphene stays constant, which can be interpreted as an evidence of the stability of the SERS activity. Figure 2.5b shows the Raman spectra at 0 min, 20 min and 40 min, corresponding to the initial point, maximum point (forward bias) and minimum point (reverse bias) in Figure 2.5a. By attracting the molecules onto the substrate, the

Raman spectra intensity could be dramatically enhanced as shown in the spectra. There is more than 2 orders of magnitude difference between the Raman intensity at forward bias and reverse bias.

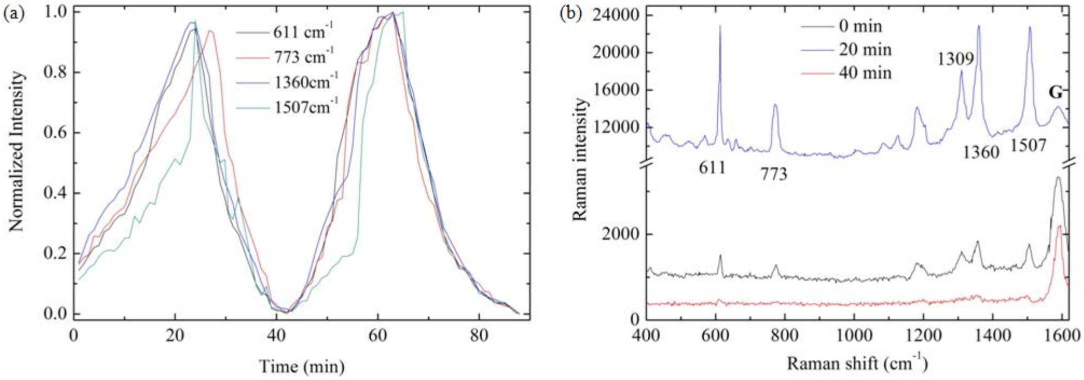

Figure 2.5. (a) Raman spectra intensity of R6G molecules under attraction and repulsion cycles. Different curves represent different spectral modes of R6G Raman spectrum (611 cm^{-1}, 773 cm^{-1}, 1360 cm^{-1}, 1507 cm^{-1}). The intensity of each spectral mode is normalized to the its maximum intensity during the attraction/repulsion cycles. (b) The Raman spectra of R6G at 0 min, 20 min and 40 min, corresponding to the initial points, maximum intensity points and minimum intensity points in (a) with the intensity of G peak unchanged.

The simulation results are consistent with the experimental results. Figure 2.6a shows the simulation model. The substrate is a Au pyramid array arranged in hexagonal lattice. The particle model (the particle radius and mass) is based on R6G molecules. The driving force of this model is based on functions (1) (2) and (3). Figure 2.6b, 2.6c and 2.6d show the molecular distribution at 0 V, +1 V and -1 V, respectively. We could see that at 0 V particles are uniformly distributed and at +1 V and -1 V particles are attracted to or repelled from the electrode. Figure 3e shows the comparison between simulation results and experiment results when applying different voltage bias (±2 V, ±1 V, ±0.5 V). The quantity of particles that attracted to the hot spots (solid lines, Figure 2.6e) was calculated and compared with Raman signal intensity (open circles, Figure 2.6e), which shows the same trend. It should be noted that for forward bias, the saturation rate of the simulation results is faster than that of the experimental results. The reason is that in the experiments the Raman signal not only came from the hot-spot regions although they contributed to most of the SERS signal, but also from the molecules attracted to other regions. However, in the simulation model only the particles that attracted to the hot-spot regions were counted, so it saturated faster than the experimental result. Simulation results also show the trend where the repulsion motion is faster than the attraction motion, which is identical with the observation in the experiments. The reason is that the repulsion motion is resulted from the combined effect of electrostatic force and gradient force since the molecular concentration in the region close to the substrate surface region is much higher than that in other positions. But for the attraction motion the electrostatic force is partially counteracted by gradient force. As a result, the saturation rate of the repulsion motion is faster than that of the attraction motion.

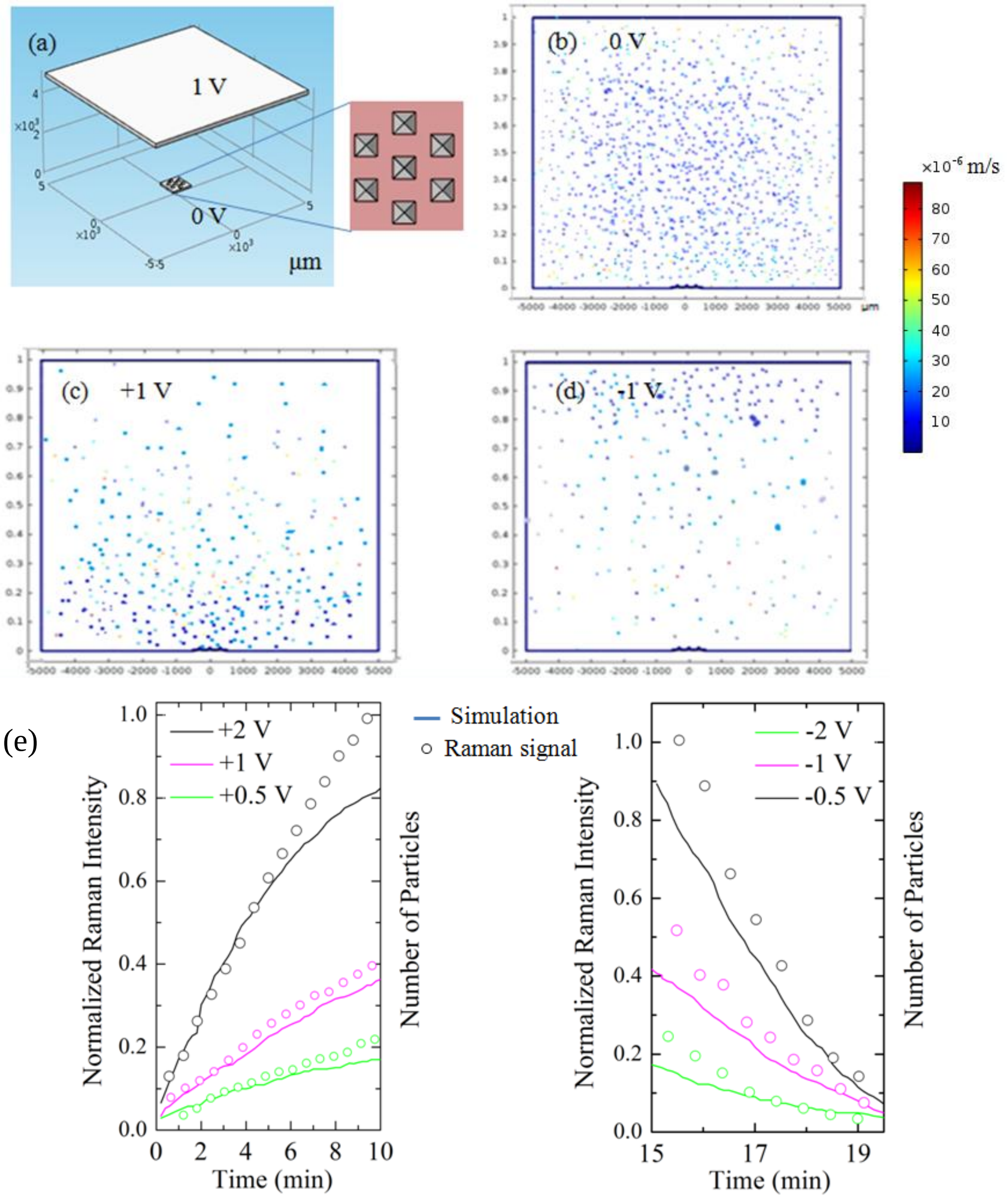

Figure 2.6. Simulation method and the results of molecular distribution. (a) The Comsol Multiphysics simulation model diagram. (b) The simulation results of molecular distribution at voltage bias of 0 V. The colors of the particles represent their different velocity. (c) The simulation results of molecular distribution at voltage bias of +1 V. (d) The simulation results of molecular distribution at voltage bias of -1 V. (e) The comparison between simulation results (solid line) and experiment results (open circles, Raman signal intensity at 1507 cm^{-1}) when applying different voltage bias (±2 V, ±1 V, ±0.5 V).

The Raman signal intensity is normalized to the maximum intensity at ±2 V during attraction/repulsion cycles.

We also observed the stepwise increase of the R6G Raman signal (Figure 2.7). The concentration of the R6G solution under detection was 10^{-9} *M*. At such low concentration, there are only 2-6 molecules within the area that the laser spot could cover (~μm^3), which indicates single-molecular level attraction and detection. To obtain the stepwise increase of Raman signal, the Raman spectra was collected every 3 s and the collection time of one spectrum was 2 s. In Figure 2.7b, we present the Raman spectra of R6G at 0 s (background signal), 30 s, 80 s and 120 s, corresponding to the time point shown in Figure 2.7a. The signal to noise ratio (S/N) is not very good since the concentration is much lower compared to previous experiments (10^{-7} *M*). With the time increases, the signal intensity approaches to a limit, since the quantity of molecules within the detection volume is extremely low. The stepwise increase phenomenon is a direct proof to the single-molecule level Raman sensitivity and the capability of electrostatic force.

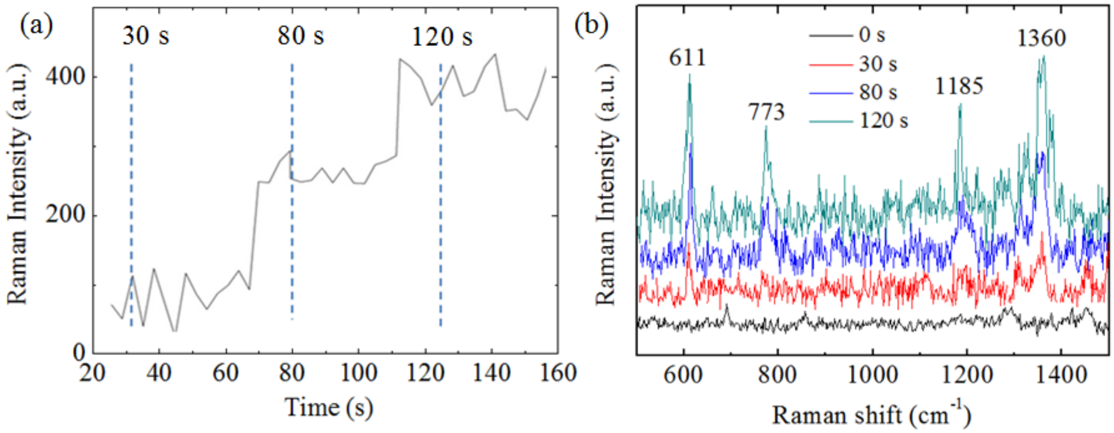

Figure 2.7. (a) The stepwise increase of Raman signal intensity with the increase of time at very low concentration (10^{-9} *M*). (b) Raman spectra of R6G at 30 s, 80 s, and 120 s, corresponding to the three stages in (a) marked by the dotted lines. To clearly show each spectrum, we added a constant offset between each line.

2.4.3 Selective Attraction by Electrostatic Force

Equation 2.2 indicates that the molecules with different charges have different responses to the external electrical field. Particularly for opposite charges, they will move in opposite directions under the same electric field. To show this effect, we added another type of molecule, 4-MBA (4-Mercaptobenzoic acid) molecules (pKa ~4.79, molecular mass ~154 g/mol), into the solution. First, we tested the change of 4-MBA Raman spectra under electrostatic force (Figure 2.8). The solution concentration was 10^{-7} *M*. The voltage bias was -1 V from the top electrode to bottom electrode. The Raman intensity of 4-MBA greatly changed with time. We observed the similar phenomena as those in R6G solution. However there are two differences: (1) The voltage bias is opposite to that in R6G solution since 4-MBA and R6G have opposite charges; (2) The intensity change of 4-MBA is faster since the molecular mass of 4-MBA is smaller.

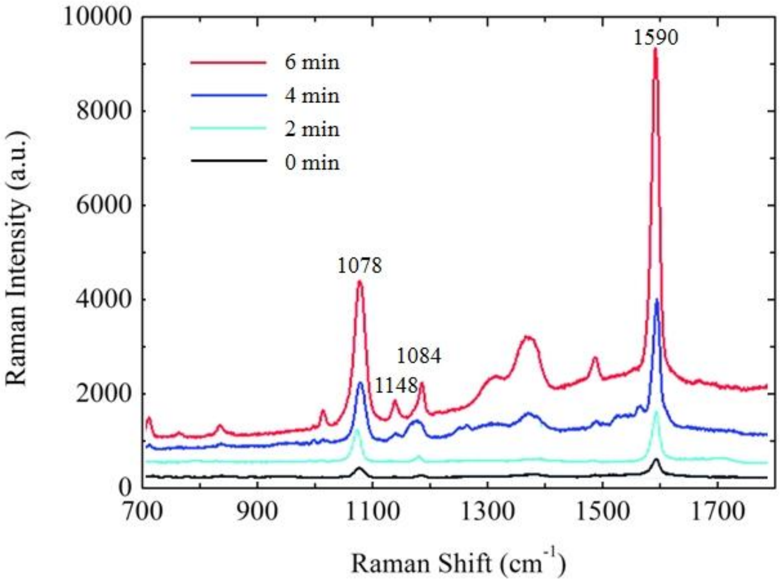

Figure 2.8. Raman spectra of 4-MBA at 0 min, 2 min, 4 min and 6 min.

Figure 2.9 shows the selective attraction and repulsion in the mixture solution when alternating the applied voltage (the cycle time is about 10 min). Figure 2.9a represents the Raman spectrum of mixture solution at 10 min with the voltage bias at +1 V. R6G was attracted to the SERS substrate and 4-MBA repelled from the substrate. The black arrows point out the Raman modes of R6G and the red arrows point out the Raman modes of 4-MBA. Figure 2.9b shows the Raman spectrum at 20 min with voltage bias at -1 V. R6G was repelled from the substrate and 4-MBA was attracted to the substrate. As the Figure 2.9b shown, the R6G's signal is almost overwhelmed by the 4-MBA's signal. The Raman peaks at 1309, 1360 and 1508 cm^{-1} are the strongest modes of R6G, the hint of these Raman modes could still be observed at negative bias. Figure 2.9c shows the Raman intensity change of R6G (black line) and 4-MBA (red line) with time. The relative intensity of the Raman modes of each species keeps consistent during the attraction/repulsion cycles.

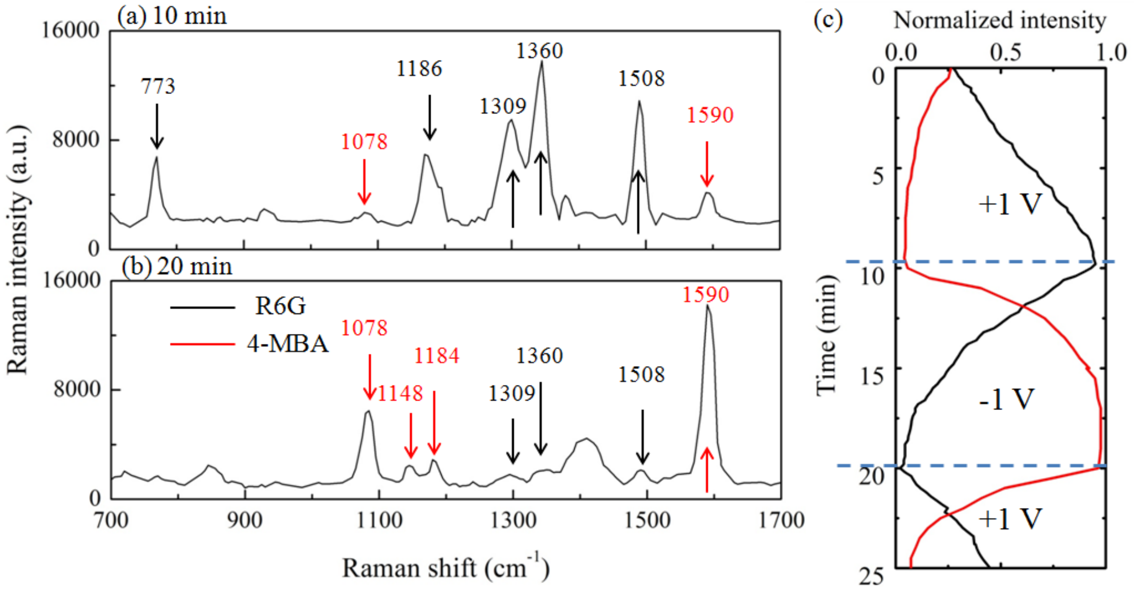

Figure 2.9. Selective attraction of 4-MBA and R6G mixture solution. (a) The spectrum at 10min under positive voltage bias. (b) The spectrum at 20 min under negative voltage bias. The red arrows mark the Raman modes of 4-MBA and the black arrows mark the Raman modes of R6G. (c) The Raman signal intensity change of R6G (black, 1360 cm^{-1}) and 4-MBA (red, 1590 cm^{-1}) with time. The Raman intensity of each species is normalized to its maximum Raman intensity during the attraction/repulsion cycle.

Once again it is obvious that the movement of 4-MBA is faster than that of R6G. The qualitative analysis shows that the directional movement velocity of molecules is highly dependent on its molecular mass. This trend is supported by the comparison between the experimental observations and the simulation results assuming the Raman signal intensity is proportional to the number of molecules attracted to the substrate. Figure 2.10 shows the comparison of the motion between R6G and 4-MBA. Solid lines represent the simulation results and open circles represent the experiment results. The attraction rate of 4-MBA is faster than that of R6G, which is consistent with our expectation. While the actual value is different by < 12% for 4-MBA and < 24% for R6G, the similarity of the overall trend lends support to our model being correct.

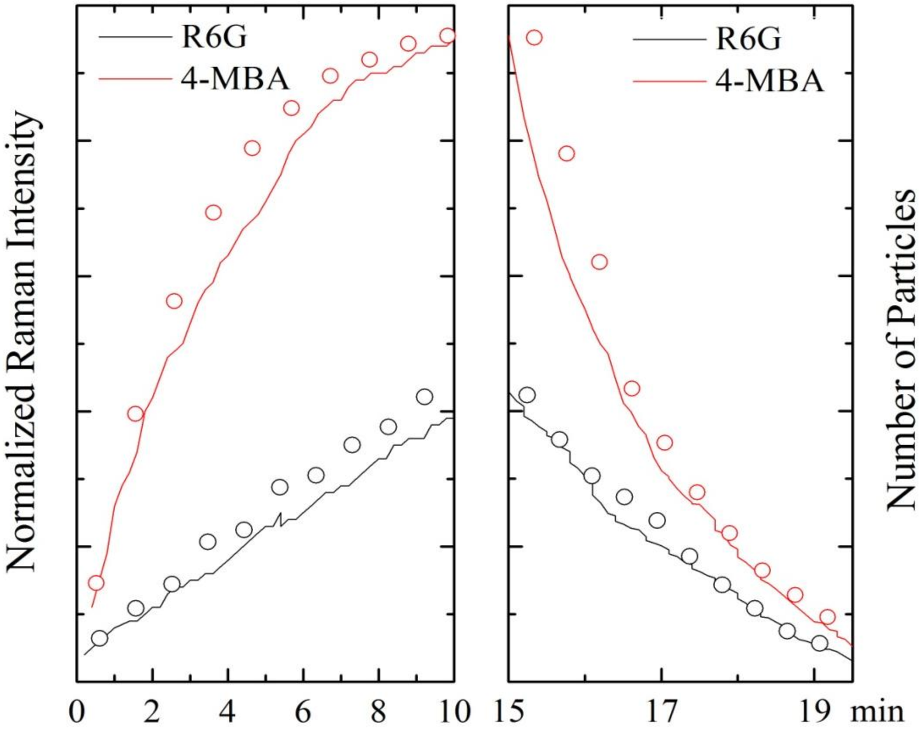

Figure 2.10. Comparison of the simulation results and experimental results of the Raman signal intensity with increasing time. The red line and black line are the simulation results of 4-MBA and R6G, respectively. The open circles represent the experimental results. The Raman signal intensity is normalized to the maximum intensity during attraction/repulsion cycles.

Besides the charge state, the molecular mass could also be an important factor influencing the motion of molecules under electrostatic force. It is possible to achieve the selective attraction of the smaller molecules while the bigger molecules are almost kept still. The principle is very similar to a mass spectrometer which uses a magnetic field to separate out gaseous molecules based on their charge-mass ratio. The influence of mass can already be seen from the above experiments and simulation. However, to clearly show the influence of molecular mass, we chose lysozyme (isoelectric point ~10.5) as the compared molecule. Its molecular weight (about 14,000 g/mol), comparing with the 4-MBA (154 g/mol) and R6G (479 g/mol), is much bigger, while still having the same charge as R6G. The concentration of lysozyme was 10^{-6} *M*, 10 times larger than the other two species. Figure 2.11 shows the Raman spectra of the mixture solution of these three molecules. Figure 2.11a and 2.11b shows the spectra at 5 min and 20 min with the voltage bias at +1 V (lysozyme and R6G are both attracted to the SERS substrate). Although the concentration of lysozyme is larger than that of R6G, the signal of R6G is more pronounced than lysozyme since R6G moves faster than lysozyme at 5 min. Figure 2.11c shows the spectrum with voltage bias at -1 V. At this voltage bias, the 4-MBA was attracted to the substrate while the other two molecules were repelled from the substrate. So we could see that the signal of 4-MBA with lysozyme and R6G disappeared at 30 min.

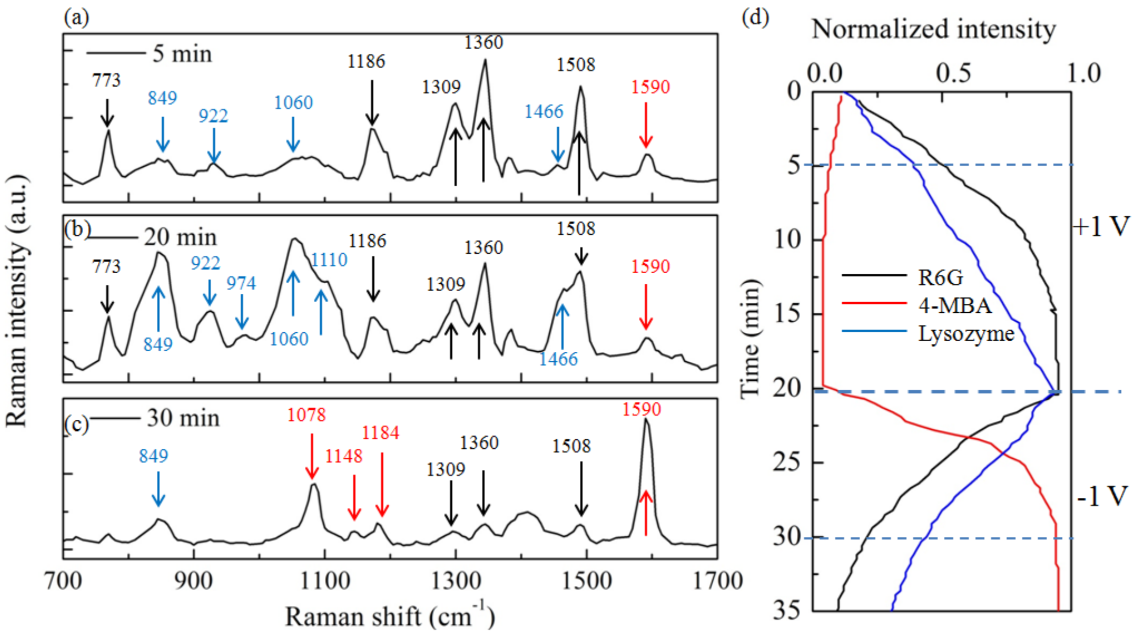

Figure 2.11. Selective attraction and repulsion of R6G, 4-MBA and lysozyme mixture solution. (a) The spectrum at 5 min under positive voltage bias. (b) The spectrum at 20min under positive bias. (c) The spectrum at 30 min under negative bias. The red arrows mark the peaks of 4-MBA, the black arrows mark the peaks of R6G, the blue arrows mark the peaks of lysozyme. (d) The Raman signal intensity change of R6G (black) 4-MBA (red) and lysozyme (blue) with time. The Raman intensity of each species is normalized to the its maximum Raman intensity during the attraction/repulsion cycle.

Therefore, by combining the influence of molecular charge and mass, we could achieve the selective attraction among different molecules which gives us the ability to study certain class of molecular species. This is especially useful when the concentration or Raman cross-section of one molecule is much smaller than that of the other molecules in the mixture solution. In our experiments, we employed R6G as an indicator to show that even though it has a lower concentration, we could still observe its signal under selective attraction, which is not possible in a normal situation. The selective attraction will also be useful when the Raman cross-section of certain kind of molecule is much lower than other molecules.

2.4.4 Capture of Single Molecules using Combined Method

In this section, we demonstrate the combined effect of plasmonic tweezer and electrostatic force. The simulation results (Figure 2.2) indicates that the plasmonic tweezer effect could only affect the region very close to (~20 nm) the nanostructured surface, necessitates a longer range force in order to influence molecules further away from the hotspots. Electrostatic bias on the other hand, is a long range force with its effect spreads across the entire space in between the pair of electrodes. The combination method could guide molecules from all across the analyte to a layer immediately adjacent to the plasmonic surface thereby greatly increase the probability of the molecules being trapped by the plasmonic field.

The experimental results under the combination effect of plasmonic tweezer and the electrostatic force is shown in Figure 2.12. The molecules were first guided towards the nanostructured surface by electrostatic force when voltage bias of 1 V across the PDMS cell was applied at 0 min. The signal intensity kept increasing during first 5 min (Stage 1). Figure 2.8a shows the Raman spectra of R6G at different time (0 min, 2 min, 3 min and 5 min). Comparing with plasmonic tweezer, the electrostatic force has a much stronger attraction effect. The Raman intensity at 1361 cm^{-1} at 5 min under electrostatic force (Figure 2.12a) is about 48000 counts, but under plasmonic tweezer effect it is only about 6000 counts. Then the plasmonic tweezer was turned on and the voltage bias was turned off simultaneously at 5 min (Stage 2). By turning off the voltage bias, the influence of the electrical field is excluded so that we can compare the molecular motion with and without plasmonic effect. We could see that the signal intensity gradually approached constant at around 8 min (Figure 2.12b, red open circles). The Raman spectrum at 8 min is shown in Figure 2.12a. The residual signal intensity indicates that a certain amount of molecules was captured by the plasmonic tweezer when electric bias was turned off. At 11 min, the plasmonic tweezer was turned off, the Raman signal intensity subsequently dropped back to original state (Stage 3), which has the same trend as shown in Figure 2.12b. For comparison, we did a control experiment. The Raman intensity change was measured without the plasmonic tweezer effect (Figure 2.12b, black open squares). In Stage 1, under electrostatic force, the signal intensity again kept increasing. The black squares and red circles are overlapped with each other, indicating the repeatability of the experimental results. Then the Raman intensity started to decrease right after the electrostatic bias was turned off at 5 min and at around 8 min the Raman signal intensity was back to the original state. The control experiment again demonstrates the ability of the plasmonic tweezer to capture molecules.

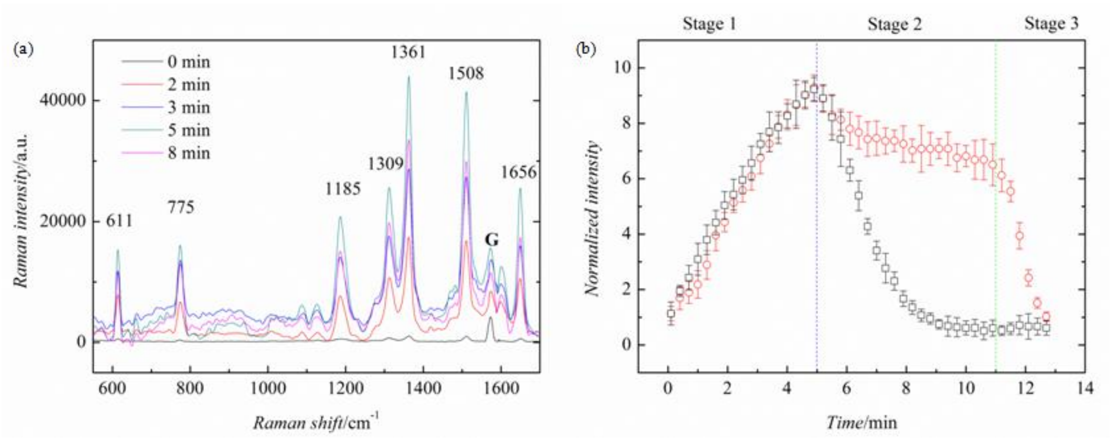

Figure 2.12. Combined effect of plasmonic tweezer and electrostatic force. (a) Raman spectra of R6G at0 min, 2 min, 3 min, 5 min and 8 min (with plasmonic tweezer on). The intensity of the graphene G peak kept constant; (b) The change of Raman signal intensity (1361 cm^{-1} peak) with time. The Raman intensity is normalized to the intensity of graphene G peak. Stage 1: (0 min - 5 min) the electrostatic bias on and plasmonic tweezer off; Stage 2: (5 min - 11 min) for red circles electrostatic bias off and plasmonic tweezer on, and for black squares electrostatic bias off and plasmonic tweezer off; Stage 3: (from 11 min) electrostatic bias off and plasmonic tweezer off.

In sufficiently dilute solution of R6G (~10^{-9} M), we observed the capture of single molecules by combining the plasmonic tweezer effect and the electrostatic force. The acquisition time is 1 s. First the voltage bias and plasmonic tweezer was turned on at 1 min. At about 2 min there was an abrupt change of the Raman signal intensity (Figure 2.13a, black curve), indicating that there was R6G molecule being attracted to the SERS hybrid platform. Then the electrostatic bias was turned off at ~3 min and the Raman signal intensity kept unchanged until around 7 min, which represented that the molecule was kept on the nanostructured surface. After 7 min, the signal disappeared and the captured molecule jumped out of the trap and left the surface. For comparison, when we turned off the plasmonic tweezer, the Raman signal intensity jumped back to the original level almost immediately after the voltage bias was turned off (Figure 2.13a, red curve). In Figure 2.13b, black curve and red curve represent the Raman spectra at 4 min with and without plasmonic tweezer respectively. This phenomenon was observed upon repeated experiments of up to 10 times. The only variation was the time it took for the abrupt increase of the Raman signal which varied between 1 and 10 mins after the electrostatic bias was turned off. In this study the acquisition time is kept at 1 s instead of using a longer time so that the molecular motion would not be interrupted especially when the plasmonic tweezer is off. In real application the signal can be greatly enhanced by increasing the collection duration or accumulation times. By combining these two effects, we successfully captured and detected single molecules. This indicates a possible way for precisely control of single molecules.

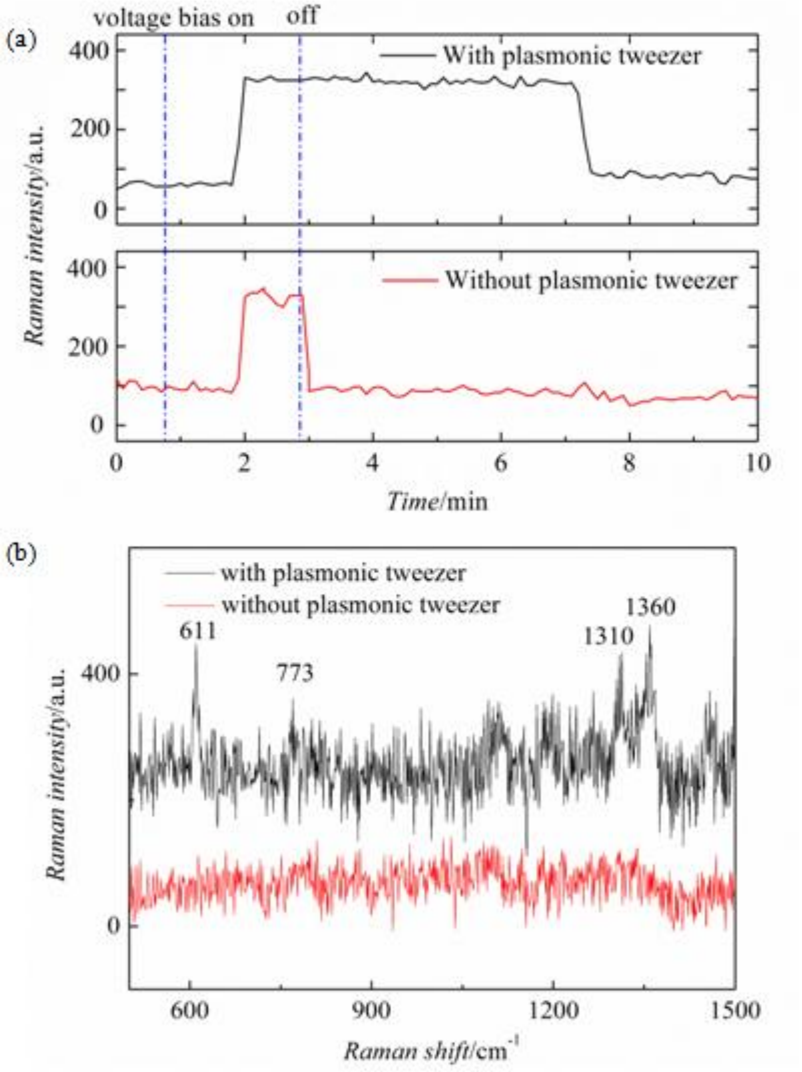

Figure 2.13. Combined effect of plasmonic tweezer and electrostatic force in dilute solution of R6G (10^{-9} M). (a) Change of Raman signal intensity of R6G (1361 cm^{-1} peak) with time. (black curve: plasmonic tweezer on; red curve: plasmonic tweezer off). (b) Corresponding Raman spectra of R6G at 4 min (black curve: plasmonic tweezer on; red curve: plasmonic tweezer off).

Above results demonstrate that the plasmonic tweezer can be employed to capture the molecules. However, the plasmonic tweezer effect itself works inefficiently since only the molecules that are brought to the nanostructured surface by the Brownian motion can be captured. The electrostatic force exactly compensates this limitation so that the capture of single molecules in dilute solution can be obtained. This effect is also a self-aligned technique since the hot spots serve as trapping locations and surface-enhanced locations for Raman scattering process simultaneously. Naturally it becomes an ideal method for enhancing the Raman sensitivity. The trapping duration is supposed to be able to adjust by changing the strength of the trapping potential and this can be achieved by changing the intensity of incident laser power or varying the plasmonic structure. Furthermore, most of biomolecules have an inherent dipole moment, so under the EM field gradient the biomolecules may align on a preferable direction. This provides the capability of another degree for molecular control - orientation control - other than the positional control. If the position and orientation of biomolecules could be precisely controlled, it allows the possibility of studying the properties and functions of these biomolecules in various biological processes.

2.5 Conclusion

In conclusion, we demonstrated a self-aligned trapping method by combining the plasmonic tweezer and the electrostatic force, which could be an effective method for increasing the sensitivity and selectivity of bio-sensing techniques. The surface plasmon field distribution and force density field distribution was calculated through FDTD solution. The calculation results indicate highly localized (~10 nm) and very intense attraction force field (>10^{11} N m^{-3}) around hot spots. These hot spots give rise to the ability of precisely positional control of molecules and a high enhancement factor for SERS detection. The molecular motion under electrostatic force was simulated using COMSOL Multiphysics. A dramatic increase of the SERS signal intensity and a saturation phenomenon were observed under plasmonic tweezer effect. The attraction/repulsion cycles of biomolecules and selective molecular manipulation based on molecular mass and charge state were demonstrated using electrostatic force. By combining plasmonic tweezer and electrostatic force, we successfully observed the capture of molecules by the nano-pyramid surface. Surprisingly even in sufficiently dilute solution (10^{-9} *M*), we could obtain the capture of single molecules by plasmonic tweezer after they were guided to individual hot spot by electrostatic force. The combined method offers a new approach for enhancing the sensitivity and selectivity of biosensing technique and a noninvasive way for precisely control and alignment of molecules in solution. This method could become a powerful tool in studying of various biological systems, such as the protein secondary structure, the metabolism of cells, etc.

References

1 Reimer, U.; Reineke, U.; Schneider-Mergener, J. Peptide Arrays: From Macro to Micro. *Curr. Opin. Biotechnol.* **2002**, *13*, 315-320.

2 Langer, R.; Peppas, N. A. Advances in Biomaterials, Drug Delivery, and Bionanotechnology. *AIChE J.* **2003**, *49*, 2990-3006.

3 Ziauddin, J.; Sabatini, D. M. Microarrays of Cells Expressing Defined cDNAs. *Nature* **2001**, *411*, 107-110.

4 Hook, A. L.; Thissen, H.; Voelcker, N. H. Surface Manipulation of Biomolecules for Cell Microarray Applications. *Trends Biotechnol.* **2006**, *24*, 471-477.

5 Abgrall, P.; Nguyen, N. T. Nanofluidic Devices and Their Applications. *Anal. Chem.* **2008**, *80*, 2326-2341.

6 Zhou, Q.; Li, X.; Fan, Q.; Zhang, X.; Zheng, J. Charge Transfer between Metal Nanoparticles Interconnected with a Functionalized Molecule Probed by Surface‐Enhanced Raman Spectroscopy. *Angew. Chem.* **2006**, *118*, 4074-4077.

7 Leyton, P.; Sanchez-Cortes , S.; Garcia-Ramos , J. V. ; Domingo , C. ; Campos-Vallette , M.; Saitz , C. ; Clavijo R. E. Selective Molecular Recognition of Polycyclic Aromatic Hydrocarbons (PAHs) on Calix [4] Arene-functionalized Ag Nanoparticles by Surface-enhanced Raman Scattering. *J. Phys. Chem. B* **2004**, *108*, 17484-17490.

8 Anderson, M. S. Locally Enhanced Raman Spectroscopy with an Atomic Force Microscope. *Appl. Phys. Lett.* **2000**, *76*, 3130-3132.

9 Xie, C.; Mace, J.; Dinno, M. A.; Li, Y. Q.; Tang, W.; Newton, R. J.; Gemperline, P. J.

Identification of Single Bacterial Cells in Aqueous Solution Using Confocal Laser Tweezers Raman Spectroscopy. *Anal. Chem.* **2005**, *77*, 4390-4397.

10 Svedberg, F.; Li, Z.; Xu, H.; Käll, M. Creating Hot Nanoparticle Pairs for Surface-enhanced Raman Spectroscopy through Optical Manipulation. *Nano Lett.* **2006**, *6*, 2639-2641.

11 Ming, T.; Kou, X.; Chen, H.; Wang, T.; Tam, H. L.; Cheah, K. W.; Chen, J. Y.; Wang, J. Ordered Gold Nanostructure Assemblies Formed by Droplet Evaporation. *Angew. Chem.* **2008**, *120*, 9831-9836.

12 Kuemin, C.; Nowack, L.; Bozano, L.; Spencer, N. D.; Wolf, H. Oriented Assembly of Gold Nanorods on the Single - Particle Level. *Adv. Funct. Mater.* **2012**, *22*, 702-708.

13 Kim, K.; Han, H. S.; Choi, I.; Lee, C.; Hong, S.; Suh, S.; Lee, L. P.; Kang, T. Interfacial Liquid-state Surface-enhanced Raman Spectroscopy. *Nat. Commun.* **2013**, *4*.

14 Liu, H; Yang, Z.; Meng, L.; Sun, Y.; Wang, J.; Yang, L.; Liu, J.; Tian, Z. Three-dimensional and Time-ordered Surface-enhanced Raman Scattering Hotspot Matrix. *J. Am. Chem. Soc.* **2014**, *136*, 5332-5341.

15 A. Ashkin, J. M. Dziedzic, *Appl. Phys. Lett.*, **1974**, *24*, 586.

16 J. W. Chan, A. P. Esposito, C. E. Talley, C. W. Hollars, S. M. Lane, T. Huser, *Anal. Chem.*, **2004**, *76*, 599.

17 C. Xie, M. A. Dinno, Y. Q. Li, *Opt. Lett.*, **2002**, *27*, 249.

18 C. Xie, J. Mace, M. A. Dinno, Y. Q. Li, W. Tang, R. J. Newton, P. J. Gemperline, *Anal. Chem.*, **2005**, *77*, 4390.

19 H. Tang, H. Yao, G. Wang, Y. Wang, Y. Q. Li, M. Feng, *Opt. Express*, **2007**, *15*,

12708.

20 M. M. Wang, E. Tu, D. E. Raymond, J. M. Yang, H. Zhang, N. Hagen, B. Dees, E. M. Mercer, A. H. Forster, I. Kariv, P. J. Marchand, *Nat. Biotechnol.*, **2005**, *23,* 83.

21 D. G. Grier, *Nature,* **2003**, *424,* 810.

22 A. N. Grigorenko, N. W. Roberts, M. R. Dickinson, Y. Zhang, *Nat. Photonics,* **2008**, *2*, 365.

23 K. Wang, E. Schonbrun, P. Steinvurzel, K. B. Crozier, *Nat. Commun.*, **2011**, *2*, 469.

24 S. K. Mondal, S. S. Pal, P. Kapur, *Opt. Express*, **2012**, *20,* 16180.

25 M. L. Juan, M. Righini, R. Quidant, *Nat. Photonics*, **2011**, *5*, 349.

26 L. Novotny, R. X. Bian, X. S. Xie, *Phys. Rev. Lett.*, **1997**, *79,* 645.

27 O. J.Martin, C. Girard, *Appl. Phys. Lett.*, **1997**, *70*, 705.

28 A. V. Zayats, I. I. Smolyaninov, *J. Opt. A: Pure Appl. Opt.*, **2003**, *5,* S16.

29 Giuliano, K. A.; Post, P. L.; Hahn, K. M.; Taylor, D. L. Fluorescent Protein Biosensors: Measurement of Molecular Dynamics in Living Cells. *Annu. Rev. Biophys. Biomol. Struct.* **1995**, *24*, 405-434.

30 Sönnichsen, C.; Reinhard, B. M.; Liphardt, J.; Alivisatos, A. P. A Molecular Ruler Based on Plasmon Coupling of Single Gold and Silver Nanoparticles. *Nat. Biotechnol.* **2005**, *23*, 741-745.

31 Eggeling, C.; Fries, J. R.; Brand, L.; Günther, R.; Seidel, C. A. M. Monitoring Conformational Dynamics of a Single Molecule by Selective Fluorescence Spectroscopy. *Proc. Natl. Acad. Sci.* **1998**, *95*, 1556-1561.

32 Endo, T.; Kerman, K.; Nagatani, N.; Takamura, Y.; Tamiya, E. Label-free Detection of

Peptide Nucleic Acid-DNA Hybridization Using Localized Surface Plasmon Resonance Based Optical Biosensor. *Anal. Chem.* **2005**, *77*, 6976-6984.

33 Li, X.; Gan, L.; Ou, Q.; Zhang, X.; Cai, S.; Wu, D.; Chen, M.; Xia, Y.; Chen, J.; Yang, B. Enzyme-free and Label-free Fluorescence Sensor for the Detection of Liver Cancer Related Short Gene. *Biosens. Bioelectron.* **2015**, *66*, 399-404.

34 Gogoi, S. K.; Gopinath, P.; Paul, A.; Ramesh, A.; Ghosh, S. S.; Chattopadhyay, A. Green Fluorescent Protein-Expressing Escherichia c oli as a Model System for Investigating the Antimicrobial Activities of Silver Nanoparticles. *Langmuir* **2006**, *22*, 9322-9328.

35 Gramlich, P. M.; Wirges, C. T.; Manetto, A.; Carell, T. Postsynthetic DNA Modification through the Copper‐Catalyzed Azide–Alkyne Cycloaddition Reaction. *Angew. Chem., Int. Ed.* **2008**, *47*, 8350-8358.

36 Anker, J. N.; Hall, W. P.; Lyandres, O.; Shah, N. C.; Zhao, J.; Van Duyne, R. P. Biosensing with Plasmonic Nanosensors. *Nat. Mater.* **2008**, *7*, 442-453.

37 Fan, Z.; Kanchanapally, R.; Ray, P. C. Hybrid Graphene Oxide Based Ultrasensitive SERS Probe for Label-free Biosensing. *J. Phys. Chem. Lett.* **2013**, *4*, 3813-3818.

38 Willets, K. A.; Van Duyne, R. P. Localized Surface Plasmon Resonance Spectroscopy and Sensing. *Annu. Rev. Phys. Chem.* **2007**, *58*, 267-297.

39 Fraire, J. C.; Pérez, L. A.; Coronado, E. A. Rational Design of Plasmonic Nanostructures for Biomolecular Detection: Interplay between Theory and Experiments. *ACS Nano* **2012**, *6*, 3441-3452.

40 Wang, P.; Zhang, W.; Liang, O.; Pantoja, M.; Katzer, J.; Schroeder, T.; Xie, Y. H.

Giant Optical Response from Graphene–plasmonic System. *ACS Nano* **2012**, *6*, 6244-6249.

41 Y. Harada, T. Asakura, *Opt. Commun.*, **1996**, *124*, 529.

42 Z. Xu, G. He, M. D. Elking, *J. Chem. Phys.*, **1997**, *107*, 3947.

43 Madura, J. D.; Briggs, J. M.; Wade, R. C.; Davis, M. E.; Luty, B. A.; Ilin, A.; Antosiewiczb, J.; Gilsong, M. K.; Bagherif, B.; Scottf, L. R.; et al. Electrostatics and Diffusion of Molecules in Solution: Simulations with the University of Houston Brownian Dynamics Program. *Comput. Phys. Commun.* **1995**, *91*, 57-95.

44 E. O. Ganbold, J. H. Park, U. Dembereldorj, K. S. Ock, S. W. Joo, *J. Raman Spectrosc.*, **2011**, *42*, 1614.

45 Abgrall, P.; Gue, A. M. Lab-on-chip Technologies: Making a Microfluidic Network and Coupling It into a Complete Microsystem—a Review. *J. Micromech. Microeng.* **2007**, 17, R15.

Chapter 3   Plasmon Powered Hybrid Platform for SERS

3.1 Introduction

The electromagnetic (EM) enhancement is the major mechanism for SERS enhancement, in which local EM field is enhanced due to the excitation of localized surface plasmon (LSP) of metal nanostructures. This enhancement of EM field accounts for the increase of the Raman signal intensity of adsorbates on (typically) metallic surfaces. To achieve strong Raman signal, highly localized EM field is required in SERS metallic nanostructures. Tremendous efforts have been spent on engineering the structure of metal nanostructures to obtain high local EM field. Among these nanostructures, nanogap formed between metal nanoparticles (NPs) is a highly effective SERS nanostructure, which can boost the Raman signal up to ~10^9 times. The deficiency of this kind of structure is the small detection volume, typically below 10 nm. With such small size of detection volume, it is difficult for large biomolecules like proteins and other biological entities like cells to fit in the gap where the hot spots are located. Compared with nanogap between adjacent NPs, the hybrid platform, graphene-Au pyramid structure, has distinct advantages. The nanopyramid array is an open structure, in which hot spots locate between neighboring pyramids. As such, large biomolecules and biological entities can easily move into these regions and their Raman signals can be enhanced. By introducing a single layer graphene the hybrid platform is capable of providing a bio-friendly surface and a quantitative analysis. Based on such properties, this hybrid platform is an powerful tool for bio-sensing using SERS. In this chapter, we present the applications of the hybrid platform in the bio-sensing field, in particular, the characterization of exosomes and T-cells.

3.1.1 SERS and Its Applications in Bio-sensing

Raman spectroscopy is a widely used, non-destructive method for determining the chemical bonding of molecules and then providing the structural fingerprint by which molecules can be identified[1]. Its label-free nature makes it a natural choice for the studies of biological samples over decades[2]. The most noticeable drawback of Raman spectroscopy is the extremely low yield and the resulting low detection sensitivity[3]. As a derivative technique of Raman spectroscopy, SERS is a technique capable of boosting by orders of magnitude the Raman signals from molecules located within tens of nanometers of metallic nanostructures[4,5,6,7].

There are mainly two mechanisms that explain SERS effect. One is electromagnetic (EM) enhancement mechanism, and the other is chemical enhancement mechanism. In EM enhancement, excitation light interacts with nanosized metallic SERS substrates and generates LSPR. Molecules absorbed at metallic surfaces experience a large amplification of laser field locally due to plasmon resonance while undergoing Raman processes, and thus generate enhanced Raman signal. Majority of SERS effects are due to EM enhancement on metallic nanostructures. Chemical enhancement is mainly due to charge transfer mechanism between molecules and substrate surfaces, and the magnitude of Raman signal enhancement is very low compared with EM enhancement. Therefore, we will focus on SERS effects due to EM enhancement. To quantify SERS enhancement effect, the concept of SERS enhancement factor (EF) was brought up. SERS EF reflects how much the Raman signal can be boosted. A commonly used approximation is that SERS EF is proportional to the fourth power of the magnitude of electric field ($|E|^4$).[8] Typical SERS EF of metallic SERS substrates is from 10^3 to 10^{14}. Various metallic (mainly Ag and Au) nanostructures[9,10,11,12,13] have been developed and fabricated to achieve strong local electric field and high SERS EFs.

SERS technique has been widely explored for *in vivo* biosensing due to its high sensitivity. SERS *in vivo* biosensing can be generally classified into two methods, intrinsic and extrinsic biosensing. Intrinsic SERS biosensing directly provides Raman signature for analytes of interest, such as protein, DNA strand, or small molecules. Extrinsic SERS biosensing provides Raman signature of a molecule (or Raman reporter) with an intense and distinguishable Raman features, and analyte of interest is associated with this molecule. Bisosensing of target analyte is based on spectra of Raman reporter molecules. Therefore, extrinsic SERS biosensing is an indirect sensing method.

Intrinsic SERS biosensing is also known as lab-free SERS biosensing sometimes. In label-free SERS biosensing, SERS substrates contact with target anlayte and generate strong SERS signal, which is used to identify interested molecules or do quantification. There is few study of applying label-free SERS in *in vivo* system. The Van Duyne group first demonstrated *in vivo* label-free SERS detection of the glucose from the interstitial fluid of a rat. The SERS substrate used in this study was the silver film over nanosphere (AgFON) functionalized with a self-assembled monolayer (SAM). The SERS substrate was implanted under the skin of a rat in a way that the fluid was in contact with the SERS metallic surface and the laser was focused on the SERS substrate through a glass window. One major advantage of label-free SERS is that it can provide rich spectroscopic information for detection and identification without labeling, and thus reduce the time for detection. The disadvantages of label-free SERS include the lack of specificity and the difficulty of identifying analytes from the spectroscopic information for large biomolecules, like proteins and DNA.

Compared with intrinsic or label-free SERS, extrinsic SERS is widely explored for *in vivo* biosensing. Extrinsic SERS relies on SERS nanoparticle tags (or nanotags) to identify analyte of interest. A SERS nanotag contains a metal nanoparticle core, Raman reporters on the metal surface, and a biocompatible layer which encases the metal particle and Raman reporters, as shown in Figure 3.1. Commonly used biocompatible layers are polyethylene glycol (PEG) and silica, which maintain colloidal stability and prevent interaction of the Raman reporter with the external environment. This biocompatible layer can then be further functionalized with targeting agents toward specific receptors. The targeting agents on the nanotags will provide the detection specificity through binding on the receptor on the target anlaytes. When the SERS nanotags accumulate on the analyte (e.g. cells), Raman signal of Raman reporter molecules can be enhanced and detected. Biosensing of the analyte is achieved through measuring the Raman signal of reporter molecules. SERS nanotags have been used for *in vivo* tumor detection in mouse. Nie and co-workers used functionalized Au nanoparticles as SERS nanotags to identify tumor in mouse. After injecting NPs into the mouse from the tail vein, SERS signal could be detected from a targeted tumor site up to 2 cm below the skin. The major advantage of using SERS nanotags is that extrinsic Raman reporter molecules can overcome background signals from a complex biological matrix and associate with specific biomolecules.

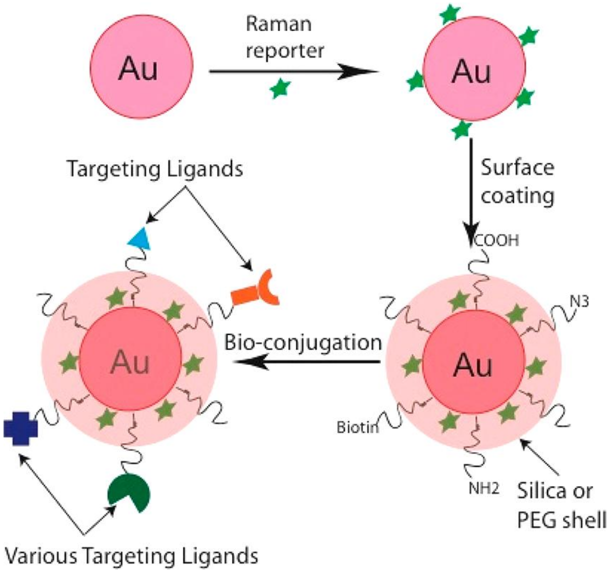

Figure 3.1. Structure of biofunctionalized SERS nanoparticle tags, consisting of a metal nanoparticle core, adsorbed Raman reporters on the metal surface (green stars), a biocompatible layer (orange layer), and targeting ligands.

3.1.2 Performance of the Hybrid Platform in Bio-sensing

The hybrid platform consists of a graphene and Au nanopyramid structure[14,15,16] (Raman enhancement factor of up to 10^{12}). Figure 3.2a is a schematic presentation of the hybrid platform. Figure 3.2b is a representative SEM image of the substrate. In our experiments, the base dimension of the pyramids is 200 nm and the center-to-center distance between adjacent pyramids is 400 nm. Graphene provides a bio-compatible surface, independent of the type of metal used for supporting plasmon resonance. Graphene also serves as a hotspot marker that indicates the intensity of individual hotspot of plasmon resonance. The periodic Au nanopyramid structure with tunable size and sharpness can be fabricated via a wafer-scale bottom-up templating technology. The local electromagnetic (EM) field distribution is simulated using FDTD Solutions (Figure 3.2c), which is based on finite-difference time-domain method (FDTD).

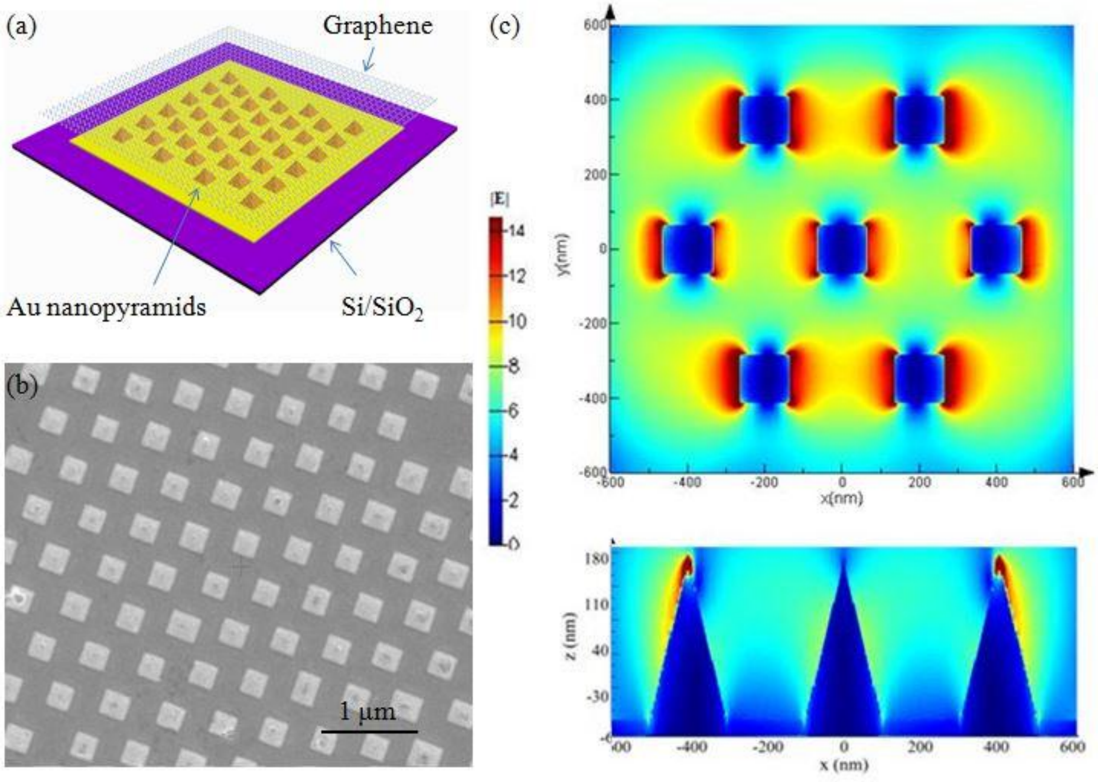

Figure 3.2. SERS hybrid platform. (a) Schematic diagram of the hybrid platform. (b) SEM image of the hybrid platform. (c) The electromagnetic (EM) field distribution simulated by FDTD at the input wavelength of 785 nm (top: xy-view; bottom: xz view). Color bar represents the electric field intensity.

The sensitivity of the SERS hybrid platform was demonstrated using two types of molecules (Figure 3.3)[15]. Lysozyme, a type of simple protein commonly used as the standard in the study of bio-molecules, is used. The active fluorescent molecule R6G is also used as a reference. Figure 3.3a-b show the average Raman intensities of R6G and lysozyme deposited on the hybrid platform at various molecular concentrations. SERS signal of R6G with concentration down to 10^{-14} M (equivalent to ~0.0015 molecules per μm^2 on average of the surface area) as well as lysozyme with concentration as low as 10^{-12} M (~0.15 molecules per μm^2 on average of the surface area) can be detected. The detection efficiency can be further increased with the help of graphene over Au pyramids. At low concentration limits such as 10^{-14} M, the knowledge of the location of the hot spots greatly shortens the time it takes to locate the sparse molecular Raman signal by being indicated by graphene signals.

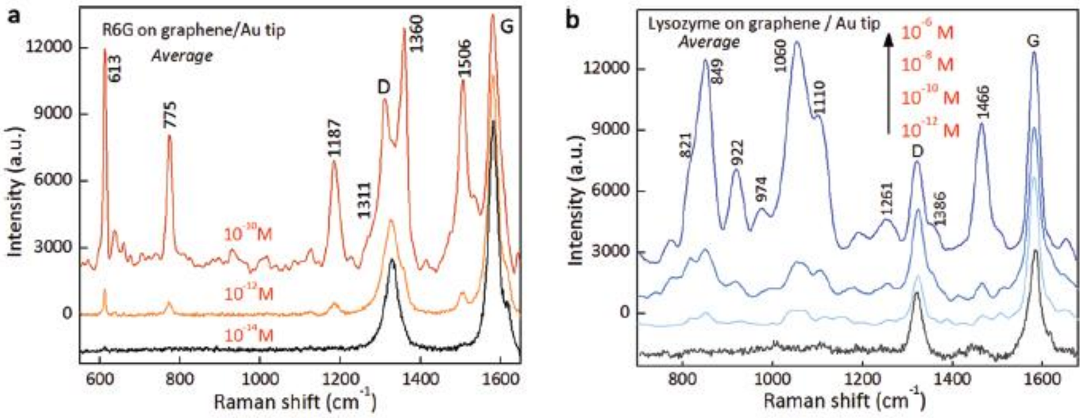

Figure 3.3 (a) Raman spectra of R6G on graphene hybrid structure with 3 different concentrations (10^{-10} M, ~15 molecules/μm^2 , 10^{-12} M, ~0.15 molecules/μm^2, 10^{-14} M, ~0.0015 molecules/μm^2) (b) Raman spectra of lysozyme on graphene hybrid structure with 4 different concentrations (10^{-6} M, 10^{-8} M, 10^{-10} M, 10^{-12} M). The laser excitation wavelength is 633 nm.[15]

3.1.3 Exosomes

Extracellular vesicles (EVs) are complex structures composed of a lipid bilayer that contains transmembrane proteins and encloses soluble hydrophilic components derived from the cytosol of the donor cell[17]. The EVs play an important role in the intercellular communications by serving as vehicles for transfer between cells[18]. Exosomes are the most abundant and best investigated type of EVs in the size range of 30-200 nm[19]. Among the EVs, exosomes are highly enriched with protein, signaling lipids, and genetic material, including mRNAs and miRNAs, all combining to mediate a variety of biological functions[20]. They have attracted increasingly amount of attention in recent years because of their potential to be used as a valuable source for diagnostic biomarkers for detecting various diseases and understanding their pathogenesis, such as cancer, neurodegenerative disease[21,22,23,24,25] and others. However, the exact biological function of exosomes and mechanisms of action are yet to be fully elucidated[26,27,28,29]. Figure 3.4 illustrates the generation of exosomes and another type of EVs, microvesicles.

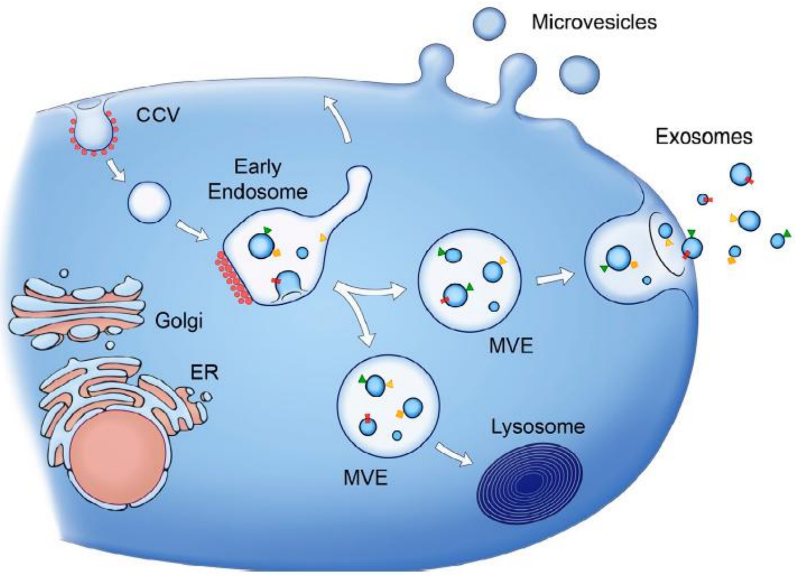

Figure 3.4. Release of microvesicles (MVs) and exosomes. MVs bud directly from the plasma membrane, whereas exosomes are represented by small vesicles of different sizes that are formed as the intraluminal vesicles (ILVs) by budding into early endosomes and multivesicular endosomes (MVEs) and are released by fusion of MVEs with the plasma membrane. Membrane-associated and transmembrane proteins on vesicles are represented as triangles and rectangles, respectively. Arrows represent proposed directions of protein and lipid transport between organelles and between MVEs and the plasma membrane for exosome secretion.

Recently SERS have been employed to characterize exosomes[30,31,32,33], but identification of single exosome including the type of cells it is secreted from and differentiation of the exosomes from other extracellular vesicles and fragments of various biological entities such as proteins and cells is still lacking. There are currently several reports in the literature on the identification of exosomes using a combination of experimental techniques [21, 24, 34]. While each of these approaches has its own strengths and weakness, a feature common to all is the uncertainty that the signals obtained using different techniques are indeed derived from exosomes as opposed to remnants of other biological entities inadvertently mixed in with the analyte.

In this chapter, we present rigorous correlative studies between SERS mapping and SEM aiming at eliminating the above mentioned uncertainty. By characterizing the bio-chemical content of exosomes we differentiated them from extracellular vesicles of different biological origin or from scattered biomolecules. By incorporating with principal component analysis (PCA), the hybrid platform presents a high specificity for differentiation and classification of various categories of biological samples. In this work, the Raman signatures of exosomes from different sources were first collected through the hybrid platform. Western blot was employed in parallel to detect the specific proteins of the investigated samples and dynamic light scattering (DLS) was used to determine their size distribution. Due to the smaller size of exosomes (<200 nm), they are difficult to directly visualize under Raman microscope, which put challenges to guarantee the source of the Raman signal. To make sure that the Raman spectrum was coming from the exosomes instead of scattered biomolecules (e.g. proteins, lipids or nucleic acid) or other extracellular vesicles, a comparison experiment was conducted by statistically correlating the density of vesicles measured from electron microscopy with that from Raman mapping results. In the meantime, single intact exosome was mapped out through SERS spectroscopy. To verify the anticipated the "finger print" capability of Raman spectroscopy, the exosomes from different sources were characterized and successfully differentiated by principal component analysis (PCA).

3.1.4 Chimeric Antigen Receptor (CAR) T-cells for Cancer Treatment

Historically, there have been three pillars of cancer treatment: surgery, chemotherapy, and radiotherapy. In recent years, immunotherapy has emerged as a possible fourth pillar, targeting cancer not by its anatomic location or propensity to divide, but by the inherent mechanisms the immune system uses to distinguish between healthy and pathologic tissue. Adoptive T cell therapy (ACT) is one stone in this new pillar, a potentially powerful approach to cancer treatment that relies on the infusion of tumor-specific T-cells. From a theoretical standpoint, cancer immunotherapy using T cells has long been of interest. Adaptive immunity has numerous beneficial properties that make it amenable for cancer treatment: (1) T cell responses are specific, and can thus potentially distinguish between healthy and cancerous tissue; (2) T cells responses are robust, undergoing up to 1,000-fold clonal expansion after activation; (3) T cell response can traffic to the site of antigen, suggesting a mechanism for eradication of distant metastases; and (4) T cell responses have memory, maintaining therapeutic effect for many years after initial treatment. Adoptive T-cell therapy has demonstrated clinical efficacy against advanced cancers[35]. In particular, multiple clinical trials have shown that T cells programmed to express antiCD19 chimeric antigen receptors (CARs) have curative potential against relapsed B-cell malignancies[36].

Accumulating clinical reports suggest that, in addition to patient-to-patient variations in tumor burden and overall health profile, the quality of individual T-cell products could significantly influence clinical outcome [37]. However, it remains unclear which T-cell characteristics are the most critical and predictive of anti-tumor efficacy, and if and how such characteristics could be promoted during T-cell manufacturing. As CAR-T cell technology advances toward broader clinical use, the ability to identify critical T-cell characteristics and systematically optimize CAR-T cell preparation has the potential to significantly improve the robustness of adoptive T-cell therapy.

In this chapter, the T-cells are characterized using the hybrid platform. Preliminary experiments are conducted on two types of T-cells, the simulated and unstimulated T-cells. The Raman spectra are analyzed by PCA, which shows a difference between these two types of T-cells. The preliminary results indicates potential applications of SERS in further studies of CAR-T cell.

3.2 Experimental Methods

3.2.1 Fabrication of Au Nanopyramids

The Au nanopyramid fabrication is based on sphere-lithography[38]. Figure 3.5 shows the fabrication process. Firstly, polystyrene (PS) nano-spheres (500 nm in diameter, Alfa Aesar) are coated on SiO_2 (50 nm)/Si wafer using scooping transfer method[39]. Before coating PS spheres, SiO_2/Si wafer is washed by Piranha solution (H_2SO_4:H_2O_2=3:1(volume ratio)) for 1h at 70 ℃ followed by de-ionized water (DI water) rinsing for 3 times. In scooping transfer process, a few drops of the diluted PS sphere suspension (5% aqueous PS sphere suspension mixed with an equal volume of ethanol) are introduced on the water surface using the partially immersed glass slide (2 cm × 10 cm). The glass slide is pretreated by a Piranha solution for 1 h at 70 ℃ and then rinsed by DI water for 3 times. After introducing PS spheres on the water surface, PS spheres will self-assembly and form closed-packed monolayers with hexagonal patterns. When about 80% of the water surface is covered with PS spheres, PS monolayer is transferred on SiO_2/Si substrates using simple scooping transfer method. Figure 3.6 (a) shows the SEM image of the PS spheres coated on SiO_2/Si substrate. The PS spheres/SiO_2/Si sample is then dry-etched by O_2 plasma (200W power, 50s) to reduce the size of PS sphere to about 250 nm (Figure 3.6 (b)).

After etching PS spheres, 50 nm Cr film is deposited on the as-prepared sample using electron beam deposition (Figure 3.5 step (3)). The PS spheres are then lift-off by ultra-sonicating the sample in acetone for 20 min, followed by DI water rinsing for 3 times. Figure 3.6 (c) shows the SEM image of the sample after PS lift-off. Using the Cr film (with small holes in the film) as mask, the 50 nm SiO_2 film beneath the Cr film is dry-etched by Oxford Plasmalab Plasma Etcher (25 sccm Ar, 25 sccm CHF_3, RIE power 200W, etch time 2min).

After etching SiO_2, the hole pattern is transferred on SiO_2 from Cr film. The sample is then etched in KOH aqueous solution (60 wt%) for 2 min at 60 ℃ to form pyramidal structure on Si surface (Figure 3.6(d)). The whole sample is then immersed into HF solution (30%) to remove SiO_2 and Cr layer. At this time, Si pyramidal mold (Figure 3.6(e)) fabrication has been finished. 200 nm Au film is deposited on the Si mode with pyramidal structure by sputtering. 5-min epoxy is used to glue the Au film on another SiO_2 (300 nm)/Si substrate, which is used to hold the Au nano-pyramids. After the epoxy cured at the room temperature, Au nano-pyramids are peeled off (Figure 3.5 step (9)).

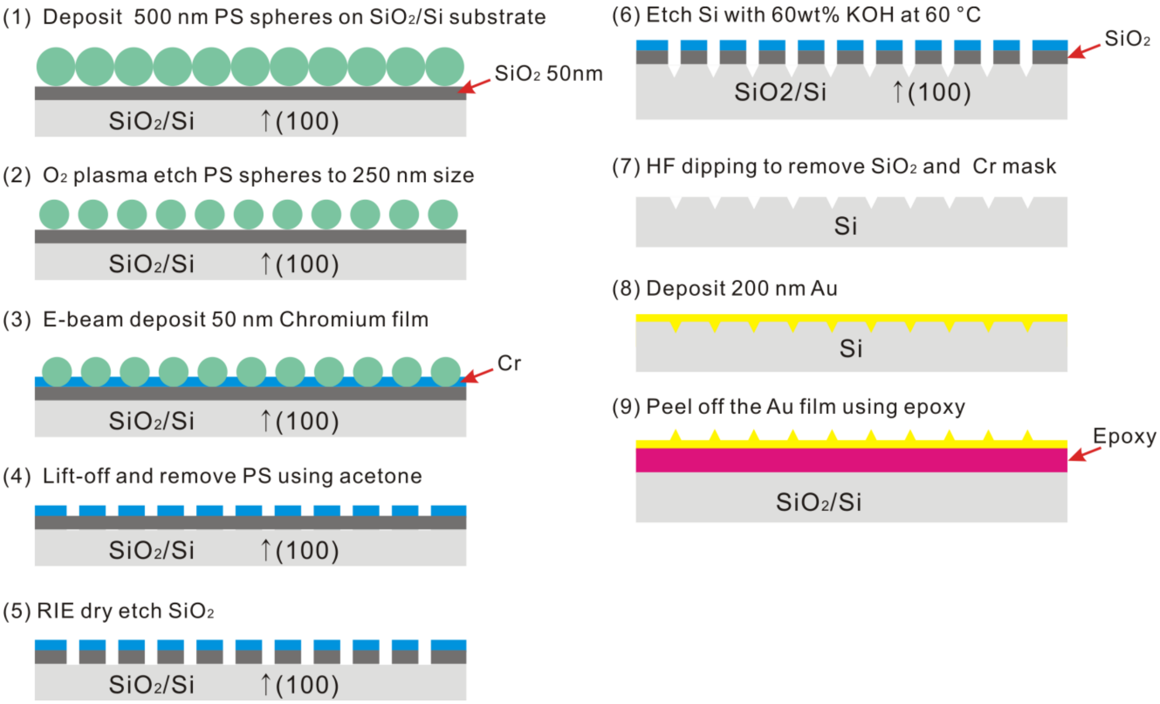

Figure 3.5 Schematic of the graphene/Au tip hybrid platform fabrication process.

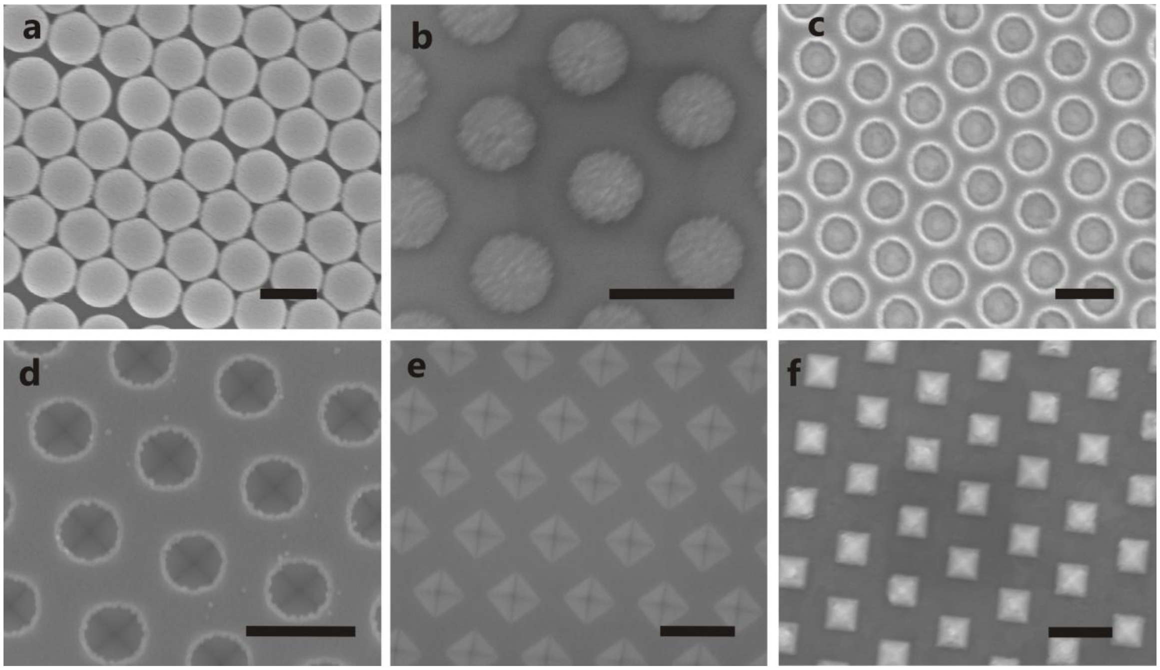

Figure 3.6 (a) SEM image of PS spheres on SiO_2/Si substrate. (b) SEM image of PS spheres after O_2 plasma

etching for 50s. (c) SEM image of the $Cr/SiO_2/Si$ sample after PS lift-off. (d) SEM image of the $Cr/SiO_2/Si$ sample after KOH etching. (e) SEM image of Si surface with inverse pyramidal hole. (f) SEM image Au nano-pyramids.

3.2.2 Growth and Transfer of Graphene

Graphene used in the experiment is grown by CVD method using copper foil. 25 micron-thick copper foil (Alfa Aesar #13382) is cut into a 2×2 inch square. The copper foil is loaded onto the center of a quartz chemical vapor deposition (CVD) chamber, the furnace is heated up to ~1025 ℃ under the flow of H_2 (~1000 sccm). After 30 minute annealing, the CVD growth is carried out with 20 Torr total pressure with CH_4 (~20 sccm) and H_2 (~1000 sccm) for 15 minutes. Then the chamber is cooled down to room temperature.

A thin layer of PMMA is uniformly spin coated on the synthesized graphene sample. The metal catalyst Cu is removed in an etching solution combined $CuCl_2$ (2.5 M) and HCl (37 wt%) aqueous solution with volume ratio of 4:1. Then the floating PMMA-graphene structure is transferred onto the surface of de-ionized water. Subsequently the sample is transferred onto the fiber facet with Au nanotriangle array using the similar method describe above, but the PMMA layer covering graphene is removed by acetone followed by isopropanol alcohol and deionized water washing.

3.2.3 Characterization Methods

Raman spectra were recorded using a Renishaw inVia Raman spectrometer under ambient conditions (20 ℃ and 1 atm). WiRe 4.2 software was used to control the whole system. The laser excitation wavelength was 785 nm. The power of the laser was kept at 5 mW to avoid sample overheating. The diameter of laser spot was 1.83 μm. The Raman measurements first were calibrated by the Si Raman mode at 520 cm^{-1}. The exosome solutions of 2 μl were applied to the SERS surface and allowed to air-dry before the measurement. The acquisition time was 1 second.

For TEM observation of isolated exosomes, pellets obtained after ultra-centrifugation at 110,000×*g* were loaded on Formvar carbon-coated EM grids by placing a small drop of PFA fixed exosomes over grid for 20min in a dry environment. The grid was then washed by floating the grid upside down on drops of filtered water. The exosomes were then post fixed in 1% glutaraldehyde for 5 min and contrasted successively in freshly prepared 2% uranyl acetate and 2% methylcellulose/0.4% uranyl acetate. Observations were made with a FEI Technai T20 electron microscope equipped with a thermionic tungsten filament and operated at an acceleration voltage of 200 kV. Images were taken with a cooled slow-scan CCD camera at a magnification of 80,000 ×.

The SEM imaging was taken by the Nova 230 Nano SEM. The accelerating voltage was 10 kV. The samples were viewed at an electron spot size of 3. The detector mode was through-the-lens" (TLD) secondary electron (SE) detector. The SERS substrate was mounted on the stage by double-coated carbon conductive tape. The images were taken at a magnification of 35,000 × and 50,000 ×.

Size distribution of EVs in liquid suspension were measured by dynamic light scattering (DLS), using a Zetasizer Nano instrument (Malvern Instruments Ltd, Worcestershire, UK). After isolation, the exosome pellet was reconstituted in 100 µl of filtered chilled PBS. Fifty microliters of purified exosomes were diluted in 1450 µl of filtered PBS and gently vortexed for 30 seconds to avoid aggregations. The whole volume was quickly put in a disposable cuvette and allowed to equilibrate for 30 secs at 25 ℃. The dispersant refractive index value used was 1.37 and a 20-mW helium-neon laser (632 nm) was used at an angle of 173 degrees. The size of the observed EVs populations was determined by Z-average and polydispersity index (PdI). Three independent measurements of 14 counts each were performed per samples and average values are presented.

Western blot analysis: protein concentration was calculated using a BCA protein assay kit (ThermoFisher Scientific, USA). Proteins were mixed with NuPAGE LDS Sample Buffer containing 5% β- mercaptoethanol and heated at 90 ℃ for 10 min. Twenty µg of protein extracts were fractionated on 4-12% NuPAGE Bis-Tris gels and electro-transferred onto nitrocellulose membranes (ThermoFisher Scientific, USA). The membranes were then blocked with 5% skim milk in tris-buffered saline (TBS)-0.1% Tween-20 (TBST) for 1 h at room temperature and then were incubated overnight at 4 ℃ with appropriate primary antibodies at 1:2,000 dilution in blocking solution. After three washes, with TBST for 10 min each, horseradish peroxidase-conjugated secondary antibodies (ThermoFisher Scientific) at 1:5,000 dilution in blocking solution were added and the membranes were incubated for 1 h at room temperature. SuperSignal West Femto maximum sensitivity substrate (Thermo Fisher Scientific, USA) was added and protein bands were visualized using a Gel-Doc apparatus (Syngene, USA).

3.2.4 Exosomes Isolation Method

One type of exosomes were isolated from fetal bovine serum (FBS), which was procured from Invitrogen, USA. Two types of exosomes were isolated from human lung cancer cell lines, HCC827 and H1975, which were obtained from ATCC and cultured in 75 cm^2 tissue culture flasks. Cells were cultured in conditioned medium, depleted of contaminating exosomes and protein aggregates prior to exosome isolation. Supernatants were collected 48-72 h after changing the medium for exosomes isolation[40]. Peripheral blood was collected by venipuncture using a BD vacutainer push button blood collection kit and left to coagulate in silicone coated serum collection tubes for 20 min at room temperature. After centrifugation at 1,500 *g* for 15 min, serum was collected and either processed immediately or stored at -80 ℃. After thawing quickly in 37 ℃ water bath, protease and phosphatase inhibitors were added and the serum from either source was diluted ten times with chilled PBS. Diluted serum or cell culture supernatants was centrifuged at 2,000 *g* and 4 ℃ for 20 min and then further centrifuged at 12,000 *g* and 4 ℃ for 45 min to remove small debris. The supernatants were filtered using 0.22-μm pore filters, followed by ultracentrifugation (Model, L8-M70, Beckman Coulter, USA) at 110,000 *g* and 4 ℃

for 2 h. The resulting pellets were re-suspended in chilled PBS and again ultra-centrifuged at 110,000 *g* and 4 ℃ for 70 min. The final pellet of exosomes was re-suspended, in 50–100 μl chilled PBS for NTA measurement, in a 2% paraformaldehyde (PFA) solution in water for SERS and TEM experiments, or lysed in RIPA buffer, aliquoted, and stored at –80 ℃ for Western blot analysis. Exosomes from FBS and human serum was also isolated using ExoQuick® exosome precipitation solution (System Biosciences, USA) following manufacturers' instructions. Following kit isolation of exosomes, samples were passed through 0.22uM filters to remove larger vesicles and aggregates.

3.3 SERS Study on Exosomes

3.3.1 SERS Characterization of Single Exosomes.

Exosomes were isolated from fetal bovine serum (FBS) by series of differential centrifugation, ultrafiltration and ultracentrifugation. First the Raman spectrum of the isolated exosomes was collected using the SERS hybrid platform. The size distribution of isolated vesicles was determined by dynamic light scattering (DLS) analysis (Figure 3.7a). The purity of exosomes was verified by western blot analysis using exosomal marker proteins (Figure 3.7b). The DLS data indicates that the size distributions of the isolated vesicles, both by sequential centrifugation with ultrafiltration and by using commercially available exosome isolation kit, are well in range as previously reported. The occurrence of marker protein bands as seen in the western blot experiment confirmed the presence of exosomes in investigated sample fractions.

Before measurement, 2 μl of solution containing exosomes was dropped onto the hybrid platform and dried for 20 min. The wavelength of the laser beam was set at 785 nm. The acquisition time was 1 second and in total 100 spectra were collected. Raman spectrum presented in Figure 3.8 is the average of several spectra (~100 collections) acquired over different spots. The band assignments are listed in Table 3.1[41].

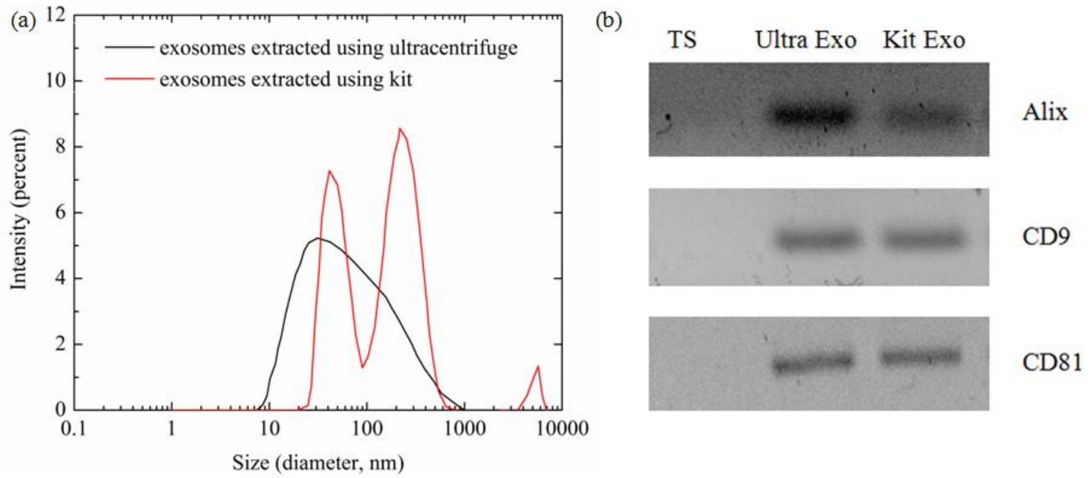

Figure 3.7. Characterization of exosomes extracted by ultracentrifugation and ExoQuick kit. (a) DLS size distribution analysis of exosomes. (b) Western blot analysis of exosomal marker proteins. CD9 and CD81 are both markers for extracellular vesicles (including exosomes and ectosomes), while Alix is ESCRT-related proteins specific for MVB formation (exosomes only). TS: total serum; Ultra Exo: Exosomes isolated by ultracentrifugation; Kit Exo: Exosomes isolated using ExoQuick exosome precipitation solution. Loading amount 25 μg/well.

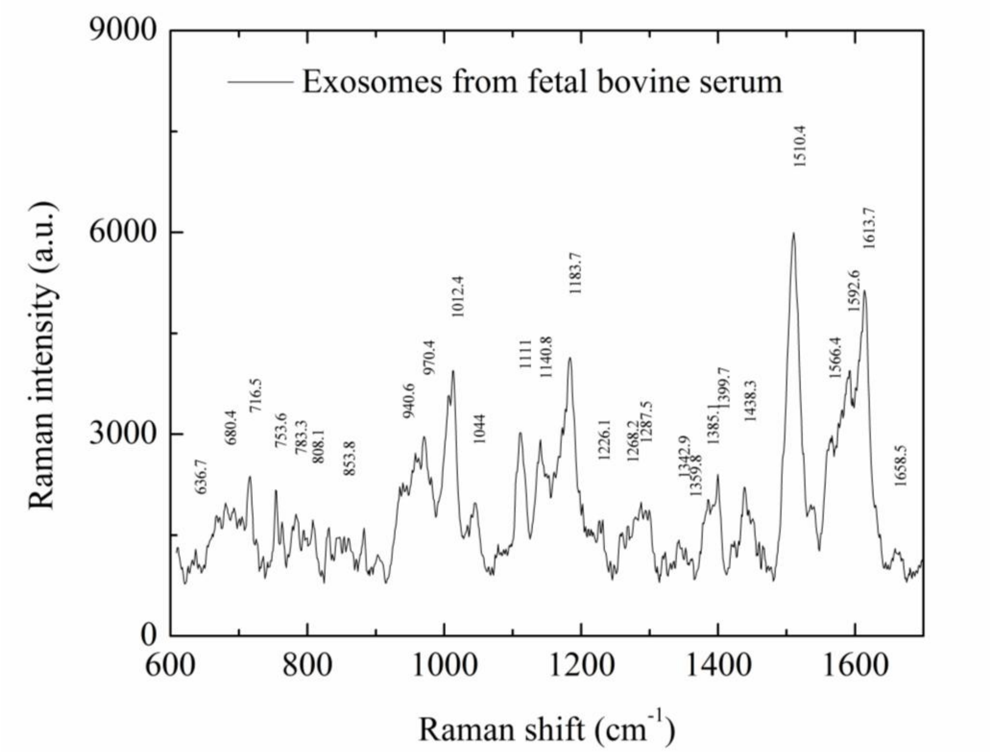

Figure 3.8 Raman spectrum of the exosomes isolated from fetal bovine serum (FBS).

Raman shift (cm^{-1})	Peak assignment
636.7	C-S stretching & C-C twisting of proteinstyrosine
680.4	Ring breathing modes in the DNA bases; G (ring breathing modes in the DNA bases)
716.5	C-N (membrane phospholipids head) $CN^{-}(CH_3)_3$ (lipids)
753.6	Symmetric breathing of tryptophan
783.3	U, T, C (ring breathing modes in the DNA/RNA bases)
808.1	Phosphodiester
853.8	Ring breathing mode of tyrosine & C-C stretch of proline ring
940.6	Skeletal modes (polysaccharides, amylose)
970.4	Lipids Phosphate monoester groups of phosphorylated proteins & cellular nucleic acids
1012.4	Phenylalanine

1044.0	Proline (collagen assignment) $\nu_3 PO_4^{3-}$(symmetric stretching vibration)
1111.0	Phenylalanine (proteins)
1140.8	Fatty acid
1183.7	Cytosine, guanine, adenine
1226.1	Amide III
1268.2	δ(=C-H) (phospholipids)
1287.5	Cytosine
1342.9	G (DNA/RNA) CH deformation (proteins and carbohydrates)
1359.8	Tryptophan
1385.1	CH_3 band
1399.7	C=O symmetric stretch, CH_2 deformation NH in-plane deformation
1438.3	CH2 and CH3 deformation vibrations, Cholesterol, fatty acid band
1510.4	A (ring breathing modes in the DNA bases)
1566.4	Tryptophan
1592.6	G (DNA/RNA), CH deformation (proteins, and carbohydrates)
1613.7	C=C stretching mode of tyrosine & tryptophan
1658.5	Fatty acids, Amide I (collagen assignment), Triglycerides (fatty acids)

Table 3.1. List of assignments of the Raman peaks obtained from Raman spectrum of FBS.

3.3.2 Correlative Study using Raman Mapping and Electron Microscopy

Due to the small size of the exosomes (<200 nm) and the limited spatial resolution of SERS, it is not feasible to see individual exosomes under optical microscope to confirm the source of the Raman spectra. To clearly identify the source of Raman signature, a correlative study was done using Raman mapping and SEM imaging. The original FBS derived exosome solution was diluted to three different concentrations (stock, x3 and x10 times respectively). The Raman mapping was taken on these different concentrations of exosomes. The distance of the Raman mapping between each point is set as 2 μm to avoid overlap of adjacent laser spots. At each concentration, we collected Raman spectra for 10 x 10 pixels. Figure 3.9, a-c shows the Raman mapping results, in which the black pixels represent the existence of the exosomes. Figure 3.9d illustrates how the existence of the Raman signature from the exosomes was decided. Three Raman modes with high S/N ratio was chosen as the indicators: 1012 cm^{-1}, 1509 cm^{-1}, and 1613 cm^{-1}, with each mode representing the vibrational mode of Phenylalanine, the ring breathing mode in the DNA bases, and the Raman mode of Tyrosine, respectively. The existence of these peaks was also indicated by the red, yellow and blue pixels respectively. The black pixels implied the presence of all three peaks, which was considered as the Raman signature from the exosomes. From the Raman mapping results, we found that the number of exosomes observed, decreases with the increasing dilution. To further confirm that the Raman spectrum is from exosomes, not other large extracellular vehicles, SEM measurements of the same samples with three different concentrations were taken. The exosomes and other extracellular vehicles could be directly observed and the density of the exosomes can be calculated and compared with the Raman mapping results.

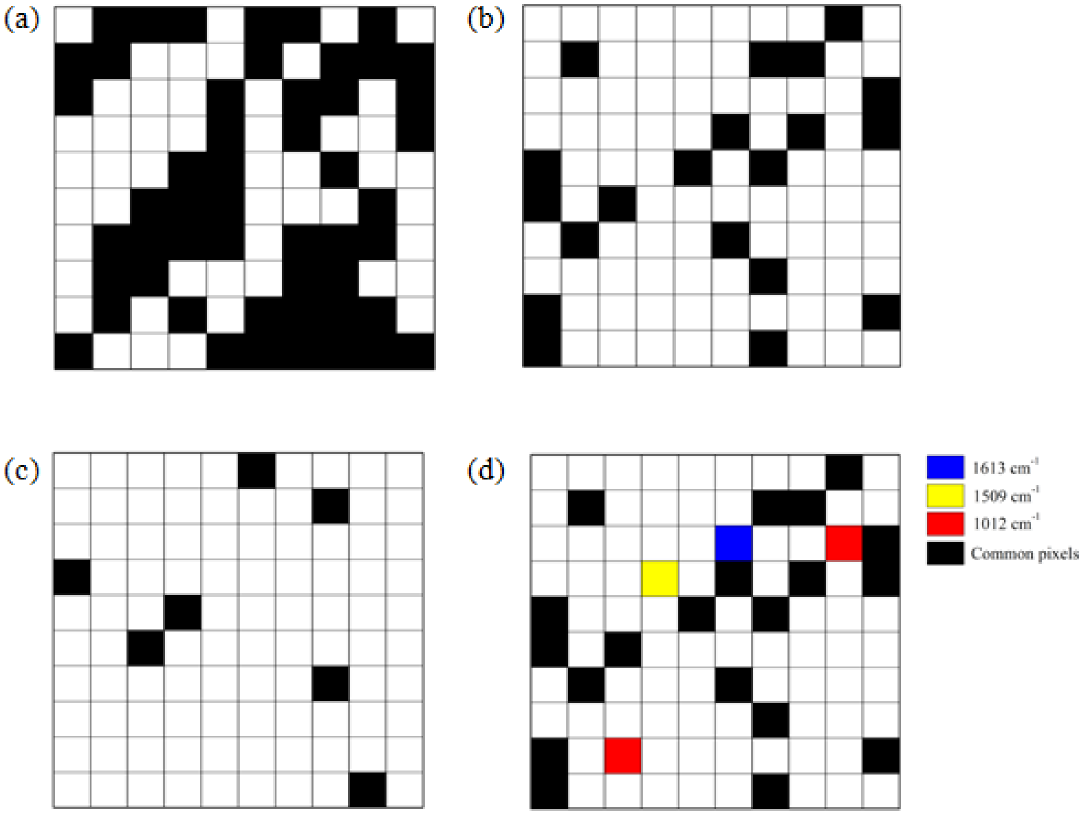

Figure 3.9. Raman mapping results on the exosomes at three different concentrations. (a) stock, (b) 3 times diluted and (c) 10 times diluted. (d) The method to determine the Raman signature of exosomes. The red, yellow and blue pixels stand for the existence of the 1012 cm^{-1}, 1509 cm^{-1}, and 1613 cm^{-1} individually. The black pixels are where all of the three peaks appear together.

The images acquired by SEM are presented in Figure 3.10a. The density of the exosome is calculated by counting the number of the exosomes within randomly selected area (9 μm x 9 μm, Fig. 3.10a). The final density was determined by taking the average of ten measurements. Figure 3.10b shows the shape and size of the exosomes but due to the low resolution of the SEM, the detailed structure was further visualized by TEM (Figure 3.10c). The bar graph represents exosome density, obtained from Raman mapping and from the SEM measurement (Figure 3.11).

Comparison of the exosome density obtained separately using Raman mapping and SEM measurement shows a good correlation between the two methods. The two measurements show similar exosome density within experimental error. The statistical significance test between the Raman mapping and SEM measurement showing that p-value is 0.385, indicating no significant difference. In the meantime between different groups the p-value is 0.017 indicating a significant difference.

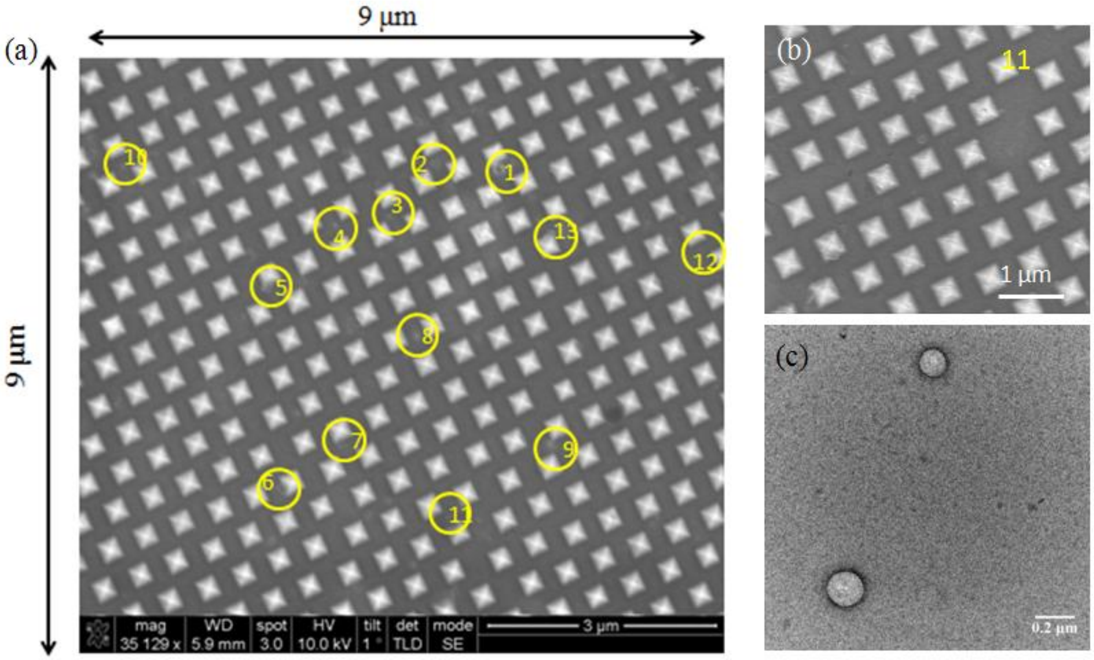

Figure 3.10. Electron microscopy on the exosomes. (a) The SEM image of exosomes on graphene substrate at magnification of ~35,000x. The area is 9 µm x 9 µm. The yellow circles markes the presence of exosomes within this region. (b) The SEM image at position 11 in (a) at magnification of ~50,000x. (c) TEM image of the exosomes at the magnification of 80,000x.

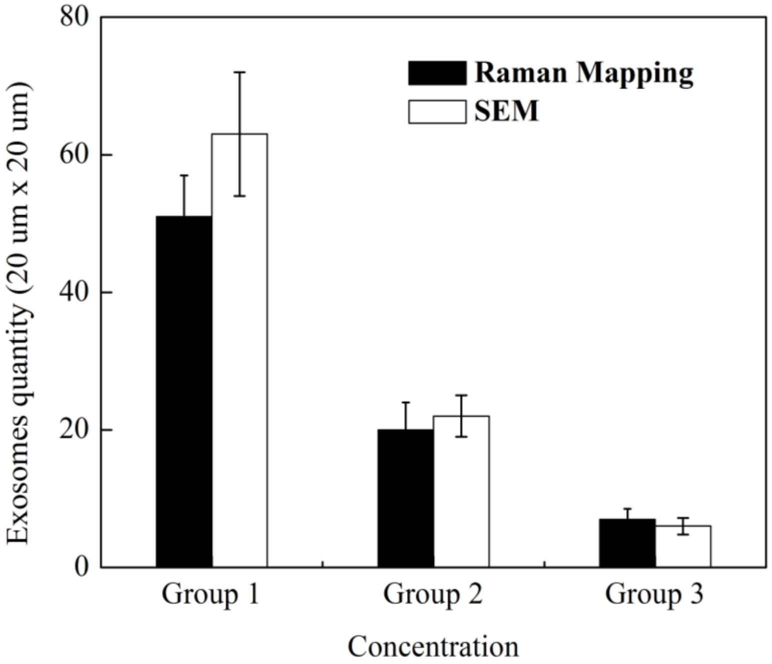

Figure 3.11. Comparison of the exosome density obtained through Raman mapping and SEM at three different concentrations (Group 1, stock; Group 2, 3x dilution; Group 3, 10x dilution). The black columns represent the exosome density acquired by Raman mapping and the white column represents the exosome density calculated from SEM images.

3.3.3 Raman Mapping Result of Individual Exosomes.

In the Raman mapping of Figure 3.9 the intensity of the Raman spectrum at each pixel changes. This variation may be due to the existence of larger EVs or the change of relative positions between exosomes and laser spot. Also the uncertainty exists that the Raman spectra come from the fragments of various biological entities (such as proteins) instead of exosomes. To eliminate such uncertainty and better illustrate individual exosomes at each pixel of the Raman map shown in Figure 3.9, a finer step Raman mapping using 0.1-μm step size was obtained at positions where Raman signature of exosomes was detected in the coarse-step mapping. The graphene G peak (Figure 3.12a) was used as a scale for normalizing the Raman signal intensity at different pixels so that the influence of hot-spot intensity fluctuation would be offset. Examination of the Raman spectrum of a single exosome (Figure 3.12a) showed multiple peaks, among which the graphene peak (G) was easily identified. The Raman mapping result was based on the peak intensity at 1509 cm-1 and 3D reconstruction of peak intensity changes along the x- and y-axes (Figure 3.12b). The lateral spread of ~2 μm of the Raman signal is attributed to the typical diameter of a focused Gaussian beam of the excitation laser convoluted over the ≤200 nm size of individual exosomes. This finer-step scanning demonstrated that at each Raman mapping pixel, as shown in Figure 3.9, the Raman spectrum was generated from individual exosomes. Through the Raman and SEM correlative study of exosome at different concentrations, we can conclude that the Raman spectrum shown in Figure 3.8 and the Raman mapping results presented in Figure 3.9, (a-d) is indeed from the individual exosomes, not from other larger vesicles or biomolecules.

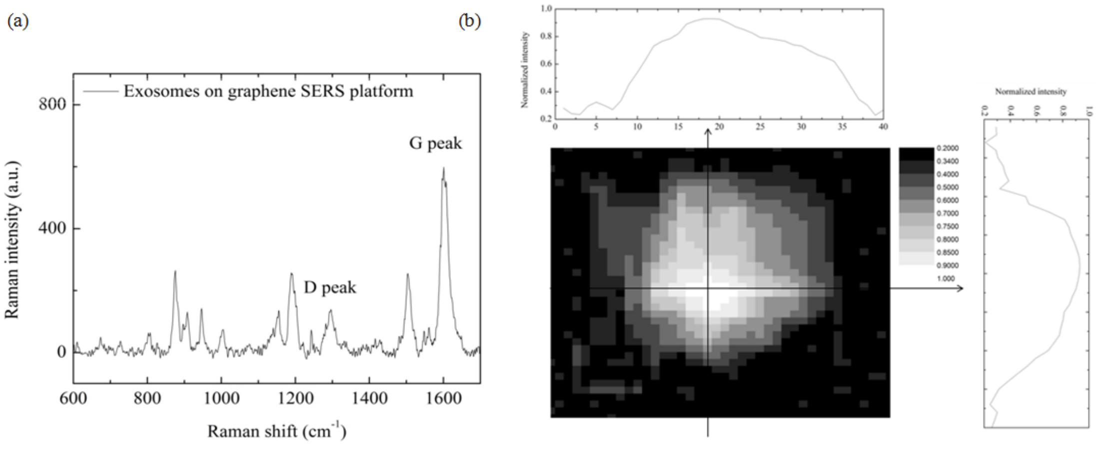

Figure 3.12. Raman mapping of intact individual exosome. (a) The Raman spectrum of a single exosome with graphene G peak. (b) Raman mapping result with a step size of 0.1 μm. The grey map is plot based on the peak intensity at 1509 cm^{-1}. Inset: The peak intensity changes along x-axis and y-axis across the exosomes.

3.3.4 Distinguishing Exosomes from Different Sources

SERS is very sensitive to the chemical composition of biological samples. Therefore, the technology potentially can distinguish exosomes from different sources reflecting the variation in cell type and cell homeostasis state. To test whether our platform could achieve this feat, we analyzed exosomes from three additional sources, including human serum from healthy individual, and two human lung cancer cell lines HCC827 and H1975. We collected about 10 ×10 Raman spectra for each type of exosomes. The averaged spectra of the exosomes from each source show both similarities and differences (Figure 3.13a-d). The peak assignments can be found in the Table 3.2-3.4. Peaks at 1113, 1208, 1340, 1420, and 1605 cm^{-1} are characteristic of nucleic acids, peaks at 1160 and 1310 cm^{-1} came from lipids, whereas protein peaks included those at 1260 cm^{-1} (amide III), 1490 cm^{-1} (amide II), and 1547 cm^{-1} (amide II). The common Raman peak at about 845 cm^{-1} represents (C-O-C) skeletal mode.

The main changes were observed in the relative intensity among samples. For example, the relative intensity of nucleic acid bands was substantially higher in the normal human and bovine exosomes than in the cancer cell-line exosomes, whereas the relative intensity of the lipids bands was stronger in the cancer cell-line exosomes. For the cancer cells, there has been research showing that they contain excessive lipids and cholesterol stored in lipid droplets (LDs), and high LDs and stored-cholesteryl ester content in tumors are now considered as hallmarks of cancer aggressiveness[42,43,44]. Therefore, it is reasonable that the cancer cell related exosomes contain more lipids than normal cells. For the content of nucleic acid, there is no observations showing the difference between normal cells and cancer cells. Further study is needed for the understanding of the nucleic acid fluctuation among exosomes derived from different sources. In addition, each type of exosomes also displayed its own Raman bands, supporting the possibility of distinguishing among the exosomes from the different sources.

To test whether in addition to the qualitative differences listed above the data also could be quantitatively, we applied principle component analysis (PCA) (Figure 3.12). PCA is a statistical procedure that uses an orthogonal transformation to convert a set of observations of possibly correlated variables into a set of values of linearly uncorrelated variables called principal components (or sometimes, principal modes of variation). In our study, the correlated variables are the vectors including Raman shift and the related Raman intensity of each Raman spectrum. This orthogonal transformation is defined in such a way that the first principal component has the largest possible variance (that is, accounts for as much of the variability in the data as possible), and each succeeding component in turn has the highest variance possible under the constraint that it is orthogonal to the preceding components. In this work, the results of the PCA is presented using two principal components, PC1 and PC2. The procedure is as follows. First, the background of the Raman spectrum is subtracted and the data is saved as txt format. Then, PCA analysis can be done using a program coded by one of the group members. The program runs on a python compiler. 16 vectors are chosen along the Raman shift axis (847, 854, 1043, 1163, 1181, 1202, 1213, 1255, 1269, 1309, 1374, 1384, 1421, 1429, 1482, 1506 cm^{-1}) for fully regenerating original spectra. The PCA analysis results are in text file and can be inputted into R studio for graphing purpose. The graphing program in R studio is also coded by one of the group members.

The result of this analysis show clearly that the four types of exosomes used were clustered into different groups with specificity of 84% on average demonstrating that the exosomes released by distinct sources could be distinguish easily. These observations suggest that the methodology developed here could be used for measuring disease biomarker in exosomes free of biological labels and without the need to know the identity of individual biomarkers. Thus, the Raman signatures of the exosomes is the biomarker.

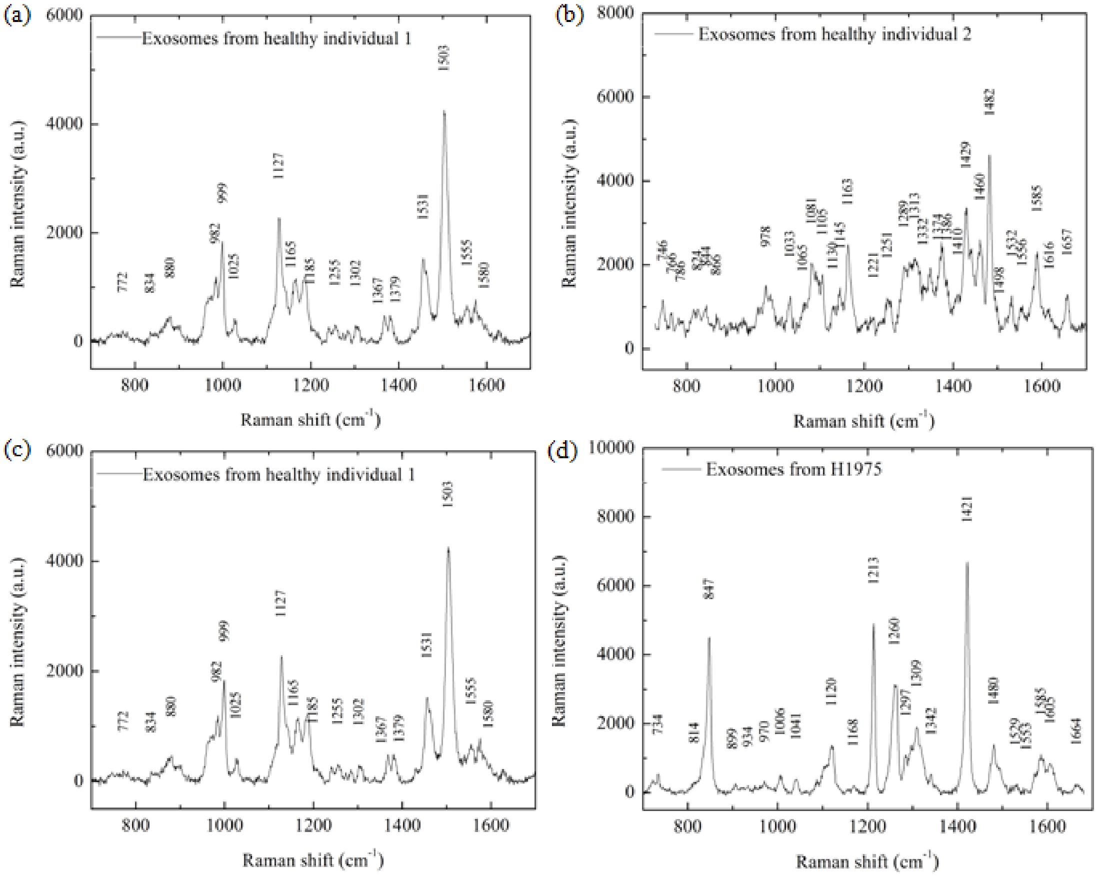

Figure 3.13. Grouping of exosomes from different sources. Raman spectra of exosome extracted from (a) serum of healthy individual, (b) FBS, and two human lung cancer cell lines- (c) HCC827 and (d) H1975.

Raman shift (cm^{-1})	Peak assignment
746.4	T (ring breathing mode of DNA/RNA bases)
786.8	DNA: O-P-O, cytosine, uracil, thymine, Pyrimidine ring breathing mode
815.2	Proline, hydroxyproline, tyrosine, v2 PO2- stretch of nucleic acids
824.6	O-P-O stretch DNA
844.6	Monosaccharides (a-glucose), (C-O-C) skeletal mode, disaccharide (maltose), (C-O-C) skeletal mode
866.8	Ribose vibration, one of the distinct RNA modes(with 915 and 974 cm-1)
978.6	C-C stretching b-sheet (proteins) =CH bending (lipids)
1033.1	Phenylalanine mode, v(CO), v(CC), v(CCO) (polysaccharides, pectin), C-H in-plane phenylalanine (proteins)
1041.0	Formalin peaks appearing in the fixed normal and tumor tissues
1065.7	Palmitic acid, Fatty acid

1081.3	v1CO3, v3PO4, v(C-C) skeletal of acyl backbone in lipid(gauche conformation)
1091.4	Phosphodioxy, Symmetric PO2- stretching vibration of the DNA backbone-phosphate backbone vibration as a marker mode for the DNA concentration C-N of proteins
1105.9	Carbohydrates peak for solutions, Phenylalanine (proteins)
1130.3	C-C skeletal stretch transconformation, Phospholipid structural changes (trans bersus gauche isomerism)
1145.7	Carbohydrates peak for solids
1163.3	Tyrosine (collagen type I) , tyrosine
1221.2	T,A (DNA/RNA), Amide III (proteins) =CH bending (lipids)
1251.6	C-O4 aromatic stretch
1289.2	Cytosine, Phosphodiester groups in nucleic acids
1295.6	CH2 deformation
1302.0	CH3, CH2 twisting (collagen assignment) CH2 deformation (lipid), adenine, cytosine
1313.8	CH3CH2 twisting mode of collagen/lipid
1332.9	-C stretch of Phenyl (1) and C3-C3 stretch and C5-O5 stretch CHa in-plane bend
1348.8	An unassigned mode
1374.2	T, A, G (ring breathing modes of the DNA/RNA bases)
1386.8	CH3 band
1410.9	Vs COO- (IgG)
1429.6	Deoxyribose, (B,Z-marker), CH2 scissoring
1439.0	C-H bending mode of accumulated lipids in the vecrotic core of the atheromatous plaque, fatty acids
1460.8	CH2/CH3 deformation of lipids & collagen, CH2 wagging, CH2/CH3 deformation, deoxyribose
1482.4	G, A (ring breathing modes in the DNA bases), Nucleotide acid purine bases (guanine and adenine)
1498.9	C=C stretching in benzenoid ring
1532.6	Carotenoid (absent in normal tissues)
1556.0	Tryptophan, n(CN) and d(NH) amide II (protein assignment), n(C=C) porphyrin, tyrosine, amide II, COO-
1569.2	Guanine, adenine, TRP (protein)
1589.4	Graphene D-peak, G (DNA/RNA), CH deformation (proteins, and carbohydrates)
1616.5	C=C stretching mode of tyrosine & tryptophan
1657.4	Fatty acids, Amide I (collagen assignment), Triglycerides (fatty acids)

Table 3.2. List of assignments of the Raman peaks obtained from Raman spectrum of exosomes isolated from serum of healthy individual.

Raman shift (cm^{-1})	Peak assignment
569.0	Phosphatidylinositol
588.7	Phosphatidylinositol
607.1	Cholestrol ester
632.7	C-S stretching & C-C twisting of proteins-tyrosine
675.2	Ring Breathing modes in DNA bases
705.3	Cholesterol, cholesterol ester
726.9	Phosphatidylserine
741.2	T (ring breathing mode of DNA/RNA bases)
769.8	Pyrimidine ring breathing mode
817.0	C-C stretching (collagen assignment)
854.4	Phosphatidylinositol
885.8	C-C stretching (collagen assignment)
892.8	Monosacchardies (β-glucose), (C-O-C) skeletal mode
927.4	C-C backbone (collagen assignment)
952.6	Symmetric stretching vibration of phosphate of HA
992.5	C-O ribose, C-C
999.3	Carotenoids (absent in normal tissues), Phenylalanine, δ(ring)
1034.3	carbohydrates peak for solution and solids, Proline (collagen assignment)
1069.1	Triglycerides (fatty acids)
1095.9	Phenylalanine (proteins)
1113.6	The strong C-O band of ribose (serves as marker band for RNA in solutions)
1138.0	Triglycerides (fatty acids)
1207.0	Tryptophan & phenylalanine v(C-C6H6) mode, Stretching of C-N
1238.4	Amide III
1253.5	Amide III (protein band), second amide, Amide III (unordered), structural protein modes of tumors, amide III vibration mode of structural protein, triglycerides (fatty acids)
1277.2	Differences in collagen content, Cytosine
1291.1	Palmitic Acid, Acyl chains, Fatty acids
1302.9	CH3/CH2 twisting or bending mode of lipid/collagen, CH3/CH2 twisting, wagging &/ or bending mode of collagens & lipids
1335.8	Graphene D-peak, G (DNA/RNA), CH deformation (proteins, and carbohydrates)
1369.6	CH3/CH2 twisting or bending mode of lipid/collagen
1383.3	CH3 band
1415.7	A,G (ring breathing modes of DNA/RNA bases)
1443.8	Guanine, TRP (protein), porphyrins, lipids,

	T, A, G (ring breathing modes of the DNA/RNA bases)
1474.8	Amide II (largely due to coupling of CN stretching & in-plane bending of N-H group,
1506.6	N=H bending, Cytosine
1523.0	Carotenoid (absent in normal tissues)
1547.4	Amide II
1584.8	Graphene G-peak,C=C olefinic stretch, Phenylalanine, hydroxyproline
1620.9	v(C=C), porphyrin
1658.8	Amide I (collagen) C=O stretching of collagen & elastin (pritein assignment)

Table 3.3. List of assignments of the Raman peaks obtained from Raman spectrum of exosomes isolated from lung cancer cell HCC827.

Raman shift (cm^{-1})	Peak assignment
640.0	C-S stretching & C-C twisting of proteins-tyrosine
682.4	Ring Breathing modes in DNA bases, G (ring breathing modes in the DNA bases)
734.1	Phosphatidylserine
814.6	Proline, hydroxyproline, tyrosine, PO2- stretch of nucleic acids
847.4	Monosaccharides (alpha glucose, (C-O-C) skeletal
899.7	Monosacchardies(beta-glucose), (C-O-C) skeletal mode, Disaccharide (maltose), (C-O-C) skeletal mode
934.3	C-C backbone (collagen assignment)
970.9	Phosphate monester group of phosphorylated porteins & cellular nucleic acids
1006.1	Carotenoids(absent in normal tissues), Phenylalanine, δ(ring)
1041.1	carbohydrates peak for solution and solids, Proline (collagen assignment)
1120.3	The strong C-O band of ribose (serves as a marker band for RNA in solutions)
1168.8	Lipids, v(C=C), δ(COH) (lipid assignment), v(C-C), carotenoid
1213.5	Tryptophan & phenylalanine v(C-C6H6) mode, Stretching of C-N
1260.0	Amide III (protein band), second amide, Amide III vibration mode of structural proteins, CH2 in-plane deformation (lipids), Triglycerides (fatty acids)
1297.5	Palmitic Acid, Acyl chains, Fatty acids
1309.3	CH3/CH2 twisting or bending mode of lipid/collagen
1342.2	Graphene D-peak, G (DNA/RNA), CH deformation (proteins, and carbohydrates)
1422.0	A,G (ring breathing modes of DNA/RNA bases)
1481.0	Amide II (largely due to coupling of CN stretching & in-plane bending of N-H group)
1529.1	Carotenoid (absent in normal tissues)

1553.5	Amide II
1590.9	Graphene G-peak,C=C olefinic stretch(protein assignment), Phenylalanine, hydroxyproline
1605.9	Cytosine (NH2), Ring C-C stretch of phenyl(1), Phenylalanine, tyrosine, C=C (protein)
1664.7	Amide I (collagen), C=C (of lipids in normal tissue; not that of amide I) Amide I (C=O stretching mode of proteins α-helix conformation)/ C=C lipids, C=O stretching of collagen & elastin (pritein assignment)

Table 3.4. List of assignments of the Raman peaks obtained from Raman spectrum of exosomes isolated from lung cancer cell H1975.

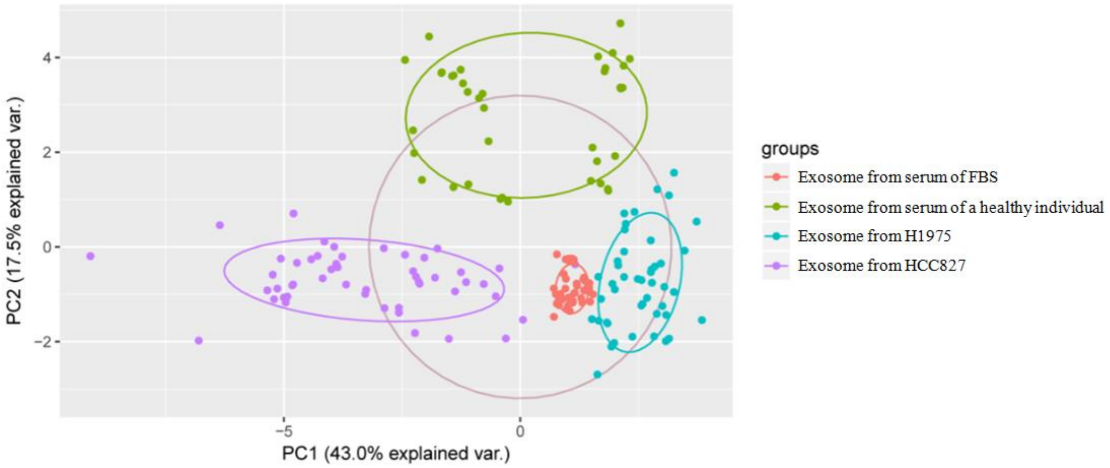

Figure 3.12. PCA of exosomes from different sources showing that they are clearly distinguishable

3.3.7 SERS analysis of exosomes isolated by different methods

The procedure of exosome isolation has yet to be standardized and is often insufficient in meeting the need of a particular downstream experiment. The combination of differential centrifugation, ultrafiltration and ultracentrifugation is considered to be the gold standard for isolation of pure exosomes. The disadvantages of this method include: 1) labor-intensive and time consuming protocols; 2) requirement for substantially larger samples volumes; and 3) costly instruments. Alternatively, EVs can be isolated using gentle salting out solutions, typically using commercially available kits, yet those produce a substantially wider size distribution of the resulting vesicles compared to the ultracentrifugation and ultrafiltration protocols. As part of our study, SERS hybrid platform is used to compare the efficacy of popular kit, ExoQuick from System Biosciences, and ultracentrifugation. The specific aim of this analysis is to test the possibility of using SERS analysis of exosomes when commercial kits are used to isolate exosome samples. The ExoQuick kit is widely used for exosomes isolation with a high-throughput and can achieve quantitative isolation of exosomes from low sample volumes (as little as 100 μL serum). The results of DLS (Figure 3.7) shows that the exosomes isolated using ultracentrifuge are more pure in terms of their size distribution (within diameter range of ~30-200 nm) than those from ExoQuick kit, although the western blot shows the successful isolation of exosomes using both the methods. To demonstrate the feasibility of the combined method of SERS and PCA to differentiate exosomes from scattered biomolecules and larger EVs, we collected the Raman spectra of the kit-isolated exosomes samples from human serum and compared the results with the exosomes isolated from the same samples using ultracentrifuge. The PCA results are presented in Figure 3.13. The overlap between the groups of exosomes isolated by ExoQuick kit and ultracentrifuge represents their common compositions. Needless to mention, the Raman spectra of kit-isolated exosomes are more scattered, indicating the presence of various other biomolecules such as proteins, lipids, etc. Also, there is a large overlap between the kit-isolated exosomes originated from FBS and human serum, probably from the common biomolecules shared by FBS and human serum. Therefore, according to our experience the ultracentrifuge method is more suitable, over kit-isolation, as exosome preparation method for SERS detection. Furthermore, SERS combining with PCA strengthens the potential for analysis of extracellular vesicles.

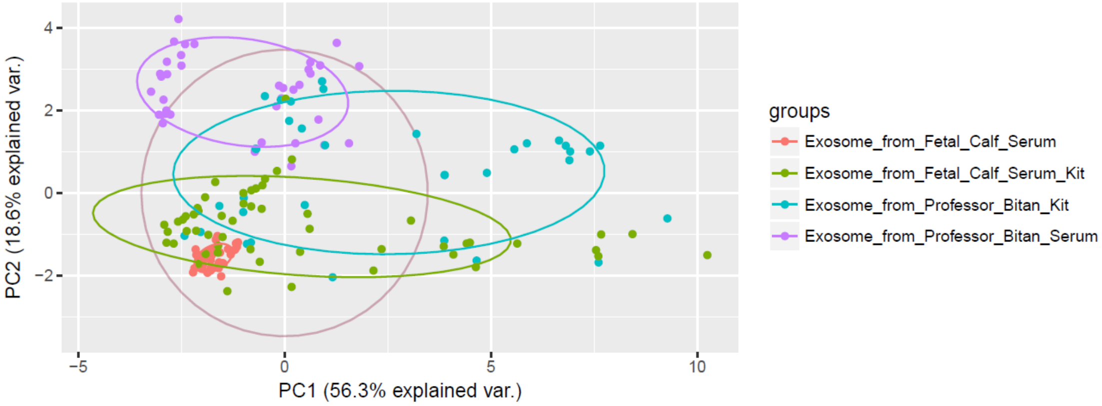

Figure 3.13. PCA of exosomes of different isolation methods.

3.3.5 Summary

We have demonstrated a methodology for unambiguous SERS identification of exosomes through the plasmonics powered hybrid platform. Comparing to all previously reported approaches, this method provides higher level of specificity as verified by the rigorous correlative study between more complementary techniques than any approach in the literature. In this study, the Raman spectrum of exosomes was first collected through a unique SERS hybrid platform. The specific proteins of the investigated samples and their size distribution were determined by western blot and dynamic light scattering (DLS). Then a correlative study using electron microscopy and Raman mapping was performed to statistically confirm the Raman signature being from the exosomes by comparing the density of the exosomes detected by electron microscopy and SERS mapping. Additionally, individual exosome was mapped out through the SERS spectroscopy. The rigorous correlative studies greatly enhanced the certainty of the SERS signature being precisely that of the exosomes. Furthermore, we verified the anticipated "finger print" capability to differentiate exosomes from four different sources through the hybrid platform.

3.4 SERS Study on T-cells

In this study, both stimulated and unstimulated T-cells were characterized using SERS hybrid platform. Three groups of samples were collected from the Prof. Yvonne Chen's lab. All of them are identical unstimulated T-cells. Then Sample 2 was stimulated right before the Raman measurement. The wavelength of the laser source for Raman spectroscopy was 785 nm. About 100 Raman spectra was collected for each group of sample. PCA are employed for the analysis of the experimental results.

Figure 3.14 shows typical spectra from sample 2 (stimulated T-cells) and sample 3 (unstimulated T-cells). In Figure 3.14 we marked the peaks which are included in the input vector matrix for PCA. The PCA result is shown in Figure 3.15. The graphene peaks has already excluded from PCA analysis. We could see that the Raman spectra are gathered into two regions. Sample 1 and 3 are almost overlapped. And they are well separated from sample 2. The PCA results indicate that the stimulated and unstimulated cell can probably be separated using the hybrid platform.

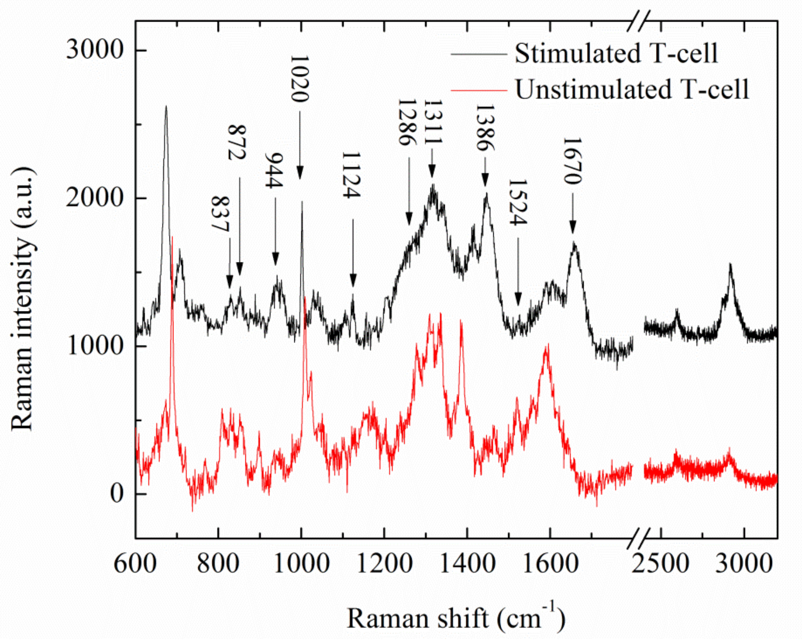

Figure 3.14. Raman spectra of stimulated T-cell (red curve, sample 2) and unstimulated T-cell (black curve, sample 3).

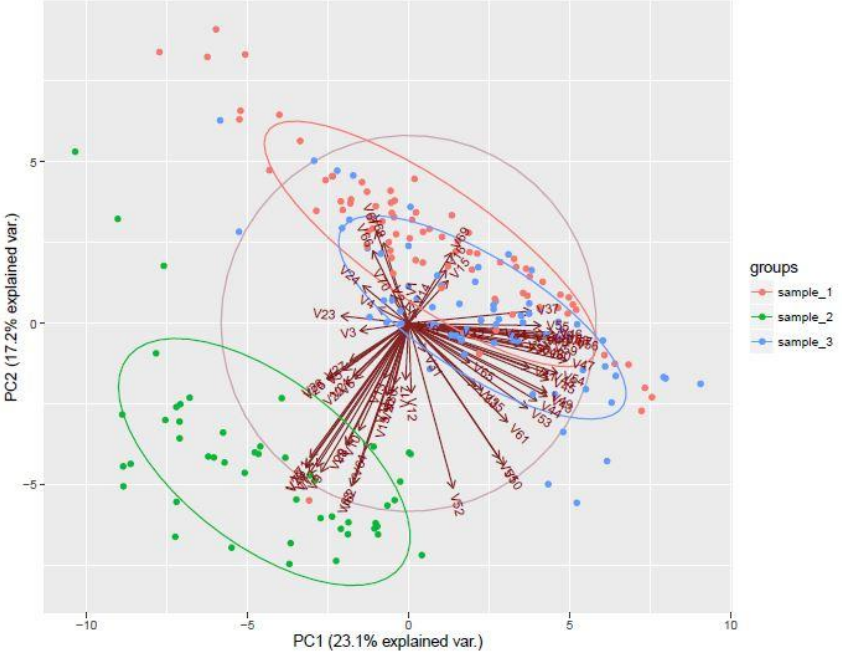

Figure 3.15. PCA analysis on T-cell Raman spectra. Sample 1 and 3 are the stimulated T-cells measured at different time. Sample 2 is the unstimulated T-cells.

3.5 Conclusion

The plasmon powered hybrid platform appears to be a powerful tool for the SERS detection. This approach provides stable and high specificity and sensitivity for exosomes detection, and therefore could offer a realistic possibility to identify disease specific biomarkers for early stage disease diagnosis, as the contents of exosomes are highly specific to the cells they are released from. Furthermore, the combination of SERS data with PCA maximizes the capability of this hybrid platform to study the functions of exosomes in various biological activities; and that would be an important step to deepen the understanding of the pathogenesis of a variety of diseases as well as exploring biomedical utilities of exosomes. In the study of CAR T-cells, the preliminary experimental results indicate that the Raman signature can be obtained from the hybrid platform and different types of T-cells can also be successfully distinguished. This provides the foundation for further CAR T-cells study.

References

1. Notingher, I. (2007). Raman spectroscopy cell-based biosensors. *Sensors*, 7(8), 1343-1358.

2. Lawson, E. E., Barry, B. W., Williams, A. C., & Edwards, H. G. M. (1997). Biomedical applications of Raman spectroscopy. *Journal of Raman Spectroscopy*, 28(2-3), 111-117.

3. Kneipp, K., Kneipp, H., Itzkan, I., Dasari, R. R., & Feld, M. S. (1999). Ultrasensitive chemical analysis by Raman spectroscopy. *Chemical reviews*, 99(10), 2957-2976.

4. Stiles, P. L., Dieringer, J. A., Shah, N. C., & Van Duyne, R. P. (2008). Surface-enhanced Raman spectroscopy. *Annu. Rev. Anal. Chem.*, 1, 601-626.

5. Garrell, R. L. (1989). Surface-enhanced Raman spectroscopy. *Analytical Chemistry*, 61(6), 401A-411A.

6. Sur, U. K. (2010). Surface-enhanced Raman spectroscopy. Resonance, 15(2), 154-164.

7. Moskovits, M. (2005). Surface-enhanced Raman spectroscopy: a brief retrospective. *Journal of Raman Spectroscopy*, 36(6-7), 485-496.

8. Le Ru, E.; Etchegoin, P. *Principles of Surface-Enhanced Raman Spectroscopy: and related plasmonic effects*. Elsevier: 2008.

9. Fang, J.; Yi, Y.; Ding, B.; Song, X. A route to increase the enhancement factor of surface enhanced Raman scattering (SERS) via a high density Ag flower-like pattern. *Applied Physics Letters* 2008, 92, 131115.

10. Xiong, Y.; McLellan, J. M.; Chen, J.; Yin, Y.; Li, Z.-Y.; Xia, Y. Kinetically controlled synthesis of triangular and hexagonal nanoplates of palladium and their SPR/SERS properties. *Journal of the American Chemical Society* 2005, 127, 17118-17127.

11. Xie, J.; Zhang, Q.; Lee, J. Y.; Wang, D. I. The synthesis of SERS-active gold nanoflower tags

for in vivo applications. *ACS nano* 2008, 2, 2473-2480.

12. Camden, J. P.; Dieringer, J. A.; Wang, Y.; Masiello, D. J.; Marks, L. D.; Schatz, G. C.; Van Duyne, R. P. Probing the Structure of Single-Molecule Surface-Enhanced Raman Scattering Hot Spots. *Journal of the American Chemical Society* 2008, 130, 12616-12617.

13. Dasary, S. S.; Singh, A. K.; Senapati, D.; Yu, H.; Ray, P. C. Gold nanoparticle based label-free SERS probe for ultrasensitive and selective detection of trinitrotoluene. *Journal of the American Chemical Society* 2009, 131, 13806-13812.

14. Wang, P., Zhang, W., Liang, O., Pantoja, M., Katzer, J., Schroeder, T., & Xie, Y. H. (2012). Giant optical response from graphene–plasmonic system. *ACS nano*, 6(7), 6244-6249.

15. Wang, P., Liang, O., Zhang, W., Schroeder, T., & Xie, Y. H. (2013). Ultra-Sensitive Graphene-Plasmonic Hybrid Platform for Label-Free Detection. *Advanced Materials*, 25(35), 4918-4924.

16. Xia, M., Zhang, P., Qiao, K., Bai, Y., & Xie, Y. H. (2015). Coupling SPP with LSPR for Enhanced Field Confinement: A Simulation Study. *The Journal of Physical Chemistry C*, 120(1), 527-533.

17. Théry, C., Ostrowski, M., & Segura, E. (2009). Membrane vesicles as conveyors of immune responses. Nature Reviews Immunology, 9(8), 581-593.

18. Pilzer, D., Gasser, O., Moskovich, O., Schifferli, J. A., & Fishelson, Z. (2005, November). Emission of membrane vesicles: roles in complement resistance, immunity and cancer.
In Springer seminars in immunopathology (Vol. 27, No. 3, pp. 375-387). Springer-Verlag.

19. van der Pol, E., Böing, A. N., Harrison, P., Sturk, A., & Nieuwland, R. (2012). Classification, functions, and clinical relevance of extracellular vesicles. Pharmacological reviews, 64(3),

676-705.

20. Johnstone, R. M. (2006). Exosomes biological significance: a concise review. Blood Cells, Molecules, and Diseases, 36(2), 315-321.

21. Taylor, D. D., & Gercel-Taylor, C. (2008). MicroRNA signatures of tumor-derived exosomes as diagnostic biomarkers of ovarian cancer. Gynecologic oncology, 110(1), 13-21.

22. Vlassov, A. V., Magdaleno, S., Setterquist, R., & Conrad, R. (2012). Exosomes: current knowledge of their composition, biological functions, and diagnostic and therapeutic potentials. *Biochimica et Biophysica Acta (BBA)-General Subjects*, 1820(7), 940-948.

23. Simpson, R. J., Lim, J. W., Moritz, R. L., & Mathivanan, S. (2009). Exosomes: proteomic insights and diagnostic potential. *Expert review of proteomics*, 6(3), 267-283.

24. Rabinowits, G., Gerçel-Taylor, C., Day, J. M., Taylor, D. D., & Kloecker, G. H. (2009). Exosomal microRNA: a diagnostic marker for lung cancer. *Clinical lung cancer*, 10(1), 42-46.

25. Michael, A., Bajracharya, S. D., Yuen, P. S., Zhou, H., Star, R. A., Illei, G. G., & Alevizos, I. (2010). Exosomes from human saliva as a source of microRNA biomarkers. *Oral diseases*, 16(1), 34-38.

26. Théry, C., Amigorena, S., Raposo, G., & Clayton, A. (2006). Isolation and characterization of exosomes from cell culture supernatants and biological fluids. *Current protocols in cell biology*, 3-22.

27. Théry, C., Regnault, A., Garin, J., Wolfers, J., Zitvogel, L., Ricciardi-Castagnoli, P., ... & Amigorena, S. (1999). Molecular characterization of dendritic cell-derived exosomes. *The Journal of cell biology*, 147(3), 599-610.

28. Lamparski, H. G., Metha-Damani, A., Yao, J. Y., Patel, S., Hsu, D. H., Ruegg, C., & Le Pecq,

J. B. (2002). Production and characterization of clinical grade exosomes derived from dendritic cells. *Journal of immunological methods*, 270(2), 211-226.

29. Conde-Vancells, J., Rodriguez-Suarez, E., Embade, N., Gil, D., Matthiesen, R., Valle, M., ... & Falcon-Perez, J. M. (2008). Characterization and comprehensive proteome profiling of exosomes secreted by hepatocytes. *Journal of proteome research*, 7(12), 5157-5166.

30. Smith, Z. J., Lee, C., Rojalin, T., Carney, R. P., Hazari, S., Knudson, A., ... & Laaksonen, T. (2015). Single exosome study reveals subpopulations distributed among cell lines with variability related to membrane content. *Journal of extracellular vesicles*, *4*(1), 28533.

31. Krafft, C., Wilhelm, K., Eremin, A., Nestel, S., von Bubnoff, N., Schultze-Seemann, W., ... & Nazarenko, I. (2016). A specific spectral signature of serum and plasma-derived extracellular vesicles for cancer screening. *Nanomedicine: Nanotechnology, Biology and Medicine*.

32. Kerr, L. T., Gubbins, L., Gorzel, K. W., Sharma, S., Kell, M., McCann, A., & Hennelly, B. M. (2014, May). Raman spectroscopy and SERS analysis of ovarian tumor derived exosomes (TEXs): a preliminary study. In *SPIE Photonics Europe* (pp. 91292Q-91292Q). International Society for Optics and Photonics.

33. Stremersch, S., Marro, M., Pinchasik, B. E., Baatsen, P., Hendrix, A., De Smedt, S. C., ... & Braeckmans, K. (2016). Identification of Individual Exosome-Like Vesicles by Surface Enhanced Raman Spectroscopy. *Small*, 12(24), 3292-3301.

34. Lee, C., Carney, R. P., Hazari, S., Smith, Z. J., Knudson, A., Robertson, C. S., ... & Wachsmann-Hogiu, S. (2015). 3D plasmonic nanobowl platform for the study of exosomes in solution. *Nanoscale*, 7(20), 9290-9297.

35 Kalos, Michael, and Carl H. June. "Adoptive T cell transfer for cancer immunotherapy in the

era of synthetic biology." Immunity 39.1 (2013): 49-60.

36 Porter, David L., et al. "Chimeric antigen receptor–modified T cells in chronic lymphoid leukemia." New England Journal of Medicine 365.8 (2011): 725-733.

37 Davila, Marco L., et al. "Efficacy and toxicity management of 19-28z CAR T cell therapy in B cell acute lymphoblastic leukemia." Science translational medicine 6.224 (2014): 224ra25-224ra25.

38 Hulteen, J. C.; Treichel, D. A.; Smith, M. T.; Duval, M. L.; Jensen, T. R.; Van Duyne, R. P. Nanosphere lithography: size-tunable silver nanoparticle and surface cluster arrays. The Journal of Physical Chemistry B 1999, 103, 3854-3863.

39 Oh, J. R.; Moon, J. H.; Yoon, S.; Park, C. R.; Do, Y. R. Fabrication of wafer-scale polystyrene photonic crystal multilayers via the layer-by-layer scooping transfer technique. Journal of Materials Chemistry 2011, 21, 14167-14172.

40. Dutta S, Reamtong O, Panvongsa W, Kitdumrongthum S, Janpipatkul, K., Sangvanich, P., Piyachaturawat, P., & Chairoungdua, A. (2015). Proteomics profiling of cholangiocarcinoma exosomes: A potential role of oncogenic protein transferring in cancer progression. Biochimica et Biophysica Acta, 1852, 1989-1999.

41. Movasaghi, Z., Rehman, S., & Rehman, I. U. (2007). Raman spectroscopy of biological tissues. Applied Spectroscopy Reviews, 42(5), 493-541.

42. Qiu, B., Ackerman, D., Sanchez, D. J., Li, B., Ochocki, J. D., Grazioli, A., ... & Simon, M. C. (2015). HIF2α-dependent lipid storage promotes endoplasmic reticulum homeostasis in clear-cell renal cell carcinoma. Cancer discovery, 5(6), 652-667.

43. Yue, S., Li, J., Lee, S. Y., Lee, H. J., Shao, T., Song, B., ... & Cheng, J. X. (2014). Cholesteryl

ester accumulation induced by PTEN loss and PI3K/AKT activation underlies human prostate cancer aggressiveness. Cell metabolism, 19(3), 393-406.

44. Bozza, P. T., & Viola, J. P. (2010). Lipid droplets in inflammation and cancer. Prostaglandins, Leukotrienes and Essential Fatty Acids (PLEFA), 82(4), 243-250.

Chapter 4 Plasmon Powered Hybrid Platform for Coupling SERS and CARS

4.1 Introduction

Bio-sensing is a topic that has attracted increasing amount of attention over the past decade or two. Biological detection with labels is a mature technique and has been broadly used for different types of bio-sensing from bio-molecules to cells. Label-free bio-sensing with the intrinsic advantage of examining biological systems in their unaltered states has its unique place in the broader field of bio-sensing. Raman spectroscopy is a label free bio-sensing technique based on the vibrational spectra of molecules and has been widely used for their detection[1,2,3]. The most noticeable drawback of Raman spectroscopy is the extremely low yield and the resulting low detection sensitivity. Various derivative techniques of Raman spectroscopy have been employed to enhance Raman signal. Among these derivatives, surface-enhanced Raman spectroscopy (SERS) and to a lesser extent coherent anti-Stokes Raman spectroscopy (CARS) are the most successful ones[4,5,6,7,8,9,10].

SERS is a technique capable of boosting by orders of magnitude the Raman signals from molecules located within tens of nanometers of metallic nanostructures[11]. The enhancement arises mainly from the intensified optical fields stemming from electromagnetic resonance (surface plasmon resonance) at the interface between metallic nanostructures and dielectric materials including vacuum. CARS is an alternative way of achieving Raman signal enhancement. It employs multiple photons to interact with molecular vibrations in a coherent fashion leading to greatly enhanced signals[12,13]. CARS has several unique features, such as being immune to the interference from fluorescence background, reduced photo damage to biological samples, and being very sensitive to the bio-molecule clusters (lipid compartments, protein clusters in cell and tissue cultures)[14,15]. Most importantly, CARS signals are superlinearly dependent on and thus very sensitive to the incident photon beam intensity.

Combining CARS with an appropriate resonant plasmonic nanostructure as commonly used in SERS, further multiplicative enhancement of Raman signals can be achieved[16,17,18,19,20]. If all three frequencies in CARS are in resonance with the collective modes of the surface plasmon, an exceedingly strong enhancement can be expected. This is known as surface-enhanced coherent anti-Stokes Raman scattering (SECARS). The feasibility of SECARS process from the molecules located near the nanostructured surface was predicted theoretically by Chew et al[21]. A few experimental attempts[22,23,24,25] using silver and gold nanostructures have been carried out. The first attempt was reported back in the 1990s. The technique was narrowband in nature which contained only one vibrational mode per acquisition. With the development of multiplex CARS[26] and the optimization of the plasmonic structure, broadband SECARS is established[16,18]. It contains more information about the chemical composition of samples, especially for biological samples (proteins, nucleic acid, exosomes, cells, *etc*.) whose spectrum typically spreads more than

1000 cm^{-1}. The plasmonic structure is also evolved from the randomly distributed nanoparticles to the well designed nanostructures. The effort resulted in further enhancement in SECARS leading to detection concentration limits approaching single molecule level. Despite of the tremendous progress made in this field, there exists one major shortcoming of all broadband SECARS techniques reported to date, namely poor spectral resolution especially when the concentration of detecting specie is low, while in the narrowband CARS/SECARS setup high spectral resolution could be achieved[27,28]. Low spectral resolution results in serious degradation in detection specificity, which is the main strength of Raman spectroscopy to begin with. The highest spectral resolution reported in the literature to date for the broadband SECARS setup is 100-200 cm^{-1}.

In our study, the hybrid platform is employed to combine surface plasmonics with broadband CARS into a SECARS system with superior spectral resolution and sensitivity comparing to other SECARS works reported in the literature. Comparing to previous SECARS setups, single molecule level sensitivity with high spectral resolution is achieved. The superior performance comes from the unique properties of the plasmonic hybrid platform and the modified CARS setup.

A chirped broadband CARS setup is employed, in which a significant spectral range of vibrational resonances is addressed simultaneously instead of a point-by-point acquisition of the CARS spectrum as in narrow-band CARS. This is particularly advantageous for the identification of the chemical constituents or the physical state of the sample. The Au pyramids plasmonic structure[29,30,31] is employed to provide high Raman enhancement factor (~10^{12}) using graphene as a hot spot marker, and has a broadband frequency (from 550 nm to 750 nm) response to the electromagnetic field. Therefore the photons at different frequencies are in resonance with surface plasmons concurrently and are enhanced in the same spatial location. The broadband SECARS spectrum with improved spectral resolution can provide more detail information on the chemical compositions of biological samples. We also demonstrate the utility of this SECARS system in the bio-sensing field using several types of biomolecules. Our unique SECARS system based on the plasmon powered hybrid platform provides a better solution for label free bio-sensing with higher specificity and sensitivity through improving both detection limit and spectral resolution.

4.2 Theoretical Analysis

CARS is a third-order nonlinear process[3] in which three input photons ω_1, ω_2, and ω_3 of generally two different frequencies ω_s (Stokes beam, ω_1) and ω_p (pump beam and probe beam, ω_2=ω_3) interact coherently through the third-order susceptibility of the material to produce an output photon ω_{AS} at anti-Stokes frequency with the intensity dependence of

$$I_{CARS} \propto \left|\chi^{(3)}\right|^2 I_P^2 I_S \quad (1)$$

where the I_{CARS} is the CARS signal intensity, I_P and I_S are the intensities of the input pump and Stokes beams respectively, and $\chi^{(3)}$ is the third-order susceptibility of the material. A properly designed metallic nanostructure substrate can provide large local field enhancement due to plasmon resonance[32,33], which is the mechanism responsible for SERS. Provided all input (ω_s, ω_p) and output (ω_{AS}) frequencies are in resonance with the plasmonic mode(s) of the nanostructure, the surface-enhanced CARS signal from analyte molecules located in the immediate vicinity of the nanostructure will be amplified. The total enhancement factor would theoretically scale as eighth power of local field enhancement factor (as compared to the fourth power for SERS alone):[14]

$$G_{SECARS} = g_p^4 g_s^2 g_{AS}^2 \quad (2)$$

where the G_{SECARS} is the overall enhancement factor, the g_p, g_s and g_{AS} are the enhancement factors of the pump/probe beam, Stokes beam and anti-Stokes beam respectively.

In addition to sensitivity, simultaneous high spectral resolution and wide spectral bandwidth are highly desired for bio-sensing applications. Several efforts[34,35,36] have been devoted to developing broadband CARS setups with high spectral resolution in the past few years. The basic principle is to employ a broadband Stokes pulse to simultaneously excite several vibrational modes in the sample along with a narrowband pump/probe pulse. In pioneering experiments[37,38] two separate lasers of femtosecond and picosecond pulse durations were used to excite the sample. This approach required a complex synchronization system. An alternative approach involves a single femtosecond laser source from which the Stokes pulse is produced via supercontinuum generation and the pump/probe pulse is obtained by spectral filtering of the initial pulse[39]. In present work we too use a single femtosecond pulse source, but generate Stokes supercontinuum in a short piece of a regular fiber, while the narrowband pump/probe pulse is generated via optical parametric amplification (OPA) and spectral filtering.

The principle of our approach and spatiotemporal spectrogram of the pulses interacting on the sample are shown in Figure 4.1. The broadband chirped Stokes and narrowband transform-limited pump/probe pulses are overlapped in space and time on the sample. Thus, a molecular vibration is driven with down-sweeping frequency $\omega_p - \omega_s$. The anti-Stokes signal is then generated at down-sweeping frequency $\omega_p + (\omega_p - \omega_s)$ and detected in a time-averaged manner with a typical broadband spectrometer. The total bandwidth of the detectable CARS signal is determined by the spectral width of the Stokes pulse, while the spectral resolution is determined by the bandwidth of the pump/probe pulse. To take advantage of the local field enhancement at all frequencies involved we employ a broadly resonant nanostructured gold substrate consisting of an array of sharp nanopyramids with a monolayer graphene draped on top as described below.

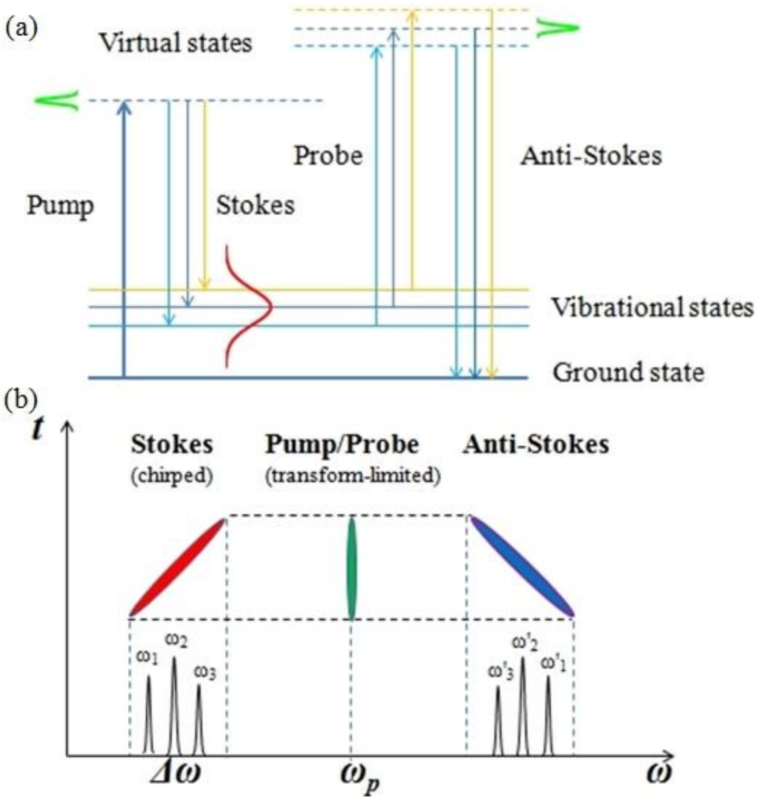

Figure 4.1(a) Energy (Jablonski) diagram of a typical broadband CARS process: broadband Stokes and narrowband pump pulses excite several vibrational modes simultaneously. A narrowband probe pulse subsequently scatters off the excited vibrations to produce broadband anti-Stokes signal. (b) Spectrogram of Stokes, pump/probe and anti-Stokes pulses for generating broadband CARS.

4.3 Experimental Setup

In this section, we present the experimental method of the SECARS system, which consists of two components, the broadband CARS setup and the SERS hybrid platform.

The broadband CARS setup is shown in Figure 4.2a (details see Supporting Information). Femtosecond pulses are generated and amplified by a Ti:Sapphire oscillator and a regenerative amplifier to 50 fs duration and 5 uJ energy at 250 kHz repetition rate.

The pulse train is then split into two branches to generate pump/probe and Stokes beams. The transmitted branch is coupled into a regular single-mode optical fiber of 5 cm length to generate super-continuum spanning 600-1000 nm via self-phase modulation (SPM) in a normal dispersion regime. Frequency chirping of the supercontinuum pulses take place in the optical fiber, rendering a pulse width of ~3 ps. The spectral portion between 650-775 nm is selected using a pair of long pass and short pass filters to be used as the Stokes beam. The advantage of using regular fiber and SPM is high pulse-to-pulse stability, low drift due to coupling, well-defined chirped pulse structure and smooth spectral magnitude of the supercontinuum as opposed to the more conventional supercontinuum generated in a photonic crystal fiber. However, a high pulse energy laser system is required to generate reasonably broad spectrum. The other branch is directed into an optical parametric amplifier (OPA) tuned to 633 nm (a convenient choice of wavelength of a HeNe laser) and passed through a 633 nm, 2 nm-wide bandpass filter to be used as the pump beam. To achieve high spectral resolution, the bandwidth of the probe pulses (633 nm) is additionally narrowed down by a 1200 lines/mm diffraction grating following by an iris of tunable width. The Stokes and pump/probe beams are spatially overlapped with a polarizing cube beamsplitter and temporally overlapped via a delay stage in the Stokes arm of the setup. To avoid substrate damage ,neutral density filter wheels are used to control the power on the sample. Beams are then coupled collinearly into a modified microscope through a dichroic mirror focusing on the sample and the SERS substrate through either a 10x or a 50x objective. The SECARS signal is extracted in reflection off the dichroic mirror and focused on a slit of an imaging spectrometer.

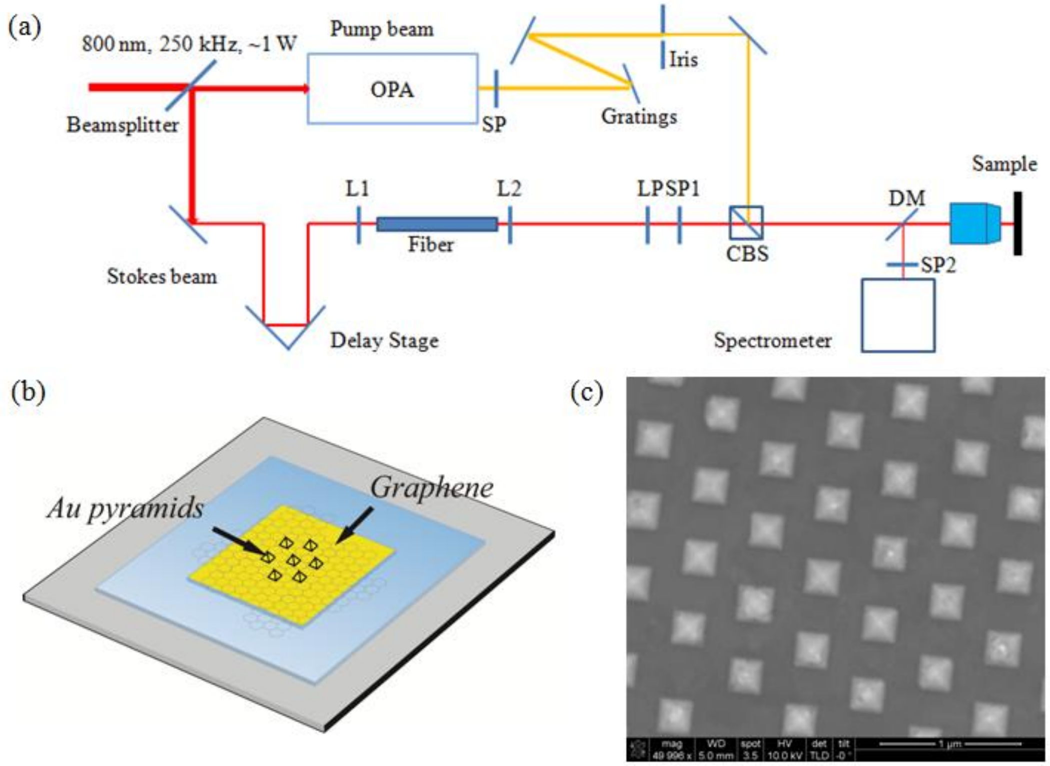

Figure 4.2. SECARS setup. (a) Schematic diagram of the broadband CARS setup. OPA: optical parametric amplifier; BP: 633 nm band-pass filter; CBS: cube beam splitter; LP: 633 nm long pass filter; SP1: 775 nm short pass filter; Grating: 1200 lines/mm grating; SP2: 633nm short pass filter; DM: 633 nm long pass dichroic mirror; L1: lens (EFL=25 mm); L2: lens (EFL=15 mm). (b) Schematic diagram of the SERS hybrid platform comprising single layer graphene and Au nanopyramids arranged in 2D hexagonal lattice (diagram is not to scale). (c) SEM image of the Au nanopyramids structure.

The plasmonic substrate for SERS enhancement consists a graphene-Au pyramids structure we hereby refer to as the hybrid platform[40,41] (Raman enhancement factor of up to 10^{12}). Figure 4.2b is the schematic diagram of the hybrid platform. Figure 4.2c is the scanning electron microscope (SEM) image of this substrate. Figure 4.3a shows the comparison of the SERS spectra of R6G on the hybrid platform, a commercial substrate (active at 633 nm) and on flat gold surface. The electromagnetic (EM) field enhancement of the hybrid platform is calculated by FDTD method (Figure 4.3b) and the inset shows the localized electric field distribution at 633 nm. The enhancement factor is defined as (E/E_0)^4 where E is the local maximum electric field, and E_0 is the amplitude of input source electric field. The EM field enhancement curve indicates a wide range of resonant frequency of the hybrid platform. The hybrid platform can support multiple surface plasmon resonant (SPR) modes is because of the pyramid structure. The width of pyramid as well as the separation between adjacent pyramids varies along z direction, which allows the incident light of different wavelength couple to the SPR modes. It provides the possibility to enhance all of the incident (pump beam ~633 nm, Stokes beam ~650-775 nm) and scattered photons (anti-Stokes beam ~500-610 nm) in the CARS process. The periodic Au nanopyramid structure with tunable size can be fabricated via a wafer-scale bottom-up templating approach[42]. In this study, the base dimension of the pyramids is ~250 nm and the center-to-center distance between adjacent pyramids is ~500 nm. Graphene provides a bio-compatible surface independent of the type of metal used for supporting SPR. Graphene also serves as a hotspot marker which indicates the intensity of individual hot spot of SPR.

As we mentioned at the beginning of this section, the SECARS system is achieved by combining the modified CARS setup with the unique hybrid platform. The spectral resolution and the coherent enhancement of SECARS is dominated by the CARS process. The localized field enhancement is determined by the spectral response and the enhancement factor of the SERS platform.

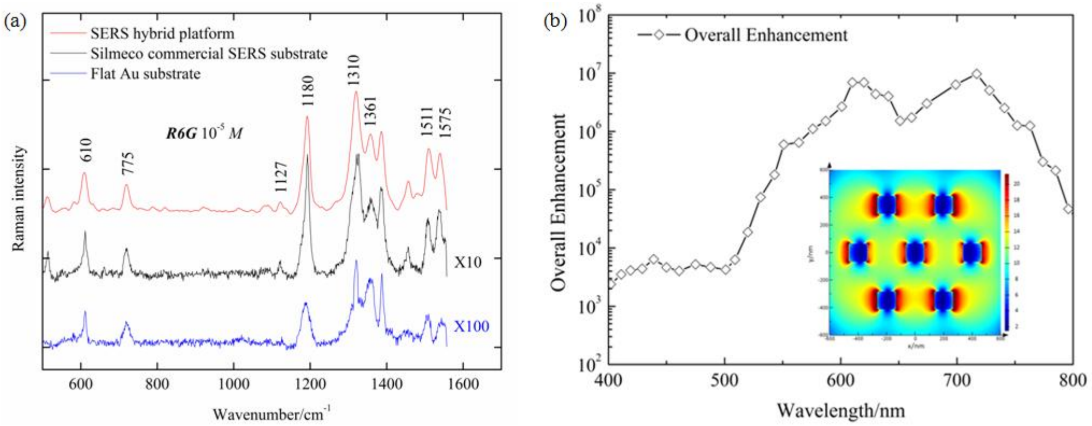

Figure 4.3. Performance of the SERS substrate. (a) The Raman spectra of R6G on three different substrate: SERS hybrid platform, Silmeco commercial substrate and flat gold film. The concentration of R6G is 10^{-5} *M*. Measured at 633 nm. (b) Simulation results of the overall enhancement of EM field using FDTD solution. The simulation result shows a broadband frequency response of the substrate to the incident EM field. Inset: simulation results of the EM field distribution at wavelength of 633 nm.

4.4 Results and Discussion

4.4.1 The Performance of Broadband CARS

Here we present the experimental results to show the properties of the CARS setups.

The input spectra of pump beam and Stokes beam are shown in Figure 4.4a. The Stokes beam is a supercontinuum spanning the spectral range between 650 nm and 775 nm. The bandwidth of the pump beam is about 0.5 nm (~10 cm^{-1}). The CARS spectrogram (Figure 4.4b) shows that the bandwidth of CARS spectrum is about 1500 cm^{-1} and can be continuously tuned from 300 cm^{-1} to 3000 cm^{-1} by adjusting the delay time between pump beam and Stokes beam. At the relative delay time of 1 ps, the spectrum range can cover from 900 cm^{-1} to 2400 cm^{-1}, which is the rich spectral region of most bio-molecules (proteins, DNA, etc). Beyond this range the CARS intensity decreases by several orders of magnitude. The intensity dependence on the pump beam and the Stokes beam are shown in Figure 4.4c plotted in log-log scale. The slope of the peak intensity versus P_{Stokes} is 1.11 and the slope of the peak intensity versus P_{pump} is 2.18 in agreement with the theory of CARS process, $I_{CARS} \propto \left|\chi^{(3)}\right|^2 I_P^2 I_S$. The performance of the broadband CARS is demonstrated using Rhodamine 6G (R6G). The CARS spectrum of Rhodamine 6G on silicon substrate is shown in Figure 4.4d. The concentration of R6G used for CARS testing is 10 m*M*. The acquisition time is 1 second. The measurement is taken after R6G solution is dried on the substrate. The CARS spectrum shows the Raman modes of 1275 and 1310 cm^{-1}, which are separated by 35 cm^{-1}, are clearly separated. The experimental results demonstrate its superlinearly dependence on the incident beams and its broadband feature with high spectral resolution.

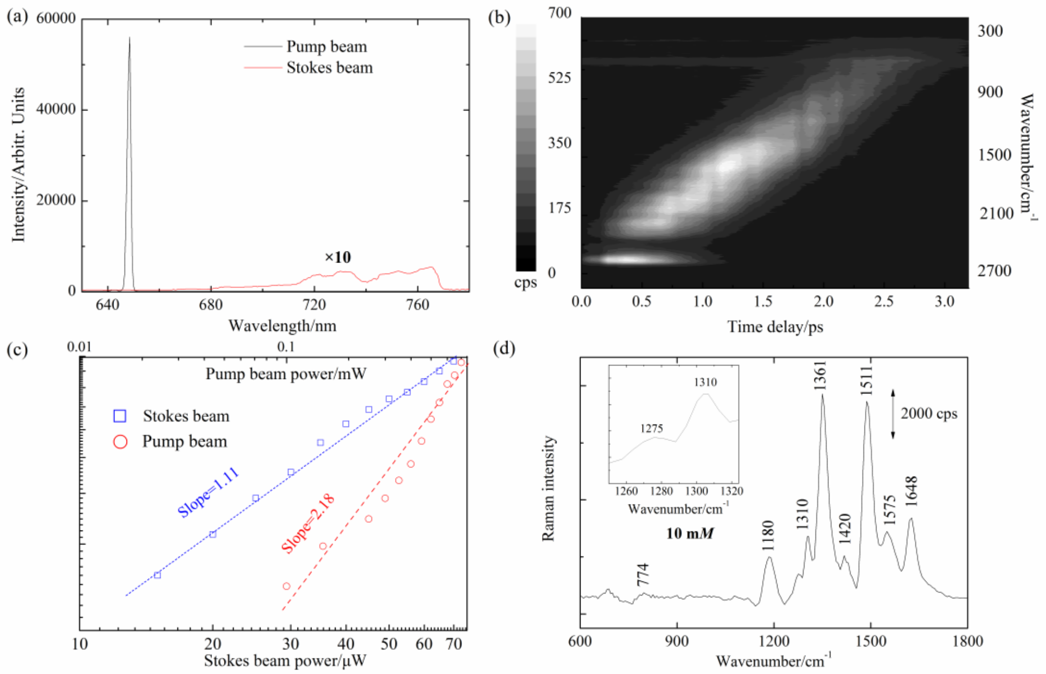

Figure 4.4. (a) Input spectra of the pump (green) and Stokes (red) beams. The Stokes beam is a supercontinuum, and the spectral range of which is from 650 nm to 775 nm. The bandwidth of the pump beam is about 0.5 nm (~10 cm^{-1}). (b) CARS spectrograms. The CARS spectrum range is shown as a function of the pump-Stokes time delay. the bandwidth of CARS spectrum is about 1500 cm^{-1} and can be continuously tuned from 300 cm^{-1} to 3000 cm^{-1} by adjusting the delay time. (cps: count per second). (c) Peak intensity versus P_{pump} change only and P_{Stokes} change only in logarithm coordinates. The slope of Stokes beam is 1.11 and pump is 2.18. (d) CARS spectrum of R6G on silicon substrate. The concentration of R6G solution is 10 m*M*. The inset shows that the Raman mode of 1275 and 1310 cm^{-1} which are separated by 35 cm^{-1} are clearly separated.

4.4.2 The Experimental Results Using Broadband SECARS

Based on the extraordinary properties of the plasmonic hybrid platform and the CARS setup, the SECARS measurement was performed by coupling these two processes. The SECARS spectrum of R6G on the hybrid platform is shown in Figure 4.5a. The concentration of the R6G solutions are 10^{-3} *M* (black curve), 10^{-5} *M* (blue curve), 10^{-7} *M* (red curve), and 10^{-9} *M* (gray curve) respectively. By combining CARS with the intense EM field from surface plasmon resonance, we could achieve the characteristic spectrum of R6G with signal-to-noise ratio better than 10:1 at 10^{-9} *M* analyte concentration. Comparing to that of conventional CARS of about 0.1 *mM*[43], the intensity of SECARS at low analyte concentration is much enhanced by combining with the surface plasmon field while keeping a high spectral resolution. It can be seen that the SECARS spectrum covers a broad spectrum range with a spectral resolution of <35 cm^{-1}, which is 4 times superior comparing to SECARS spectra spectral resolutions reported in other works[14-18, 20-24] (100-200 cm^{-1}). The inset shows the SECARS intensity dependent on the solution concentration in log-log scale. The dependence is in a super linear way at low concentration and then approaches saturation with concentration increasing. The saturation behavior can be understood by considering the model in which the majority of the Raman signal comes from individual hot spots of $(10 \text{ nm})^3$ volume. The separation of the hot spots is on the order of 1 μm which is close to the dimension of the size of focused laser beams. Therefore the Raman signal of individual pixels originates mainly from one hot spot on average. With increasing analyte concentration, the entire volume of individual hot spots is occupied by R6G molecules and the further increase in the analyte concentration results in the additional molecules being located outside the hotspots. As a result, the Raman signal approaches saturation. Figure 4.5b the magnified SECARS spectrum of R6G solution at 1 *nM*, which is at the single molecule level[14], i.e. the concentration level at which there is on average one molecule per plasmonic hotspot (see supporting information). At the concentration of 1 *nM*, 10 μl of such solution was dropped onto the substrate (~1 cm^2) such that on average an estimated number of 10 molecules fell into detection region (1 μm^2 area). Since the hotspots are highly localized region within area of 10 nm^2 scale (nano tip region), the molecules that fell into the hot spot region is further fewer, reaching single molecule level. To clearly demonstrate the enhancement of SECARS over SERS, we also directly compare the signal-to-noise ratio between SERS and SECARS due to the nonlinear effect and coherent effect. Figure 5c shows the SERS (hybrid platform, red line) and SECARS (black line) spectra of R6G at the same input power with the solution concentration on the level of 10^{-7} *M*. Comparing to SERS, the SECARS spectrum renders more than 2 orders of magnitude higher signal to noise ratio. For comparison, the SERS spectrum on commercial substrate is also shown in Figure 4.5c (blue curve). The signal-to-noise ratio is much higher than the SERS spectrum from hybrid platform.

We further demonstrate the utility of the SECARS using three different types of biomolecules. Dopamine is an organic chemical of the catecholamine and phenethylamine families that plays several important roles in the brain and body. Figure 4.5d shows the SECARS spectra of dopamine at different concentrations (10^{-5}, 10^{-7} and 10^{-9} *M*). The SECARS spectra of glutamine, an α-amino acid used in the biosynthesis of proteins, is shown in Figure 4.5e. Also Figure 4.5f shows the SECARS spectra of serotonin, a monoamine neurotransmitter. Again, the high spectral resolution can be observed in these spectra. These results indicate that this label free technique can be potentially used in various biological systems.

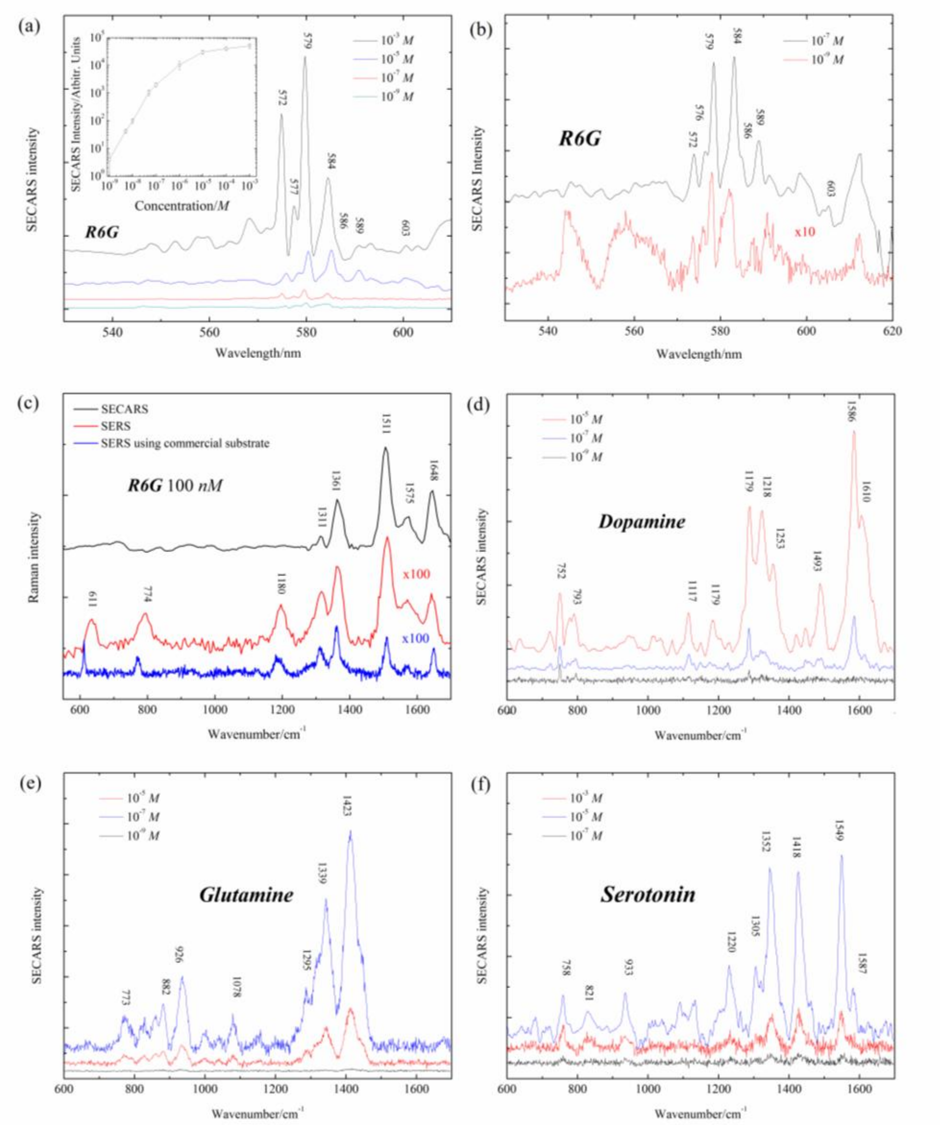

Figure 4.5. Experimental results of SECARS. (a) SECARS spectra of R6G on the Au pyramid substrate with the concentration of R6G solution at 10^{-3} *M* (black line), 10^{-5} *M* (blue line) and 10^{-7} *M* (red line) and 10^{-9} *M* (grey line). Inset: The SECARS peak intensity at 571 nm (1511 cm^{-1}) vs. solution concentration in log-log coordinates. (b) The enlarged SECARS spectra with the concentration of solution at 10^{-7} *M* (red line) and 10^{-9} *M* (grey line). (c) Comparison between SECARS (black curve) and SERS spectra (hybrid platform, red curve; commercial substrate, blue curve) of R6G (10^{-7} *M*) at

0.2 mW input power. (d) SECARS spectra of dopamine of three different concentrations (10^{-5} *M*, 10^{-7} *M* and 10^{-9} *M*). (e) SECARS spectra of glutamine of three different concentrations (10^{-5} *M*, 10^{-7} *M* and 10^{-9} *M*). (f) SECARS spectra of serotonin of three different concentrations (10^{-3} *M*, 10^{-5} *M* and 10^{-7} *M*).

The above presented experimental results show that the SECARS setup combines the advantages of SERS and CARS. Surface plasmon resonance is believed to contribute to the enhancement of all four coupled fields including input fields (pump, Stokes and probe beam) and output field that collectively form the overall SECARS enhancement. The multiplicative enhancement not only improves the detection sensitivity, but also higher temporal resolution. High temporal resolution benefits the study of the dynamics of biological processes such as lipid metabolism, antibody-antigen interactions *etc*.

4.4.3 Nonresonant Background and Laser Damage

The total CARS and SECARS signal contains an inherent non-resonant background. This non-resonant signal can be considered as the result of (several) far off-resonance transitions that also add coherently. In our SECARS measurement, the nonresonant background (NRB) also exists (Figure 4.6). In the spectra we present here, all of the NRB are subtracted.

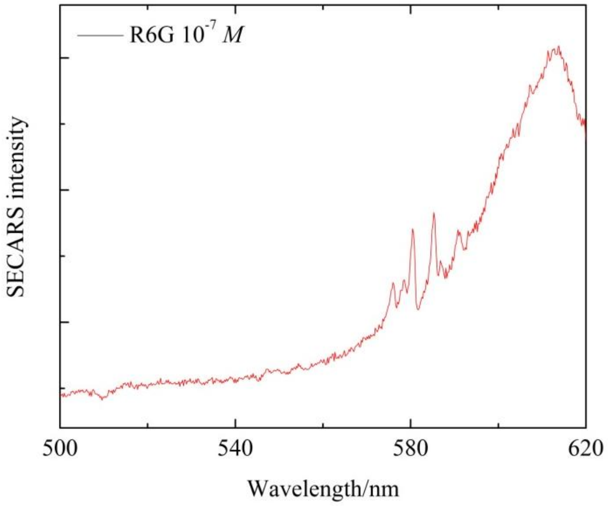

Figure 4.6. Raw data of SECARS spectrum of R6G at 10^{-7} *M*, in which the NRB can be observed clearly.

In SECARS, damage to the nanostructured substrate caused by the laser excitation is a potential concern. The damage threshold over a plasmonic surface under the illumination of laser pulses could be quite different compared to the situation of both SERS and CARS since the laser source for SECARS is ultrashort laser source. The peak power of ultrashort laser pulses is orders of magnitude larger than CW laser source. There are research results[44,45] showing that these metallic surfaces could be damaged at very low energy density per pulse (0.2 J/cm^2). Assuming the area of the focused laser spot being 1 μm^2, the threshold damage energy per pulse is about 2 nJ. Because of the higher absorption efficiency of the nanostructured surface as shown in Figure 4.3b, the damage threshold is expected to be even lower. During our SECARS measurement, the total input power is limited to below 0.2 mW (~0.8 nJ) to avoid damage to the hybrid platform. To confirm the threshold damage power, we compared the Raman spectra of graphene before and after the graphene is exposure to the femtosecond laser pulses (Figure 4.7). We could find that under 0.2 mW, the change of the graphene Raman intensity is negligible, indicating no obvious burnt or melt of the SERS substrate. Similar results could be found in Ref[46].

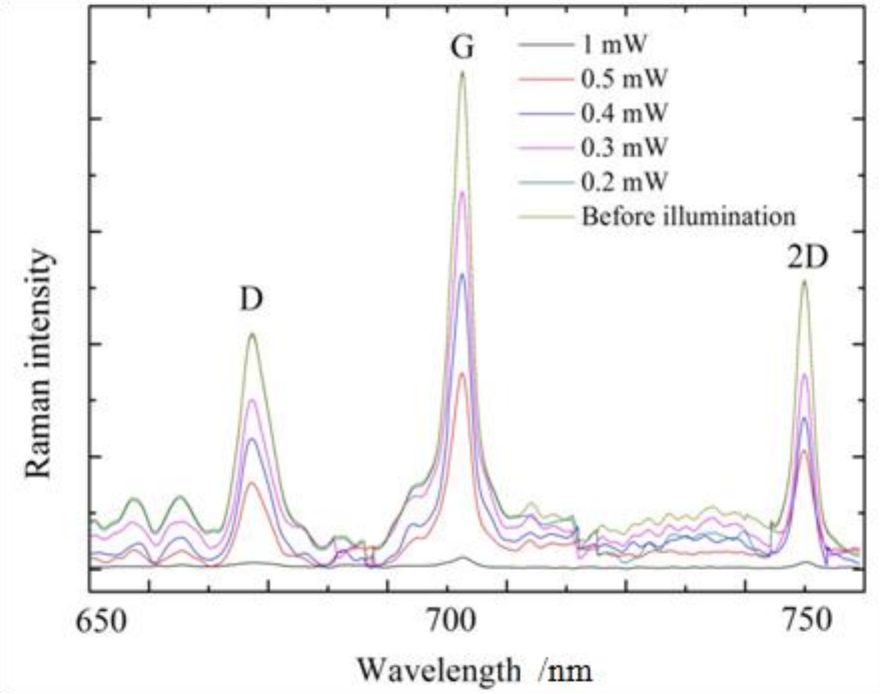

Figure 4.7. (a) The burnt spots on the SERS substrate by femtosecond laser pulses under optical microscope with different incident laser power. (b) Comparison of the Raman spectrum of graphene detected before and after femtosecond laser illuminated on the substrate.

4.5 Conclusion

In conclusion, a novel broadband SECARS setup based on the plasmon powered hybrid platform with high spectral resolution and high sensitivity is demonstrated. The unique platform gives a very intense local field and broadband resonance frequency, providing the possibility for an ultra high multiplicative enhancement over CARS and SERS. The chirped broadband Stokes beam and narrow band pump beam that generated from a single femtosecond laser source are combined to achieve wide spectral bandwidth with high spectral resolution. By optimizing the shapes of the incident pulses, this SECARS can be used to record an entire spectrum (~1500 cm^{-1}) during one acquisition, allowing for direct comparisons between Raman mode intensities within the broadband region of interest. The obtained SECARS spectrum has superior spectral resolution (<35 cm^{-1}), comparing to previous broadband SECARS setups (100-200 cm^{-1}). It allows for accurately distinguishing different vibrational modes such as 1275 and 1310 cm^{-1} modes of R6G. The signal-to-noise ratio of SECARS obtained was 2 orders of magnitude higher than that of SERS at 10^{-7} *M* analyte concentration. The detection limit is extended to 1 n*M*, in the single molecule regime. Even at such low concentration, the high spectral resolution is maintained. The utility of this system is further benchmarked using several different types of biomolecules. This work improves the performance of SECARS technique which can potentially reach single molecule sensitivity while keeping a high spectral resolution with the associated much enhanced specificity. This broadband high spectral resolution SECARS instrument is ideal for detection of biomolecules and dynamic monitor of biological processes. It opens the door for live and instantly biological detections with ultra high sensitivity and specificity. We believe that with such advantages, the new SECARS system has a bright future in the label free bio-sensing field.

References

1. Anker, J. N., Hall, W. P., Lyandres, O., Shah, N. C., Zhao, J., & Van Duyne, R. P. (2008). Biosensing with plasmonic nanosensors. Nature materials, 7(6), 442-453.

2. Pillai, I. C., Li, S., Romay, M., Lam, L., Lu, Y., Huang, J., ... & Lee, J. (2016). Cardiac Fibroblasts Adopt Osteogenic Fates and Can Be Targeted to Attenuate Pathological Heart Calcification. Cell stem cell.

3. Chou, I. H., Benford, M., Beier, H. T., Coté, G. L., Wang, M., Jing, N., ... & Good, T. A. (2008). Nanofluidic biosensing for β-amyloid detection using surface enhanced Raman spectroscopy. Nano letters, 8(6), 1729-1735.

4. Stiles, P. L., Dieringer, J. A., Shah, N. C., & Van Duyne, R. P. (2008). Surface-enhanced Raman spectroscopy. *Annu. Rev. Anal. Chem.*, *1*, 601-626.

5. Hildebrandt, P., & Stockburger, M. (1984). Surface-enhanced resonance Raman spectroscopy of Rhodamine 6G adsorbed on colloidal silver. *The Journal of Physical Chemistry, 88*(24), 5935-5944.

6. Begley, R. F., Harvey, A. B., & Byer, R. L. (1974). Coherent anti-Stokes Raman

spectroscopy. *Applied Physics Letters*, *25*(7), 387-390.

7. Xia, M., Qiao, K., Cheng, Z., & Xie, Y. H. (2016). Multiple layered metallic nanostructures for strong surface-enhanced Raman spectroscopy enhancement. *Applied Physics Express*, *9*(6), 065001.

8. Xia, M., Zhang, P., Leung, C., & Xie, Y. H. (2016). SERS optical fiber probe with plasmonic end-facet. *Journal of Raman Spectroscopy*.

9. Yan, Z., Xia, M., Zhang, P., & Xie, Y. H. (2017). Self-Aligned Trapping and Detecting Molecules Using a Plasmonic Tweezer with an Integrated Electrostatic Cell. *Advanced Optical Materials*.

10. Yan, Z., Xia, M., Wang, P., Zhang, P., Liang, O., & Xie, Y. H. (2016). Selective Manipulation of Molecules by Electrostatic Force and Detection of Single Molecules in Aqueous Solution. *The Journal of Physical Chemistry C*, 120(23), 12765-12772.

11. Haynes, C. L., McFarland, A. D., & Duyne, R. P. V. (2005). Surface-enhanced Raman spectroscopy. *Analytical Chemistry*, *77*(17), 338-A.

12. Zumbusch, A., Holtom, G. R., & Xie, X. S. (1999). Three-dimensional vibrational imaging by coherent anti-Stokes Raman scattering. *Physical review letters*, *82*(20), 4142.

13. Evans, C. L., & Xie, X. S. (2008). Coherent anti-Stokes Raman scattering microscopy: chemical imaging for biology and medicine. *Annu. Rev. Anal. Chem.*, *1*, 883-909.

14. Nan, X., Cheng, J. X., & Xie, X. S. (2003). Vibrational imaging of lipid droplets in live

fibroblast cells with coherent anti-Stokes Raman scattering microscopy. *Journal of lipid research*, *44*(11), 2202-2208.

15. Cheng, J. X., Book, L. D., & Xie, X. S. (2001). Polarization coherent anti-Stokes Raman scattering microscopy. *Optics letters*, *26*(17), 1341-1343.

16. Steuwe, C., Kaminski, C. F., Baumberg, J. J., & Mahajan, S. (2011). Surface enhanced coherent anti-Stokes Raman scattering on nanostructured gold surfaces. *Nano letters*, *11*(12), 5339-5343.

17. Koo, T. W., Chan, S., & Berlin, A. A. (2005). Single-molecule detection of biomolecules by surface-enhanced coherent anti-Stokes Raman scattering. *Optics letters*, *30*(9), 1024-1026.

18. Zhang, Y., Zhen, Y. R., Neumann, O., Day, J. K., Nordlander, P., & Halas, N. J. (2014). Coherent anti-Stokes Raman scattering with single-molecule sensitivity using a plasmonic Fano resonance. *Nature communications*, *5*.

19. Namboodiri, V., Namboodiri, M., Diaz, G. C., Oppermann, M., Flachenecker, G., & Materny, A. (2011). Surface-enhanced femtosecond CARS spectroscopy (SE-CARS) on pyridine. *Vibrational Spectroscopy*, *56*(1), 9-12.

20. Masia, F., Langbein, W., Watson, P., & Borri, P. (2009). Resonant four-wave mixing of gold nanoparticles for three-dimensional cell microscopy. Optics letters, 34(12), 1816-1818.

21. Chew, H., Wang, D. S., & Kerker, M. (1984). Surface enhancement of coherent anti-Stokes Raman scattering by colloidal spheres. JOSA B, 1(1), 56-66.

22. Liang, E. J., Weippert, A., Funk, J. M., Materny, A., & Kiefer, W. (1994). Experimental observation of surface-enhanced coherent anti-Stokes Raman scattering. Chemical physics letters, 227(1-2), 115-120.

23. Steuwe, C., Kaminski, C. F., Baumberg, J. J., & Mahajan, S. (2012, February). Molecular imaging with surface-enhanced CARS on nanostructures. In SPIE BiOS (pp. 82340E-82340E). International Society for Optics and Photonics.

24. Hua, X., Voronine, D. V., Ballmann, C. W., Sinyukov, A. M., Sokolov, A. V., & Scully, M. O. (2014). Nature of surface-enhanced coherent Raman scattering. *Physical Review A*, 89(4), 043841.

25. Fast, A., Kenison, J. P., Syme, C. D., & Potma, E. O. (2016). Surface-enhanced coherent anti-Stokes Raman imaging of lipids. *Applied optics*, 55(22), 5994-6000.

26. Knutsen, K. P., Johnson, J. C., Miller, A. E., Petersen, P. B., & Saykally, R. J. (2004, June). High-spectral-resolution multiplex CARS spectroscopy using chirped pulses. In *Biomedical Optics 2004* (pp. 230-239). International Society for Optics and Photonics.

27. Oron, D., Dudovich, N., Yelin, D., & Silberberg, Y. (2002). Narrow-band coherent anti-Stokes Raman signals from broad-band pulses. Physical Review Letters, 88(6), 063004.

28. Crampton, K. T., Zeytunyan, A., Fast, A. S., Ladani, F. T., Alfonso-Garcia, A., Banik, M., ... & Apkarian, V. A. (2016). Ultrafast coherent Raman scattering at plasmonic nanojunctions. The Journal of Physical Chemistry C, 120(37), 20943-20953.

29. Wang, P., Liang, O., Zhang, W., Schroeder, T., & Xie, Y. H. (2013). Ultra-Sensitive Graphene-Plasmonic Hybrid Platform for Label-Free Detection. *Advanced Materials*, *25*(35), 4918-4924.

30. Xia, M., Zhang, P., Qiao, K., Bai, Y., & Xie, Y. H. (2015). Coupling SPP with LSPR for Enhanced Field Confinement: A Simulation Study. *The Journal of Physical Chemistry C*, 120(1), 527-533.

31. Xia, M., Li, B., Yin, K., Capellini, G., Niu, G., Gong, Y., ... & Xie, Y. H. (2015). Spectroscopic Signatures of AA′ and AB Stacking of Chemical Vapor Deposited Bilayer MoS2. *ACS nano*, 9(12), 12246-12254.

32. Willets, K. A., & Van Duyne, R. P. (2007). Localized surface plasmon resonance spectroscopy and sensing. *Annu. Rev. Phys. Chem.*, 58, 267-297.

33. Pattnaik, P. (2005). Surface plasmon resonance. *Applied biochemistry and biotechnology,* 126(2), 79-92.

34. Müller, M., & Schins, J. M. (2002). Imaging the thermodynamic state of lipid membranes with multiplex CARS microscopy. *The Journal of Physical Chemistry B*, *106*(14), 3715-3723.

35. Okuno, M., Kano, H., Leproux, P., Couderc, V., & Hamaguchi, H. O. (2008). Ultrabroadband multiplex CARS microspectroscopy and imaging using a subnanosecond supercontinuum light source in the deep near infrared. *Optics letters*, *33*(9), 923-925.

36. Kano, H., & Hamaguchi, H. O. (2005). Ultrabroadband (> 2500cm− 1) multiplex coherent anti-Stokes Raman scattering microspectroscopy using a supercontinuum generated from a photonic crystal fiber. *Applied Physics Letters*, *86*(12), 121113.

37. Cheng, J. X., & Xie, X. S. (2004). Coherent anti-Stokes Raman scattering microscopy: instrumentation, theory, and applications. *The Journal of Physical Chemistry B,* 108(3), 827-840.

38. Cheng, J. X., Volkmer, A., Book, L. D., & Xie, X. S. (2001). An epi-detected coherent anti-Stokes Raman scattering (E-CARS) microscope with high spectral resolution and high sensitivity. *The Journal of Physical Chemistry B,* 105(7), 1277-1280.

39. Richter, Lee J., Teresa P. Petralli-Mallow, and John C. Stephenson. "Vibrationally resolved sum-frequency generation with broad-bandwidth infrared pulses." *Optics letters* 23.20 (1998): 1594-1596.

40. Wang, P., Zhang, W., Liang, O., Pantoja, M., Katzer, J., Schroeder, T., & Xie, Y. H. (2012). Giant optical response from graphene–plasmonic system. *ACS nano, 6*(7), 6244-6249.

41. Wang, P., Xia, M., Liang, O., Sun, K., Cipriano, A. F., Schroeder, T., ... & Xie, Y. H.

(2015). Label-free SERS selective detection of dopamine and serotonin using graphene-Au nanopyramid heterostructure. Analytical chemistry, 87(20), 10255-10261.

42. Sun, K., Zhang, W., Li, B., Lee, J. Y., Xie, Y. H., Schroeder, T., ... & Russell, T. P. (2012). Field emission tip array fabrication utilizing geometrical hindrance in the oxidation of Si. *IEEE Transactions on Nanotechnology*, 11(5), 999-1003.

43. Pezacki, J. P., Blake, J. A., Danielson, D. C., Kennedy, D. C., Lyn, R. K., & Singaravelu, R. (2011). Chemical contrast for imaging living systems: molecular vibrations drive CARS microscopy. *Nature chemical biology*, *7*(3), 137-145.

44. Wang, B., & Gallais, L. (2013). A theoretical investigation of the laser damage threshold of metal multi-dielectric mirrors for high power ultrashort applications. *Optics express*, *21*(12), 14698-14711.

45. Summers, A. M., Ramm, A. S., Paneru, G., Kling, M. F., Flanders, B. N., & Trallero-Herrero, C. A. (2014). Optical damage threshold of au nanowires in strong femtosecond laser fields. Optics express, 22(4), 4235-4246.

46. Kern, C., et al. "Comparison of femtosecond laser-induced damage on unstructured vs. nano-structured Au-targets." Applied Physics A 104.1 (2011): 15-21.

Chapter 5 Summary and Future Study

5.1 Summary

This dissertation discusses a new integrated system for biological detection and analysis based on a plasmonics powered hybrid platform, and explores its application in the label free bio-sensing field. The following is a summary of the dissertation work presented:

In Chapter 2, a self-aligned molecular manipulation method by combining the plasmonic tweezer and the electrostatic force is developed based on the hybrid platform. The combined method is demonstrated to be an effective method for increasing both the sensitivity and selectivity of bio-sensing techniques. The SPR field distribution and force density field distribution are calculated through FDTD solution indicating highly localized and very intense attraction force field around plasmonics hot spots. These hot spots give rise to the ability of precisely positional control of molecules and a high enhancement factor for SERS detection. A dramatic increase of the SERS signal intensity are observed under the combined method. The selective molecular manipulation based on molecular mass and charge state is also demonstrated. By combining plasmonic tweezer and electrostatic force, we successfully observed the capture of molecules by the nano-pyramid surface. Surprisingly even in sufficiently dilute solution (10^{-9} *M*), we can obtain the capture of single molecules by plasmonic tweezer after they are guided to individual hot spot by electrostatic force. The combined method offers a new approach for enhancing the sensitivity and selectivity of biosensing technique and a noninvasive way for precisely control and alignment of biomolecules in solution.

Chapter 3 presents the applications of hybrid platform for SERS detection. Two studies are presented on exosomes and CAR T-cells. In the study of exosomes, the approach provides stable and high specificity and sensitivity for exosomes detection, and therefore could offer a realistic possibility to identify disease specific biomarkers for early stage disease diagnosis, as the contents of exosomes are highly specific to the cells they are released from. Furthermore, the combination of SERS data with PCA maximizes the capability of this hybrid platform to study the functions of exosomes in various biological activities; and that would be an important step to deepen the understanding of the pathogenesis of a variety of diseases as well as exploring biomedical utilities of exosomes. In the study of CAR T-cells, the preliminary experimental results indicate that the Raman signature can be obtained from the hybrid platform and different types of T-cells can also be successfully distinguished. This provides the foundation for further CAR T-cells study.

In chapter 4, a novel broadband SECARS setup based on the plasmonics powered hybrid platform with high spectral resolution and high sensitivity is demonstrated. The unique platform gives a very intense local field and broadband resonance frequency, providing the possibility for an ultra high multiplicative enhancement over CARS and

SERS. The chirped broadband Stokes beam and narrow band pump beam that generated from a single femtosecond laser source are combined to achieve wide spectral bandwidth with high spectral resolution. This SECARS can be used to record an entire spectrum (~1500 cm^{-1}) during one acquisition, allowing for direct comparisons between Raman mode intensities within the broadband region of interest. The obtained SECARS spectrum has superior spectral resolution (<35 cm^{-1}), comparing to previous broadband SECARS setups (100-200 cm^{-1}). The signal-to-noise ratio of SECARS obtained was 2 orders of magnitude higher than that of SERS at 10^{-7} *M* analyte concentration. The detection limit is extended to 1 n*M*, in the single molecule regime. Even at such low concentration, the high spectral resolution is maintained. The utility of this system is further benchmarked using several different types of biomolecules. This work improves the performance of SECARS technique which can potentially reach single molecule sensitivity while keeping a high spectral resolution with the associated much enhanced specificity. This broadband high spectral resolution SECARS instrument is a powerful tool for detection of biomolecules and dynamic monitor of biological processes. It opens the door for live and instantly label free biological detections with ultra high sensitivity and specificity.

5.2 Direction of future study

Several bio-sensing related techniques have been successfully developed based on the plasmonics powered hybrid platform. Preliminary applications in the bio-sensing and biomedical field have been demonstrated, but more contributions in understanding of various biological activities can be achieved through these techniques. In this section, some of the future research direction will be discussed.

5.2.1 Understanding of the Functions of Exosomes in Neuro-disease

Recently, the exosomes have been extensively studied due to discoveries that exosomes (a) transport functional mRNA, miRNA, and DNA[1,2,3]; (b) are expressly packaged by cells for highly specific endogenous and exogenous intercellular communication[4]; (c) are heavily implicated in numerous pathologies, particularly neuro-disease (such as Parkinson disease and Alzheimer disease)[5]. Exosome secretion is also understood to be fundamental in intercellular communication, and exosomes can be isolated from most biological fluids (blood, urine, lymph, etc.) for potential use as biomarkers, since their protein, lipid, genetic, and metabolic content can be altered in diseased cells. However, to date the exact biological function of exosomes and mechanisms of action are yet to be fully elucidated.

Preliminary results have demonstrated that SERS can be employed as label free method for detecting the exosomes. The Raman signature can be obtained through the hybrid platform with high specificity. This provides the possibility to understand the functions of exosomes in the pathogenesis of neuro-disease and identify the specific biomarkers for early stage diagnosis, as the contents of exosomes are highly specific to the cells they are released from. In Parkinson's disease, there is evidence indicating that certain types of proteins in the patient cells play an important role in the progression of the disease. However, these types of proteins are still lack of specific fluorescence markers and thus label free method would be option for understanding if the exosomes are involved in the disease progression. In the future study, the Raman signature of exosomes extracted from healthy individual and patients can be compared using the hybrid platform and analyzed by PCA. The differences could be employed for early stage diagnosis. The disease related proteins can be isolated and also characterized using SERS. The Raman signatures can be used as an indicator to test whether these proteins have a higher amount in the exosomes extracted from patients. To some extent, this research would help understand the mechanisms of the pathogenesis of Parkinson's disease.

5.2.2 Dynamic Monitoring of Biological Activities in CAR T-cells

Optimization of CAR-T cell production remains a trial-and-error exercise due to a lack of phenotypic benchmarks that are clearly predictive of anti-tumor functionality. The efforts to improve cell preparation protocols remain empirically driven, with few guiding cues on which parameters to modify. From recent research[6,7], it could be found that activated T cells show a clear pattern of population bifurcation into two different groups ($\mathrm{CAR}^{hi}/\mathrm{CD25}^{+}$ *vs*. $\mathrm{CAR}^{lo}/\ \mathrm{CD}^{25}$). The "good" T cells ($\mathrm{CAR}^{hi}$ cells) consistently upregulate expression of the activation marker CD25. Target-cell lysis, cytokine production, and T-cell proliferation assays demonstrate that $CAR^{hi}/CD25^{+}$ cells are functionally superior to the "bad" T cells (CAR^{lo}/CD^{25-}). For the antigens that are exactly known, the flow cytometry based on the specific fluorescence antibody markers can be used to characterize the target cells. But the antigens are not always known. The SERS and SECARS based on the plasmonic hybrid platform are capable of generating the signature the target cells based on their unique vibrational modes. So they are possible to employed to distinguish the "good" or "bad" cells based their own signatures. This would serve as a way to provide feedback in quality control and T-cell manufacturing process development.

The SECARS could also be employed to understand the triggering mechanism of T cell receptor (TCR)[8,9]. There is considerable controversy about the mechanism of T cell receptor (TCR) triggering with no definitive proof in support for one hypothesis to the exclusion of the others. The key issue in TCR triggering is explaining how TCR binding to a peptide-MHC complex results in biochemical changes in the cytoplasmic domains of the TCR-CD3 complex. Since the SECARS has high sensitivity and thus high temporal resolution, it is capable to dynamically monitor the biological activities in CAR T-cells. By monitoring (1) the distribution change of TCR on the cell surface, (2) the conformation change of the compositions of the cell membranes and (3) segregation and redistribution of lipid rafts after binding, it is possible to support or exclude certain triggering hypothesis. This would deepen the understanding on the working mechanisms of the T-cells.

References

1 Valadi, H., et al. "Exosomes contain a selective number of mRNA and microRNA." Allergy: European Journal of Allergy and Clinical Immunology 62 (2007): 372.

2 Lässer, Cecilia, et al. "Human saliva, plasma and breast milk exosomes contain RNA: uptake by macrophages." Journal of translational medicine 9.1 (2011): 9.

3 Lázaro-Ibáñez, Elisa, et al. "Different gDNA content in the subpopulations of prostate cancer extracellular vesicles: apoptotic bodies, microvesicles, and exosomes." The Prostate 74.14 (2014): 1379-1390.

4 Kastelowitz, Noah, and Hang Yin. "Exosomes and microvesicles: identification and targeting by particle size and lipid chemical probes." Chembiochem 15.7 (2014): 923-928.

5 Beach, Allison, et al. "Exosomes: an overview of biogenesis, composition and role in ovarian cancer." Journal of ovarian research 7.1 (2014): 14.

6 Chen, Yvonne Y., Michael C. Jensen, and Christina D. Smolke. "Genetic control of mammalian T-cell proliferation with synthetic RNA regulatory systems." Proceedings of the National Academy of Sciences 107.19 (2010): 8531-8536.

7 Zah, Eugenia, et al. "T cells expressing CD19/CD20 bi-specific chimeric antigen receptors prevent antigen escape by malignant B cells." Cancer immunology research (2016): canimm-0231.

8 Van Der Merwe, P. Anton, and Omer Dushek. "Mechanisms for T cell receptor triggering." Nature reviews. Immunology 11.1 (2010): 47.

9 Li, Ya-Chen, et al. "Cutting Edge: mechanical forces acting on T cells immobilized via the TCR complex can trigger TCR signaling." The Journal of Immunology 184.11 (2010): 5959-5963.